2012

Development of a Near-Field Magnetic Projectile Location System

Andrew D. Lowery
West Virginia University

Development of a Near-Field Magnetic Projectile Location System

by

Andrew D. Lowery

Dissertation submitted to the
College of Engineering and Mineral Resources
At West Virginia University
in partial fulfillment of the requirements
for the degree of

Doctor of Philosophy
in
Mechanical Engineering

Submitted to

MaryAnn Clarke, Ph.D.
Powsiri Klinkhachorn, Ph.D.
Roy Nutter, Ph.D.
Franz Pertl, Ph.D.
James Smith, Ph.D., Committee Chairman

Department of Mechanical and Aerospace Engineering
College of Engineering and Mineral Resources
West Virginia University
Morgantown, West Virginia
2012

Keywords: Near-field, permanent magnet, magnetic location system

Abstract

Development of a Near-Field Magnetic Projectile Location System

by Andrew D. Lowery

Near-field magnetic principles and properties have been well studied and are used in a plethora of modern applications, ranging from medical applications to audio and video processing, and magnetic tracking. Current tracking applications are based in either AC or Pulsed-DC systems. Generally, AC systems have high resolution and accuracy, but perform very poorly in the presence of conducting magnetic materials. Pulsed-DC tracking has the benefit of not inducing large eddy currents in proximity to magnetic materials, thus increasing its overall accuracy. It has been suggested that pure DC systems are not feasible because they are unable to account for the presence of the Earth's magnetic field.

It was the purpose of this research to propose and create a system, and develop an algorithm, that has the ability to determine the three-dimensional position and orientation of a permanent magnetic source; the position and orientation to be determined by information reported by a network of single-axis magnetic sensors. Methodology to account for the Earth's magnetic field before, during, and after operation in order to remove ambient and environmental magnetic noise, much like a pulsed-DC system does, was also to be considered

A center-finding algorithm was developed to determine position (x- and y-axis) based on the unique geometry of the B-field of the magnetic source at any point in three-dimensional space. Two degrees of orientation, elevation and rotation, were calculated from the position and the reported values of the magnetic sensors. The z-axis position was then determined given the analytical model and the other calculated values. In addition to the computed position, a six input Kalman tracker-estimator was developed and implemented using three dimensions of position and velocities to aid in predicting the path the magnetic source will take, based solely on kinematics, to reduce position-based sensor error.

The contribution of this research shows that is it not necessary to obtain three-axis magnetic data to track a magnetic source in three-dimensional space. When the distribution of the magnetic flux density is known, it is possible to determine three-dimensional position and orientation with only single-axis information.

Experimental testing verified the theoretical predictions of this statement. A rotational test apparatus was used to verify two-dimensional position and orientation, while a linear test apparatus verified position in three dimensions. The same magnetic source was used, while changing the orientation for each test. Initial findings allow the magnetic source to be tracked on the rotational testing apparatus to within a radial error of 3.9% (mean) and less than 6.4% (worst case) for predictions. The linear apparatus is able to track the z-axis component of the source which can be determined within 0.19% (mean) and 0.24% (worst case), and mean three-dimensional position of the magnetic source within 1.4% error. These results suggest that the novel method presented in this document is credible method for magnetic detection and tracking.

To my family...

Acknowledgements

The author would like to extend his appreciation to the dissertation committee for their time and input into this project. The author would like to especially thank Dr. James Smith for his guidance, support, confidence, and advice throughout this process, as well as Drs. Franz Pertl and Roy Nutter for their feedback and critique. Additionally, a special thanks needs to be extended to the faculty, staff, and students, of the Center for Industrial Research Applications for their support and friendship, as well as the staff in the Department of Mechanical and Aerospace Engineering and the College of Engineering and Mineral Resources for administrative and logistical help.

And special thanks goes to my friends and especially my family for their unwavering support and motivation, to which none of this would have been possible. Thank you.

Table of Contents

Abstract ii
Acknowledgements v
List of Figures ix
List of Tables xiv
Nomenclature xv

Chapter 1 – Introduction 1
1.1 Research Objective 2
1.2 Motivation for Research 2
1.2.1 Sporting Event Tracking and Goal Detection 2
1.2.2 Tracking and Security for Retail and Merchandise 3
1.2.3 Tracking and Mapping for Medical Applications 4
1.3 Dissertation Outline 5

Chapter 2 – Review of Literature 6
2.1 Sensor Technologies 6
2.2 Types and Characteristics of Magnetic Sensors 7
2.3 Characteristics of Magnetic Fields and Flux Density 9
2.3.1 Remanent Magnetization 13
2.3.2 Magnetic Susceptibility and Permeability 14
2.3.3 Magnetic Source Material 16
2.4 Object Location and Tracking Systems 17
2.4.1 Magnetic Field Based Technique for 3D Position Tracking 17
2.4.2 Magnetic Position and Orientation Tracking System 18
2.4.3 Tracking System using Hall Sensors and Permanent Magnets 20
2.4.4 Characterizations of a Novel Magnetic Tracking System 21
2.4.5 Summary 23
2.5 Positioning in the Presence of Magnetic Noise 24
2.6 Review of Position Estimation and Error Reduction 26

Chapter 3 – Research Approach and Methodology 31

3.1 Developing a Model for a Permanent Magnetic Source 31
3.2 Permanent Magnetic Source and Specifications 34
3.2.1 Magnetic Source Geometry 34
3.2.2 Magnetic Flux Density of Source 36
3.3 Verification of Magnetic Model with Finite Element Modeling 39
3.4 Magnetic Sensor Network and Specifications 43
3.5 Design of Test Apparatus and Sensor Network 46
3.6 Algorithm for Determining 3D Position and Orientation 49
3.7 Position Estimation and Error Reduction 59
3.8 Data Acquisition System and Specifications 65

Chapter 4 – Experimental Approach and Design 69

4.1 Magnetic Sensor and Support Circuitry 69
4.2 Magnetic Sensor Network Layout 77
4.3 Data Acquisition System for a Magnetic Sensor Network 82
4.4 Experimental Testing Apparatus 83
4.4.1 Rotational Experimental Testing Apparatus 83
4.4.2 Linear Experimental Testing Apparatus 85

Chapter 5 – Results 87

5.1 Sensor Network Calibration 87
5.2 Results of Rotational Testing 89
5.3 Results of Linear Testing 96
5.4 Summary of Results 100

Chapter 6 – Conclusion and Recommendations 102

6.1 Conclusion 102
6.2 Recommendations 102

References 104

Appendix A – Magnetic Sensor Component Information 111
Appendix B – Magnetic Sensor PCB Schematic 112
Appendix C – Absolute Positions of Magnetic Sensors 113
Appendix D – Absolute Positions of Center of Sensor Clusters 114
Appendix E – Frequency Response of Unfiltered and Filtered Magnetic Sensors 115
Appendix F – Frequency Response of Power Supply 117
Appendix G – Experimental data for rotation apparatus 118
Appendix H – Experimental data for linear apparatus 124

List of Figures

Figure 1 - Detectable field strengths for various magnetic sensing technologies 7
Figure 2 - Categorization of magnetic sensor applications 8
Figure 3 - Sample magnetic field lines from a bar magnet 9
Figure 4 - Current loop used to define a simple magnetic field 10
Figure 5 - Ideal magnetic dipole and its field lines 12
Figure 6 - Block diagram for magnetic position system 19
Figure 7 - Coordinate system and sensor layout for Hall sensor tracking system 20
Figure 8 - Sensor layout for novel tracking system 21
Figure 9 - Coordinate system for novel tracking system 22
Figure 10 - Vector components of the Earth magnetic field 25
Figure 11 - Plot of recorded magnetic flux density sampled at 1 Hz for a 60 minute duration at Fredericksburg, VA (USGS) 26
Figure 12 - Graphical representation of additive probability density 28
Figure 13 - Block diagram of Kalman Filter 30
Figure 14 - Definition of model coordinate system 33
Figure 15 - Simulated magnetic flux density for 1 kG permanent magnetic source centered at the origin on the x-y plane at z = 0 inches. 35
Figure 16 - Simulated magnetic field lines for normalized permanent magnetic source centered at the origin on the x-y plane at z = 0 ft. 36
Figure 17 - Simulated magnetic flux density of a 1 kG magnetic source at z = 9.84 ft above origin with orientation of 0° about x-axis. 37
Figure 18 - Simulated magnetic field lines of a 1 kG magnetic source at origin with orientation of 0° about x-axis. 37
Figure 19 - Simulated magnetic flux density of a 1 kG magnetic source at z = 9.84 ft above origin with orientation of 90° about x-axis. 37
Figure 20 - Simulated magnetic field lines of a 1 kG magnetic source at origin with orientation of 90° about x-axis. 37
Figure 21 - Simulated magnetic flux density of a 1 kG magnetic source at z = 9.84 ft above origin with orientation of 180° about x-axis. 38

Figure 22 - Simulated magnetic field lines of a 1 kG magnetic source at origin with orientation of 180° about x-axis. 38
Figure 23 - Simulated magnetic flux density of a 1 kG magnetic source at z = 9.84 ft above origin with orientation of 270° about x-axis. 38
Figure 24 - Simulated magnetic field lines of a 1 kG magnetic source at origin with orientation of 270° about x-axis. 38
Figure 25 - Plot of simulated two-dimensional magnetic flux density over control volume from a distance of 12 inches away from magnetic source (with θ = 0°) 40
Figure 26 - Plot of simulated, extruded three-dimensional magnetic flux density over control volume from a distance of 12 inches away from magnetic source (with θ = 0°) 40
Figure 27 - Plot of simulated magnetic flux density over defined control volume. 41
Figure 28 - Analytical model (MATLAB) vs. computational simulation (COMSOL) from a distance of approximately 12 inches away from magnetic source (with θ = 60°) 42
Figure 29 - Analytical model (MATLAB) vs. computational simulation (COMSOL) from a distance of approximately 24 inches away from magnetic source (with θ = 60°) 42
Figure 30 - Analytical model (MATLAB) vs. computational simulation (COMSOL) from a distance of approximately 36 inches away from magnetic source (with θ = 60°) 43
Figure 31 - Plot of the superposition of the magnetic flux densities of a permanent magnet, DC Earth field component, and magnetic noise 44
Figure 32 - Scaled plot of the superposition of the magnetic flux densities to show magnetic noise variations 45
Figure 33 - Scaled plot of magnetic flux density versus distance for a permanent magnetic with surface remanent magnetization Br = 3.309 kG and a noise floor of 4 mG 46
Figure 34 - Sample sensor cluster layout 47
Figure 35 - Zones of sensor network (using centers of clusters) 48
Figure 36 - Magnetic flux density (z-direction) for ideal magnetic dipole located at the center of the sensor network (θ = 0°) 12 inches vertically away from the sensor 50
Figure 37 - Patches (n = 4, 12 sensors) selected from magnetic volume 50
Figure 38 - Simulated plot of the intersection of Patch normal vectors in 3D (left) and 2D (right) space 52
Figure 39 - Intersection of normal vectors in two-dimensional space on the x-y plane 52

Figure 40 - (x,y) position for all combination of point-normal intersections 53
Figure 41 - Plot of elevation angle vs. ratio of simulated sensor values (max/min) for $12 \leq z \leq 48$ in 54
Figure 42 - Plot of simulated rotation angle vs. sensor position 56
Figure 43 - Plot of θ vs. Equivalent B_r in the z-axis based on maximum sensor value 57
Figure 44 - Radial offset percentage for elevated magnet (z = 12, 24, 36, and 48 inches) 58
Figure 45 - Path of projectile with and without AWGN and with applied Kalman filter 64
Figure 46 - Percent error of Kalman filter and smoothed Kalman filter in free-space 64
Figure 47 - Block diagrams of system with single acquisition system 67
Figure 48 - Block diagrams of system with multiple pre-processors 68
Figure 49 - Block diagram of magnetic sensor and support circuitry 70
Figure 50 - Sensor output vs. magnetic field input for HMC1021z [85] 70
Figure 51 - Circuit diagram of differential operational amplifier 72
Figure 52 - Frequency response of single axis magnetic sensor and amplification, filtering circuitry 73
Figure 53 - Magnetic sensor circuit schematic 74
Figure 54 - Transient noise from magnetic sensor and support circuitry 75
Figure 55 - Magnetic sensor (HMC 1021z) noise vs. frequency[85] 76
Figure 56 - Sample PCB including magnetic sensor and support circuitry 76
Figure 57 - Sensor cluster - Positions of magnetic sensors 77
Figure 58 - Simulated sensor network with 12 sensors, 4 sensor clusters 78
Figure 59 - Simulated sensor network with 12 sensors, 15 sensor clusters 79
Figure 60 - Experimental sensor network with 12 sensors 79
Figure 61 - Sensor network response (dB) for magnetic source 1 ft above origin 80
Figure 62 - Sensor network response (dB) for magnetic source 2 ft above origin 81
Figure 63 - Block diagrams of experimental sensor network 83
Figure 64 - Rotational testing apparatus 84
Figure 65 - Magnetic slug holder 84
Figure 66 - Linear testing apparatus 85
Figure 67 - Pre-calibration data 88
Figure 68 - Post-calibration data 88

Figure 69 - Output of magnetic sensors for rotating test apparatus (θ = 0°) 89
Figure 70 - Simulated position for rotating test apparatus using ideal magnetic source as a baseline for systematic error..... 90
Figure 71 - Radial position for rotating test apparatus (θ = 0°, 15 clusters)..... 91
Figure 72 - Position for rotating test apparatus (θ = 0°, 15 clusters)..... 91
Figure 73 - Orientation for rotating test apparatus (θ = 0°, 15 clusters)..... 92
Figure 74 - Percent error for rotating test apparatus (source angle = 0°, 15 clusters)..... 92
Figure 75 - Simulated network with 441 uniformly spaced sensors (27 sensors per ft^2) 94
Figure 76 - θ and φ in simulated network with 441 uniformly spaced sensors (27 sensors per ft^2) 94
Figure 77 - Simulated plot of sensor network density vs. percent error (θ, φ, and z) for a 16 ft^2 sensor network..... 95
Figure 78 - Output of magnetic sensors for linear test apparatus (θ = 0°)..... 96
Figure 79 - Simulated position for linear test apparatus using ideal magnetic source as a baseline for systematic error..... 97
Figure 80 - Position for linear test apparatus (θ = 0°, 15 clusters) 98
Figure 81 - Percent error for linear test apparatus (θ = 0°, 15 clusters)..... 98
Figure 82 - Output of magnetic sensors for rotating test apparatus (θ = 15°) 118
Figure 83 - Radial position for rotating test apparatus (θ = 15°, 15 clusters)..... 118
Figure 84 - Experimental percent error for rotating test apparatus (θ = 15°, 15 clusters)..... 119
Figure 85 - Output of magnetic sensors for rotating test apparatus (θ = 30°) 119
Figure 86 - Radial position for rotating test apparatus (θ = 30°, 15 clusters)..... 120
Figure 87 - Experimental percent error for rotating test apparatus (θ = 30°, 15 clusters)..... 120
Figure 88 - Output of magnetic sensors for rotating test apparatus (θ = 45°) 121
Figure 89 - Radial position for rotating test apparatus (θ = 45°, 15 clusters)..... 121
Figure 90 - Experimental percent error for rotating test apparatus (θ = 45°, 15 clusters)..... 122
Figure 91 - Experimental output of magnetic sensors for rotating test apparatus (θ = 60°)..... 122
Figure 92 - Radial position for rotating test apparatus (θ = 60°, 15 clusters)..... 123
Figure 93 - Experimental percent error for rotating test apparatus (θ = 60°, 15 clusters)..... 123
Figure 94 - Output of magnetic sensors for linear test apparatus (θ = 15°)..... 124
Figure 95 - Three-dimensional position for linear test apparatus (θ = 15°, 15 clusters) 124

Figure 96 - Error for linear test apparatus (θ = 15°, 15 clusters) 125
Figure 97 - Output of magnetic sensors for linear test apparatus (θ = 30°) 125
Figure 98 - Three-dimensional position for linear test apparatus (θ = 30°, 15 clusters) 126
Figure 99 - Error for linear test apparatus (θ = 30°, 15 clusters) 126
Figure 100 - Output of magnetic sensors for linear test apparatus (θ = 45°) 127
Figure 101 - Three-dimensional position for linear test apparatus (θ = 45°, 15 clusters) 127
Figure 102 - Error for linear test apparatus (θ = 45°, 15 clusters) 128

List of Tables

Table 1 - Relative permeabilities for common diamagnetic and paramagnetic elements and compounds 15
Table 2 - Relative permeabilities for common ferromagnetic elements (DC, no saturation) 16
Table 3 - Comparison of ferromagnetic materials 16
Table 4 - Comparison of tracking systems 23
Table 5 - Electromagnetic characteristics for computational simulation constants. 39
Table 6 - Table of magnet characteristics and sensor characteristics used 45
Table 7 - Sampling frequencies for 0.5" and 0.1" resolutions 65
Table 8 - Data acquisition system specifications 66
Table 9 - A/D resolution versus minimum detectable sensor signal 68
Table 10 - HMC 1021z magnetic sensor design characteristics 69
Table 11 - Data acquisition system specifications for NI DAQCard-AI-16XE-50 and NI PCI-6013 82
Table 12 - Summary of results for rotating test apparatus (position) 93
Table 13 - Summary of results for rotating test apparatus 93
Table 14 - Theoretical vs. simulated θ for network with 27 sensors per ft^2 95
Table 15 - Summary of experimental results for linear test apparatus 99
Table 16 - Theoretical vs. simulated z for network with 441 sensors (density of density of 27 sensors per ft^2) 99
Table 17 - Computation speeds of geometrical solver vs. MATLAB iterative solver 101

Nomenclature

∇	Vector differential operator
θ	Angle of elevation
μ_0	Free-space permeability ($H \cdot m^{-1}$)
μ_r	Relative permeability
ρ	Volume charge density
σ	Conductivity
φ	Angle of rotation
χ	Magnetic susceptibility
Ω	Ohm
A	Ampere
A	Magnetic vector potential
A/D	Analog to digital
AC	Alternating current
B	Magnetic flux density (G)
B_r	Remanent magnetization (G)
C	Coulomb
°C	Degrees Celsius
D	Electric flux density ($C \cdot m^{-2}$)
DAQ	Data acquisition
dB	Decibel
DC	Direct current
E	Electric field strength ($V \cdot m^{-1}$)
EKF	Extended Kalman Filter
EMI	Electromagnetic interference
FOV	Field of view
FS	Full scale
G	Gauss
H	Henry
H	Magnetic field strength ($A \cdot m^{-1}$)
Hz	Hertz
in	inch
J	Current Density ($S \cdot m^{-1}$)
k	Kilo (10^3)
KF	Kalman Filter
LMA	Levenberg-Marquardt algorithm
M	Magnetization ($A \cdot m^{-1}$)
m	Magnetic dipole moment ($A \cdot m^2$)
m	Meter
mph	Mile per hour
MRI	Magnetic Resonance Imaging
N	North
Oe	Oersted
PCB	Printed Circuit Board
r	Vector distance
RMS	Root mean squared
RMSE	Root mean squared error
S	Siemens (Ω^{-1})
sec	Second
T	Tesla ($Wb \cdot m^{-2}$)
V	Volt
VDC	Volts (DC)
Wb	Weber
x	x-axis coordinate
y	y-axis coordinate
z	z-axis coordinate

Chapter 1 – Introduction

Magnetic fields and their principles have been well studied and are well defined. Because of this, there are wide spread possibilities for practical applications. Previously researched technical embodiments using magnetic fields include: medical applications [3], theories of biological effects [4], wireless identification [5], thermal processes [6], and audio [7] and video processing [8]. Additionally, magnetic fields can be used for tracking applications.

Current magnetic tracking applications exist for a variety of applications. These active systems are made using both AC and pulsed DC magnetic fields. Generally, AC systems have high resolution and accuracy, but perform very poorly in the presence of conducting magnetic materials such as carbon steel and iron alloys [1]. It is often for this reason that DC systems are employed [9]. It has been suggested that pure DC systems are not always feasible because there is no easy or reliable way to account for the presence of the Earth's magnetic field [2]. The traditional solution to this problem is through the use of pulsed DC magnetic sources. Pulsed DC tracking has the benefit of reducing eddy currents in relatively close proximity to magnetic materials, thus increasing its overall accuracy [2].

It is the purpose of this research to propose, model, and create a magnetic tracking system that has the ability to account for the Earth's magnetic field before, during, and after operation in order to determine the three-dimensional location and orientation of a target object. Position and orientation will be determined by using a network of single-axis magnetic sensors and a priori knowledge of the geometry of the magnetic flux density (B-field) of the source projectile. Knowledge of this geometry was used to create models to determine the rotation and elevation of the magnetic source from the sensor network, as well as the z-axis position. Developing an algorithm that takes advantage of the B-field geometry reduces the amount of computation time necessary for location and tracking applications compared to iterative solutions methods. Additionally, this novel method of using magnetic sources and sensors will describe possible uses in magnetically noisy conditions.

1.1 Research Objective

The objective of this research is to create a system, and develop a novel algorithm, that can successfully locate the three-dimensional position and orientation of a permanent magnet projectile using a network of single-axis magnetic sensors.

This research will discuss the theory behind the proposal, including characteristics of magnetic sensors and magnetic fields with respect to desirable magnetic characteristics (material, shape, and strength), an overview of previous magnetic tracking systems and practical applications, as well as the effect of magnetic noise on the ability to track a magnetic projectile.

From basic principles, equations of an analytical model will be developed for a magnetic source with 5-degrees of freedom, and which will then be compared for accuracy against electromagnetic simulations. Once verified with simulations, an experimental apparatus will be designed and constructed as a proof-of-concept apparatus. Additionally, hardware, including a network of single axis sensors, a data acquisition system, and software solutions for calculating and estimating the position will be developed and tested. Results will show the feasibility of a simplistic one-dimensional sensor network for calculating and tracking the position and orientation of a magnetic projectile in three-dimensional space.

1.2 Motivation for Research

Because of the variety of magnetic sources and magnetic sensing devices, the magnetic tracking system being proposed has a host of possible embodiments. Possible uses for this novel system are described in the sections below.

1.2.1 Sporting Event Tracking and Goal Detection

Sporting events have occupied an important part of our leisure time for decades, and inaccurate calls, even when done inadvertently or accidentally can, and often do, change the outcome of the

game. Often, improper or inaccurate calls by a scoring official also result in a delay in the game and loss of momentum for both the teams and the spectators. In some sports, such as ice hockey, the actions associated with the scoring process can create significant problems. This is particularly true when the field of view is obscured by players or their equipment. Additionally, the speed of the puck and the actions and interactions of the skaters surrounding it can easily hide the progress on, or near, the goal line.

To facilitate the calls of the officials, video equipment and the availability of video play-back can aid in the decision making process. [10], [11] In some applications [12], [13], high speed video cameras blanket the rink, covering the visible ice from as many angles as possible. Unfortunately, even all of this visual monitoring equipment can be blocked, making this situation even more difficult to call. Clearly what is needed is a detection protocol where the players and their equipment are transparent to the system.

Attempts have been made in the past to track the puck on the ice. [14] This was mainly for television viewers to be able to locate the puck while in action. Previous methods attempting to perform goal detection were based solely on visible recognition, and therefore were not accurate enough for goal tracking because the puck is often occluded by the goal keeper or other players. The novel method of using magnetic sources and sensors described in this document will propose a tracking system that is not dependant on visual interpretation.

1.2.2 Tracking and Security for Retail and Merchandise

In another possible embodiment, a small scale magnetic system could be used to track merchandise in-store or in-warehouse for security or inventory purposes. Much like magnetic security devices that are used to protect expensive electronics in stores today, a small magnetic source could be embedded in product packaging and be used to detect concealed merchandise leaving the premises, as well as its movements from warehouse, to store, to consumer.

Although there will not be enough information to uniquely identified specific products, this system could be used to quickly identify packages marked as expensive, perishable, dangerous,

or otherwise differentiable. A system such as this would no longer make removing specialized security devices necessary, which assumes that the product re-entering the store for return does not interfere with the inventory management system.

A simple implementation, similar to the sport event embodiment, includes a small, inconspicuous magnetic sensor network that could be deployed around doorways, thresholds, or in specific areas of warehouses or storage areas with the ability to detect when merchandise enters and exits. This sensor network could be connected to a data acquisition system capable of detecting a magnetic signal as small as a few hundred milligauss. Information about the product and number of products could be then directed to the store's inventory management system.

1.2.3 Tracking and Mapping for Medical Applications

In another possible embodiment, a magnetic source could be used to track bodily functions or map organs such as the intestinal tract or blood stream. This sensor grid would consist of an arrangement of magnetic sensors incorporated in a suitable substrate sheet that is embedded in an examination table. Again, due to the nature of the magnetic field, and its ability not to be limited to line of site, tracking magnetic sources in the body will be much like tracking outside of the body.

Additional modifications will be needed for inter-body tracking. The first and foremost will be the size and strength of the magnetic signature. The size of the source will be dictated by the application, “milli” scale for intestinal tract and “nano” scale for blood / vein mapping. Because of the size / strength relationships between most magnetic materials the strength of the magnet will also need to be reduced. Current magnetic resonance imaging (MRI) machines use magnetic field between 4.7 kG and 47 kG [15], but these fields are exterior to the body and are then reduced over distance. Although the body is able to tolerate large static magnetic fields, it does not fare as well with dynamic magnetic fields [16]. If a magnetic source was to be introduced to the body, it would need to be small, as to not create a large dynamic magnetic field, which has been linked to leukemia [17].

Clarity and precision will be critical in this embodiment. Since the patient will be confined to the examination table, the magnetic sensors will only need to have a vertical range of the width of a body (approximately 18 in), instead of multiple feet as would be needed for large scale object tracking. In order to ensure needed details, the sensor network, or sensor substrate, will need to be denser. It may be necessary for several hundred sensors to be used and in varying configurations for suitable clarity. All data collection equipment, filters, and prediction models will be similar, as in the previous embodiments.

1.3 Dissertation Outline

This document is structured in the following format. Chapter 1 is the introduction, which also contains the purpose and objectives for performing the research, motivation and possible embodiments of the technology as well as this outline for the document. Chapter 2 contains a review of past literature that is applicable to the current research topic, including applicable sensor technologies, electromagnetic theory pertinent to tracking magnetic objects, developed tracking systems and their algorithms, and position and error estimation techniques. Chapter 3 contains the research approach and methodology, which includes specifications for magnetic source and sensor, algorithms for determining position, and specifications for a data acquisition system to collect and process information. Chapter 4 contains the experimental approach and design, including the selected components and outlining their interactions. Chapter 5 contains an outline of experimental testing procedures and experimental results for the rotational and linear experimental apparatuses, and a summary of experimental results. Finally, Chapter 6 contains conclusions and the recommendations for future work.

Chapter 2 – Review of Literature

This chapter will provide a review and background of the types of sensors and sensing technologies available, as well as a scheme for classification and typical usage. This chapter will also review previous embodiments of AC and pulsed DC magnetic location and tracking systems focusing on materials, implementation, and algorithms. Additionally, a review of works emphasizing position estimation and error reduction will also be included. This information will be critical in understand the design proposed in future sections of this document.

2.1 Sensor Technologies

Sensor technologies can be lumped into two primary groups—active sensing and passive sensing. Okamoto [18] states that the sole difference between the two is the type and source of electromagnetic waves being generated by the system. Active sensors have an internal power source, and thus are able to emit their own energy, or modulated signature. Passive sensors, on the other hand, have only the power of the receiving system, and therefore are only able to receive and re-emit (in the case of passive RFIDs) electromagnetic waves [19].

Okamoto mentions that passive sensing technologies, because of their use of naturally occurring electromagnetic (EM) waves, generally suffer from a reduced range. Active sensing technologies, which generate their own EM waves, and are easier to distinguish from naturally occurring EM waves [20]. This allows for an increase in detectable range and accuracy, but it often comes at a cost of complexity. Additionally, active sensors can be modulated, pulsed, or otherwise altered to enhance the range of resolution [18]. This alteration is done at the cost of power consumption, size, shape, and complexity. This increased power consumption allows active sensors to have increased measuring capabilities, such as monitoring phase and Doppler shifts. Passive sensors, however, operate under fewer constraints because the only power available is power received by the receiver system.

Additionally, Cheng and Sridhar [21] comment on the field of view (FOV) of both sensor technologies. They state that active sensors, although offering very high resolution, suffer from a narrow FOV. Passive sensors, on the other hand, offer an incredibly wide FOV, but often lack the precision that high resolution sensors offer [21].

2.2 Types and Characteristics of Magnetic Sensors

Magnetic sensors have been used for over two millennia, with the earlier sensors being used for direction finding [22]. Better understanding of magnetic fields, and their applications, have expanded the possible use for such sensors past navigation alone. Such sensors are currently being used heavily in the field of object tracking and spatial orientation [23], [24], [25], [26], [27]. Various types of sensor technologies exist, including: magnetometers (search-coil, flux-gate, optically pumped, nuclear-precession, SQUID, magnetoresistive, and fiber-optic), hall-effect, magnetodiode, magnetotransistor, and magneto-optical. These technologies, as well as their respective detectable field strength can be seen in Figure 1.

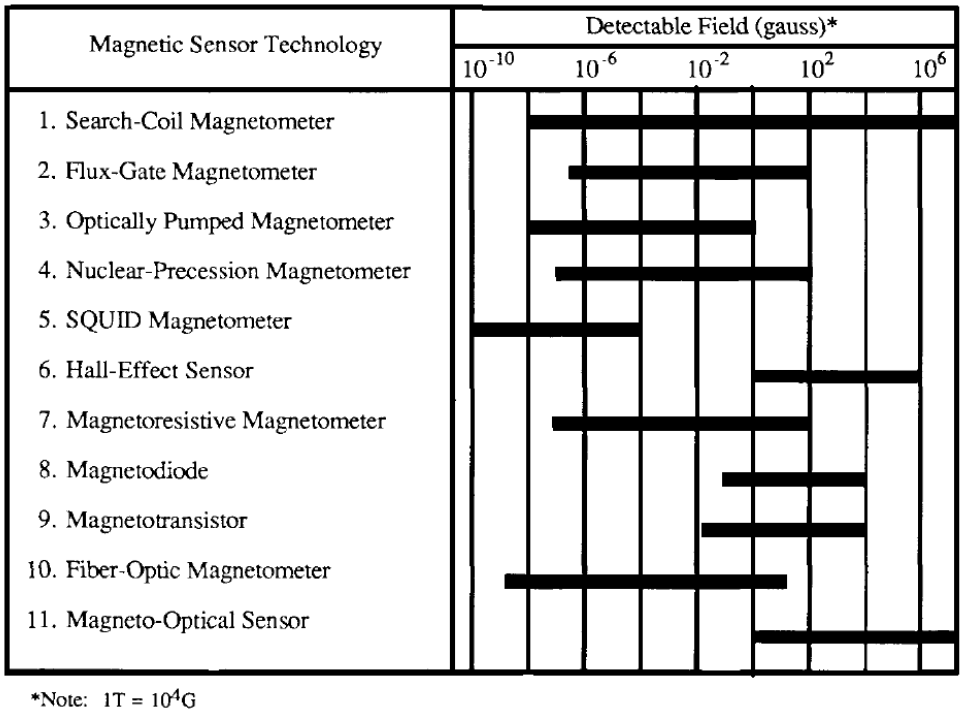

Figure 1 - Detectable field strengths for various magnetic sensing technologies [28]

Caruso et al. [22] classify magnetic sensors into three categories: low field, medium field, and high field sensing. Low field sensors are defined as sensors that are able to detect less than 1 μG. Sensors able to detect magnetic field strengths of 1 μG to 10 G will be classified as medium field sensors. Sensors with the ability to detect over ten gauss are said to be high field sensing magnetic sensors

These magnetic sensing technologies can also be sorted by how the sensor is being used in relation to the Earth's magnetic field. Lenz [28] defines three categories — high, medium, and low sensitivity. The boundary between the first and second categories is defined by the magnitude of the Earth's magnetic field (approximately 0.1 to 1 Gauss). This boundary acts as a noise floor or ceiling. The boundary between the second and third categories is defined by the level at which the Earth's magnetic field is stable. This range can vary between 10^{-3} to 10^{-6} Gauss depending upon the frequency range. Figure 2 shows the most common applications and most common sensors for each category [28].

10^{-5} G		1 G
Category 3 **High Sensitivity**	**Category 2** **Medium Sensitivity**	**Category 1** **Low Sensitivity**
Definition Measuring field gradients or differences due to induced (in Earth's field) or permanent dipole moments	**Definition** Measuring perturbations in the magnitudes and/or direction of Earth's field due to induced or permanent dipoles	**Definition** Measuring fields stronger than Earth's magnetic field
Major Applications · Brain function mapping · Magnetic anomaly detection	**Major Applications** · Magnetic Compass · Munitions fuzing · Mineral Prospecting	**Major Applications** · Noncontact switching · Current measurement · Magnetic memory readout
Most Common Sensors · SQUID Gradiometer · Optically pumped magnetometer	**Most Common Sensors** Search-coil magnetometer Flux-gate magnetometer Magnetoresistive magnetometer	**Most Common Sensors** · Search-coil magnetometer · Hall-effect sensor

Figure 2 - Categorization of magnetic sensor applications [28]

2.3 Characteristics of Magnetic Fields and Flux Density

To better understand the research problem, a brief theory behind electromagnetism is presented. The derivations shown here start from fundamental principles and move towards project-specific models. This section will include a discussion of magnetic fields, as well as covering permanent magnetic fields and magnetic materials.

For the purposes of examining the low frequency magnetic field, we can ignore the electric flux density as well as the electric field strength, and more closely focus on the magnetic flux density (B-field) and the magnetic field strength (H-field). The most familiar source of a magnetic field is from a bar magnet [29]. The bar magnet has two poles, denoted north (N) and south (S) which have equipotential lines connecting the two, illustrated in Figure 3.

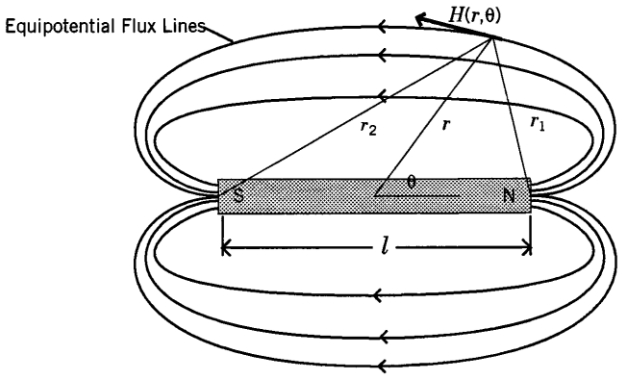

Figure 3 - Sample magnetic field lines from a bar magnet [29]

Although non-visual, the presence of a magnetic field can be determined by measuring either the magnetic flux density (B-field) or the magnetic field strength (H-field). They are related in free-space via:

$$\boldsymbol{B} = \mu_0 \boldsymbol{H}, \tag{2.3.1}$$

where $\boldsymbol{B}$ is the magnetic flux density, μ_0 is the free space permeability, and $\boldsymbol{H}$ is the magnetic field strength.

The properties of magnetic fields differ in the presence of matter. This is introduced as the material magnetization. As shown in many texts [30], [31], [29], [32], the magnetic flux density,

$\boldsymbol{B}$, of a magnetic source has two components—the magnetic field strength, $\boldsymbol{H}$, and the magnetization of a magnet, $\boldsymbol{M}$.

$$\boldsymbol{B} = \mu_0(\boldsymbol{H} + \boldsymbol{M}), \tag{2.3.2}$$

where $\boldsymbol{B}$ is the magnetic flux density, μ_0 is the free space permeability, $\boldsymbol{H}$ is the magnetic field strength, and $\boldsymbol{M}$ is the magnetization of a magnetic material.

To further examine characteristics of the B-field, attributes of the H-field and the magnetization of the material must first be explored. Macintyre [29] states that, when distance r is much greater than the largest dimension of the magnetic source, the H-field of magnetized objects can be determined by the following equation.

$$\boldsymbol{H} = \frac{3(\boldsymbol{m} \times \hat{\boldsymbol{r}}) \cdot \hat{\boldsymbol{r}} - \boldsymbol{m}}{|\boldsymbol{r}|^3}, \tag{2.3.3}$$

where $\boldsymbol{H}$ is the magnetic field intensity, $\boldsymbol{r}$ is the vector distance between source and measurement, $\hat{\boldsymbol{r}}$ is a unit vector along $\boldsymbol{r}$, and $\boldsymbol{m}$ is the magnetic dipole moment.

To aid in the description on magnetic dipoles, moments, and fields, current loops are generally used. Figure 4 illustrates an elementary current loop "used to represent the basic source of a magnetic field … current loops are assumed to be small with respect to the distance of observation" [33].

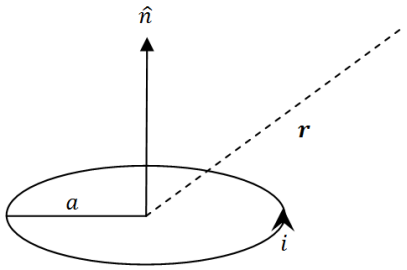

Figure 4 - Current loop used to define a simple magnetic field [33]

Using this figure as a guide, an equation for the magnetic dipole moment, $\boldsymbol{m}$, can be developed using the right-hand rule.

$$\boldsymbol{m} = i\pi a^2 \hat{\boldsymbol{n}}, \tag{2.3.4}$$

where $\boldsymbol{m}$ is the magnetic dipole moment created from a small current loop with respect to the observer distance, $\boldsymbol{r}$, i is the current flow around the loop of radius a, and $\hat{\boldsymbol{n}}$ is the unit vector normal to the current loop.

The magnetization can be directly related to the magnetic dipole moment ($\boldsymbol{m}$) and its unit volume via the following equation [29].

$$\boldsymbol{M_i} = \frac{\boldsymbol{m_i}}{volume}, \tag{2.3.5}$$

where $\boldsymbol{M_i}$ is the magnetization of a magnetic material and $\boldsymbol{m_i}$ is the magnetic dipole moment.

The total magnetization is also directly related to the net magnetic dipole moment ($\boldsymbol{m}$) via the following equation.

$$\boldsymbol{M} = \sum_{\mathrm{i}=1}^{\mathrm{n}} \frac{\boldsymbol{m_i}}{volume}, \tag{2.3.6}$$

where $\boldsymbol{M}$ is the total magnetization of a magnetic material and $\boldsymbol{m_i}$ is the incremental magnetic dipole moment, and n is the number of infinitesimal dipole segments.

Using (3.2.2), $\boldsymbol{B}$ can be rewritten just in terms of the magnetic dipole moment.

$$\boldsymbol{B} = \mu_0 \sum_i \left(\frac{3(\boldsymbol{m_i} \times \hat{\boldsymbol{r}}) \cdot \hat{\boldsymbol{r}} - \boldsymbol{m_i}}{|\boldsymbol{r}|^3} + \frac{\boldsymbol{m_i}}{volume} \right), \tag{2.3.7}$$

where $\boldsymbol{B}$ is the magnetic flux density, $\boldsymbol{r}$ is the vector distance between source and measurement, $\hat{\boldsymbol{r}}$ is a unit vector along $\boldsymbol{r}$, and $\boldsymbol{m_i}$ is the incremental magnetic dipole moment.

From this derivation, based on a current carrying wire, it can be seen that the magnetic field decays at a rate of r^{-3} and is only dependent upon the magnetic dipole moment. This will be useful later in determining sensor position over the maximum detectable distance, r.

However, the B-field, in this form, is typically modeled as an ideal dipole, which is identical to that of a current carrying wire in the far field. [33] The ideal dipole is the most basic model in electromagnetism. It has north and south poles, and is illustrated in Figure 5.

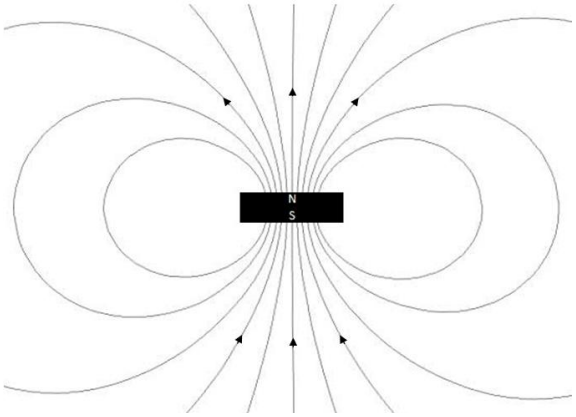

Figure 5 - Ideal magnetic dipole and its field lines

The magnetic flux density of the dipole can classically be defined as the curl of the magnetic vector potential [34]. The magnetic vector potential, $\boldsymbol{A}$, of an ideal magnetic dipole can be defined as shown in (2.3.8) [35]:

$$\boldsymbol{A}(\boldsymbol{m},\boldsymbol{r}) = \frac{\mu_0}{4\pi} \cdot \frac{(\boldsymbol{m} \times \hat{\boldsymbol{r}})}{|\boldsymbol{r}|^2}, \tag{2.3.8}$$

where $\boldsymbol{A}$ is the magnetic vector potential, $\boldsymbol{r}$ is the vector distance between source and measurement, $\hat{\boldsymbol{r}}$ is a unit vector along $\boldsymbol{r}$, μ_0 is the free space permeability, and $\boldsymbol{m}$ is the magnetic dipole moment.

The B-field is defined as the curl of $\boldsymbol{A}$ with the addition of the Earth's magnetic flux density [34], where:

$$\boldsymbol{B}(\boldsymbol{m},\boldsymbol{r}) = \nabla \times \boldsymbol{A}(\boldsymbol{m},\boldsymbol{r}) + \boldsymbol{B}_{EARTH}, \text{ or} \tag{2.3.9}$$

$$\boldsymbol{B}(\boldsymbol{m},\boldsymbol{r}) = \frac{\mu_0}{4\pi} \cdot \nabla \times \frac{(\boldsymbol{m} \times \hat{\boldsymbol{r}})}{|\boldsymbol{r}|^2} + \boldsymbol{B}_{EARTH} \tag{2.3.10}$$

Mathematical simplification of the del (∇) operator results in (2.3.11)

$$\boldsymbol{B}(\boldsymbol{m},\boldsymbol{r}) = \frac{\mu_0}{4\pi} \cdot \left[\frac{3\hat{\boldsymbol{r}}(\hat{\boldsymbol{r}} \cdot \boldsymbol{m}) - \boldsymbol{m}}{|\boldsymbol{r}|^3}\right] + \boldsymbol{B}_{EARTH} \quad \textbf{(2.3.11)}$$

where $\boldsymbol{B}$ is the magnetic flux density, $\boldsymbol{B_{EARTH}}$ is the magnetic flux density of the Earth **,** $\boldsymbol{r}$ is the vector distance between source and measurement, $\hat{\boldsymbol{r}}$ is a unit vector along $\boldsymbol{r}$, μ_0 is the free space permeability, and $\boldsymbol{m}$ is the magnetic dipole moment.

This model, as a function of the magnetic dipole moment and the distance between the source and sensor, is very similar to that of a current carrying wire shown in (2.3.7) when accounting for all incremental components of the magnetic dipole moment. Because at distances far away (magnetically), magnetic sources have fields that resemble an ideal dipole. This will be the magnetic model used in the tracking application described in the following sections of this document. This dipole model also accounts for the magnetic noise generated from the Earth's magnetic field [36].

2.3.1 Remanent Magnetization

Discussed in the previous section, the magnetic field is dependent upon the material it passes through. Equation (3.2.2) suggests that there is a second factor in the determination of the B-field, $\boldsymbol{M}$, the magnetization of a material. Because neither the magnetic dipole moment nor the magnetization have a comparable meaning, a new term, $\boldsymbol{B_r}$, is introduced. $\boldsymbol{B_r}$ is termed "remanence" or "remanent magnetization" and is defined as the value of the B-field when there is no external H-field, and is the product of the magnetization and free space permeability [37].

$$\boldsymbol{B_r} = \mu_0 \boldsymbol{M}, \quad \textbf{(2.3.1.1)}$$

where $\boldsymbol{B_r}$ is the remanent magnetization, μ_0 is the free space permeability, and $\boldsymbol{M}$ is the magnetization of a magnetic material.

(3.2.2) can be substituted yielding a new definition for the B-field:

$$\boldsymbol{B} = \mu_0 \boldsymbol{H} + \boldsymbol{B_r}, \quad \textbf{(2.3.1.2)}$$

where $\boldsymbol{B}$ is the magnetic flux density, $\boldsymbol{B_r}$ is the remanent magnetization, μ_0 is the free space permeability, and $\boldsymbol{H}$ is the magnetic field intensity.

Physically, the remanent magnetism value, $\boldsymbol{B_r}$, is magnetism that is left behind once a magnetic field is applied and removed [35]. This can be thought of as the energy that is stored in each and every permanent magnet and magnetic material. The "strength" of permanent magnets is determined by their remanent magnetization.

2.3.2 Magnetic Susceptibility and Permeability

Jiles [38] claims that magnetic materials are defined by their “bulk susceptibility” or magnetic susceptibility (χ). Jiles [38] also states that under a constant temperature and within a relatively small magnetic field, diamagnetic and paramagnetic susceptibilities are constant. This allows for the following:

$$\mathbf{M} = \chi \mathbf{H}, \quad \textbf{(2.3.2.1)}$$

where $\boldsymbol{M}$ is the magnetization of a magnetic material, χ is the material susceptibility, and $\boldsymbol{H}$ is the magnetic field strength.

From (3.2.2),

$$\mathbf{B} = \mu_0(1 + \chi)\mathbf{H}, \quad \textbf{(2.3.2.2)}$$

$$\mathbf{B} = \mu_0 \mu_r \mathbf{H}, \text{ and} \quad \textbf{(2.3.2.3)}$$

where $\boldsymbol{B}$ is the magnetic flux density, χ is the material susceptibility, μ_0 is the free space permeability, μ_r is the relative permeability, μ is the total magnetic permeability, and $\boldsymbol{H}$ is the magnetic field strength.

This result allows a comparison between The B- and H-fields at low magnetic field strengths without taking the magnetization $\boldsymbol{M}$ into account [31]. This condition also allows for the introduction of relative permeability, μ_r, which is the comparison for how susceptible a material

is to be magnetized. Inan [31] lists relative permeability for several common diamagnetic and paramagnetic materials at standard temperature and pressure, which can be seen in Table 1.

Table 1 - Relative permeabilities for common diamagnetic and paramagnetic elements and compounds [31]

Material	**Relative permeability (μ_r)**
Air	1.00000037
Aluminum	1.000021
Copper	0.9999906
Lead	0.9999831
Water	0.9999912

From (2.3.2.3), magnetic permeability is comprised of two components: relative permeability and permeability of free space, as seen in the equation below.

$$\mu = \mu_0 \mu_r, \qquad \textbf{(2.3.2.4)}$$

where μ is the magnetic permeability, μ_0 is the free space permeability, and μ_r is the relative permeability.

Given (2.3.2.4), that magnetic permeability is comprised of relative permeability and the permeability of free space, diamagnetic and paramagnetic materials from Table 1 can be assumed to have a magnetic permeability equal to that of permeability in free space ($\mu_r = 1$). This is significant in the area of electromagnetics, because all of these mediums are virtually identical to a magnetic field.

This, however, is not the case for ferromagnetic materials. Moskowitz [39] states, "ferromagnetic materials are usually what we consider being magnetic (i.e. behaving like iron)". Inan [31] lists relative permeability for ferromagnetic elements at standard temperature and pressure, which can be seen in Table 2. These permeabilities are generally frequency dependent above approximately 10 kHz [40].

Table 2 - Relative permeabilities for common ferromagnetic elements (DC, no saturation) [31]

Material	Relative permeability (μ_r)
Cobalt	250
Iron	280000
Nickel	600
Steel	100

Relative permeabilities in the table above range from hundreds to hundreds of thousands. As the relative permeability of a material increases, it can better support the formation of a magnetic field inside that medium [31]. These materials would not make a suitable sensor network medium, but high mu materials are one of the components to an ideal magnetic target.

2.3.3 Magnetic Source Material

Based upon the descriptions of magnetic classifications, ferromagnetic materials will be examined for potential use as the magnetic source. Heck [41] identifies the ferromagnetic elements (iron, cobalt and nickel) and gives an in-depth discussion on the origin of magnetic materials based upon their composition. Petrie [42] has identified significant advantages and disadvantages with some of today's most common permanent magnetic sources. A summary of these sources can be seen in Table 3.

Table 3 - Comparison of ferromagnetic materials [42]

Magnetic Type	Advantages	Disadvantages
Neodymium Iron Boron	Highest energy material Low cost Many property combinations available	New design typically required for use Low maximum temperature use Can be difficult to handle due to strength Processing is difficult to control and automate
Rare Earth Cobalt	High energy at room temperature Many property combinations available Straight-line demagnetization curve	Expensive Materials Can be difficult to handle due to strength High field strength needed to fully magnetize
Ferrite Magnets	Low material cost Many property combinations available Lower magnetizing strength needed High electrical resistance	Low energy Resistance to demagnetization reduced Brittle

Alnico	Mature product with many producers High maximum operating temperatures Corrosion resistant Low processing cost Many possible shapes and sizes	Uses strategic materials Low coercivity Requires magnetization after assembly

Due to the manufacturing and processing techniques, neodymium magnets have only become a contender for such tracking applications in the last decade. Because of this high energy potential (large B_r) and low cost, these magnets are a logical choice for this research application.

2.4 Object Location and Tracking Systems

In this section, several systems used for tracking an object's position and orientation will be reviewed and critiqued. The applications discussed in this section are used for tracking objects, specifically discussing sensor type, range, and magnetic field strength.

2.4.1 Magnetic Field Based Technique for 3D Position Tracking

Madawala and Pillay [43] have examined the use of magnetic sensors for three-dimensional tracking. Specifically, they proposed a simple and inexpensive way to track multiple garments during the wash cycle of a standard size washing machine. This was performed by placing small magnetic sensors on swatch test samples, and then placing them in the wash bin of a standard washing machine. The sensors used for this experiment were single axis Hall Effect magnetic sensors. Three of these sensors were placed orthogonal to one another, and attached to the test garment in order to determine its location in three-dimensional space.

The wash basin was fitted with wound coils oriented in a way such that asymmetrical magnetic fields were created in the cylinder. This allows custom software to be able to track the swatch throughout the entire wash cycle. Ideally, a coil design would be created such that a unique magnetic signature would exist at all points in the wash basin.

To overcome the fact that multiple identical magnetic signatures exist in the wash basin, a calibration method has to be created to determine the exact position of the garment in three-dimensional space in the basin. In order to calibrate the system, a number of data points were recorded to determine the magnetic field strength. These numbers were then stored in a lookup table in order to be referenced at a later time. The location of the garment can be predicted by measuring the actual magnetic field signature and comparing it to that of the lookup table, but this is not done in real-time.

Several measurements may need to be recorded in order to find the initial position of the garment. Once the initial position is determined, a method was then determined to track the garment. The method used was to determine the closest match in the lookup table that was in the range of the constraints of the system—how fast could the garment move in the wash cycle between readings, given the rotational speed of the washing machine. During this process, the sensing coils move more than the garment (sensor) moves.

In the experimental procedure, test setup used a 3-coil configuration with four turns powered with a DC source of 18 A. The frame of reference for the system is traveling at approximately 60 – 100 revolutions per second, and the recording rate of the system was set at 1 Hz. Experimental results show that this configuration is able to track 83.3% of the space in the cylinder. The location of the sensor in the outer periphery (closest to the 3-coil loop) was unable to be located, probably due to the limitations of the Hall Effect sensors. The maximum detectable distance of this system is approximately 1 inch. The Hall Effect sensors, used due to their ease of setup and cost, can be replaced by other, more accurate magnetoresistive sensors, for production use.

2.4.2 Magnetic Position and Orientation Tracking System

Raab et al. [44] have also developed a magnetic position and orientation tracking system. Unlike its counterparts, this system uses a three-axis magnetic sensor in addition to an active three-axis magnetic source. The authors discuss the possibilities of using a buried magnetic dipole receiver to capture signals from four or five three-axis sensors to determine the location along a perimeter. A block diagram of such a system can be seen in Figure 6.

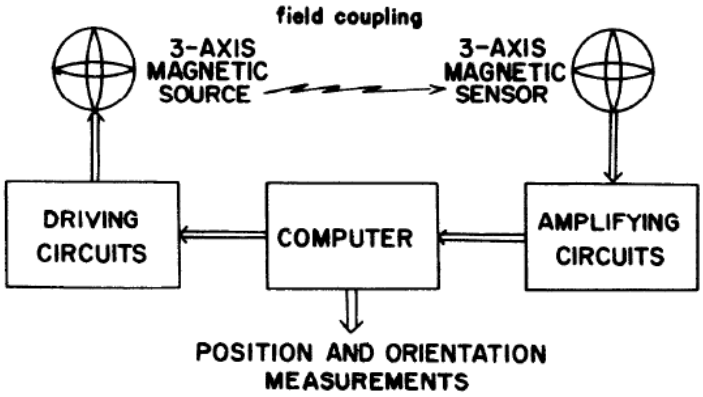

Figure 6 - Block diagram for magnetic position system [44]

The system developed uses a three-axis magnetic sensor and a three-axis magnetic dipole source with three excitation ranges (used to determine position and orientation). In order to simplify calculations and computations, the source excitation and sensor outputs are represented as vectors—where each of the three excitation states that are used are linearly independent of one another [44].

The system is designed in such a way that the source and sensors can be regarded as point sources which "tracks the position and orientation of the sensor by determining small changes in the coordinates and then updating the previous measurements" [44]. The authors' state, "applications of this system use source and sensor loops whose diameters are small in comparison to the distance separating them" [44]. It is for this reason that the sources and sensors can then be regarded as point sources and point sensors. The wavelength of the excitation signal can then be manipulated such that the quasi-static, or near-field, components are most significant. Using the three-axis sources and sensors, the properties of orthogonality can be exploited to determine the position and orientation.

This system is designed to use a 12 bit analog-to-digital converter with update rates between 30 and 120 Hz. The system is able to track objects by updating the previously recorded states by a small incremental change. The maximum range for this system is approximately 40 inches. This system, however, has several limitations; the first is that it must acquire a measurement in order to make a tracking position estimate. If for some reason a measurement cannot be made, the

system will take several iterations in order to determine position and orientation. The second is that this model is based on small angle approximations over small distances. If larger angles are measured, considerably large angle errors can be introduced into the system

2.4.3 Tracking System using Hall Sensors and Permanent Magnets

Schlageter et al. [36] analyze the use of Hall Effect sensors to track the position of a permanent magnet. This system uses sixteen identical Hall Effect sensors in a uniform grid as its sensor platform. The source is a permanent magnet. The layout for this system can be seen in Figure 7.

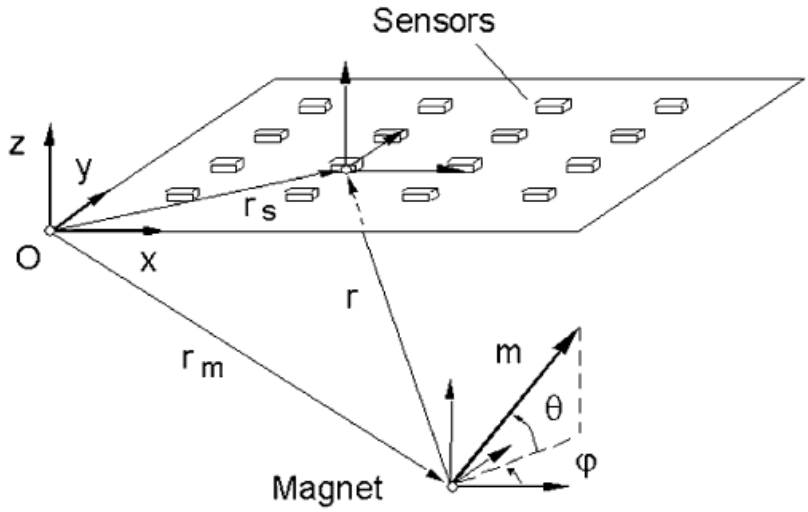

Figure 7 - Coordinate system and sensor layout for Hall sensor tracking system [36]

The authors use the Levenberg-Marquardt algorithm (LMA) shown in [45] to determine the coordinates of the magnet. LMA is a trust based, least squared minimizing method routine used for mainly nonlinear functions [45]. Quite adaptive and robust at tracking data, LMA has the ability to switch between method of steep and shallow descent. Additionally, this system is able to detect the magnetic source up to a range of 5.5 inches with a detectable magnetic field of 150 mG. This system is capable of tracking objects with a sampling frequency up to 50 Hz, which is limited by its computational method (LMA).

This system takes the magnetic field of the Earth into account. This background noise is detected and applied during a calibration phase, before the system is used to track the magnetic source. The authors state a major limitation of this system—the system will be ideal only if the transient magnetic background noise remains relatively consistent, and there is no change in the field's homogeneity (there is no introduction of large magnetic sources). If either of these occurs, the accuracy of the system will decrease.

Schlageter et al. introduce additional valuable information about ambient and system noise that can be applied to magnetic tracking. The authors claim, "as long as we are interested in low frequency applications, the main extrinsic noise is inhomogeneity of the environmental magnetic field, including the earth magnetic field" [36]. They also claim the main cause of intrinsic noise is the 1/f noise due to sensor noise which is discussed further in [36] and [46]. The authors claim the system has accuracy of ±0.21 inches while detecting B-fields of approximately 150 mG.

2.4.4 Characterizations of a Novel Magnetic Tracking System

Sherman et al. [47] continue to examine the work of Schlageter et al [36], [46] analyzing the use of Hall Effect sensors to track the position of a permanent magnet. This modified system now uses 27 identical Hall-effect sensors in a modified grid (Figure 8) as its sensor platform.

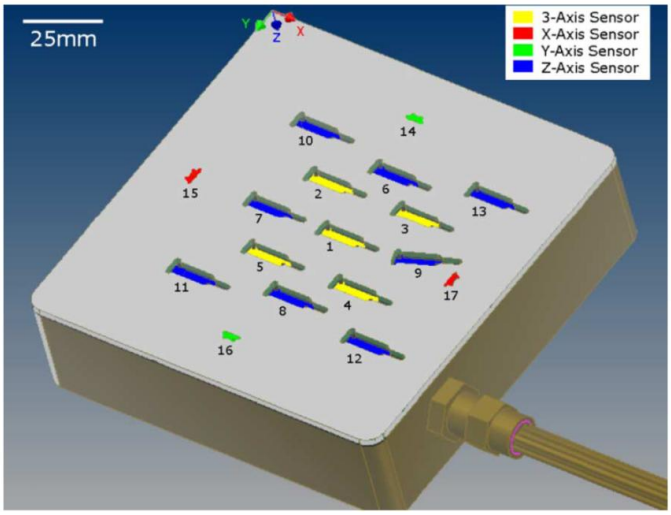

Figure 8 - Sensor layout for novel tracking system [47]

Again, the source used is a permanent magnet. The sensor layout for this system can be seen in Figure 7.

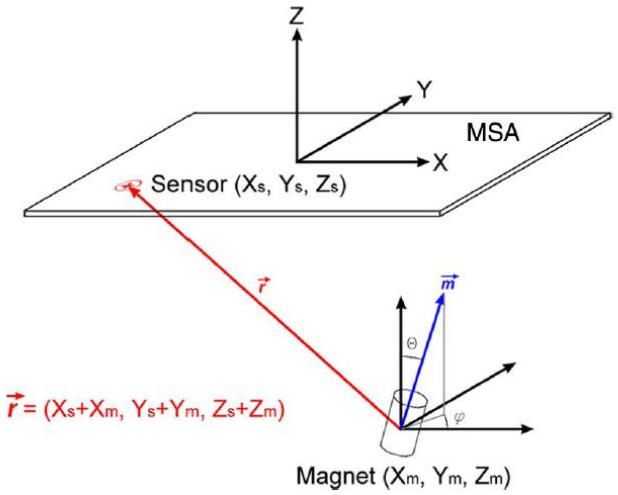

Figure 9 - Coordinate system for novel tracking system [47]

For the magnetic source, the authors use two permanent magnets. The first, for distances less than 6 in, is 14.25 kG with a 0.079 inch diameter. The second, for distances less than 13 inches, is 13.1 kG with a 0.18 inch diameter. The authors use the following equation to estimate position:

$$\boldsymbol{B} = \begin{bmatrix} B_x \\ B_y \\ B_z \end{bmatrix} = \frac{\mu_o m}{4\pi r^3}\left(3\begin{bmatrix} x \\ y \\ z \end{bmatrix}\frac{xsin\theta cos\varphi + ysin\theta sin\varphi + zcos\theta}{r^2} - \begin{matrix} sin\theta cos\varphi \\ sin\theta sin\varphi \\ cos\theta \end{matrix}\right) \qquad \textbf{(2.4.4.1)}$$

The algorithm described is two-phased. The initial position was set to (0,0,B_z). The first phase is to assume a value for θ and φ (both set to zero), and then to solve for x, y, and z. The second phase is using these values to solve for θ and φ. Once stabilized, this method continues to track the magnetic source.

The authors again use the Levenberg-Marquardt algorithm (LMA) shown in [45] to find the coordinates of the magnetic source. This system is able to detect the magnetic source up to a range of 11.8 inches. This system is designed to capture 1500 samples at a sampling frequency of

4 kHz from each sensor. Although this system is able to track to within ±4º accuracy, this model neglects ambient magnetic interference.

2.4.5 Summary

Several applications for tracking an object's position and orientation have been reviewed. Most of these applications used some type of small perturbation algorithms for tracking, with different types of sources and sensors to do the job. Most of the systems also require elaborate, multiple axis receivers. Although successful at tracking relatively slow moving object over small ranges, none of the addressed systems are able to track objects over larger distances. Half of the systems examined also require both a powered source and receiver. Table 4 compares the results in this section to the desired results of the proposed system.

Table 4 - Comparison of tracking systems

Authors	Sensor Type	Source Type	Range	Sampling Freq.	Accuracy
Madawala and Pillay	Hall Effect	Coil windings	1 in	1 Hz	± 0.59 in
Raab et al.	Magnetoresistive	3-axis magnetic dipole	39 in	30-120 Hz	NR*
Schlageter et al.	Hall Effect	Permanent Magnet	5.5 in	50 Hz	± 0.59 in
Sherman et al.	Hall Effect	NdFeB Magnet	12 in	100 Hz	± 0.21 in
Proposed System	Magnetoresistive	NdFeB Magnet	24-36 in	> 120 Hz	~ 0.2 in

NR*: information not reported by source.

The intent of the proposed system is to maintain the detectable range and accuracy of the previously reviewed systems (Table 4) while using a simple permanent magnet target moving in three-dimensional space using the method proposed in this document.

While most systems presented here are able to track and locate objects within the range of inches, the proposed system will track an object up to an approximate range of 2 to 3 ft, limited primarily by the Earth's field acting as a noise floor. A successfully system will include a sensor

package capable of detecting a large magnetic field, ranging from the kilo-Gauss range (to detect a nearby magnetic source) to the milli-Gauss range (to detect perturbations in the Earth's magnetic field). A magnetoresistive sensor will be shown to be adequate for this job. A source that is “strong enough”, or one that has a high remanent magnetism, is also needed. Rare Earth magnets, such as a Neodymium (NdFeB) magnet, will be shown to be well suited for this task; this is mainly due to the fact that they require no additional excitation energy.

2.5 Positioning in the Presence of Magnetic Noise

Earlier work in magnetic tracking has shown that there are many pitfalls with passive sensing (with using a DC or permanent magnetic source). One reason, and the main reason modulated signals were developed, was to deal with random electromagnetic phenomena, specifically ambient magnetic noise.

With regards to the proposed system, magnetic noise can be categorized into either intrinsic or extrinsic noise. Intrinsic noise can be attributed to either the magnetic source, the acquisition system, or noise internal to the system. Bittel [48] discusses noise of ferromagnetic materials and his findings show an attenuation of the power spectrum approaching the near field regime. This coincides with the findings of Schlageter [36] who stated that the main cause of intrinsic noise is the 1/f sensor noise. This type of sensor noise will need to be addressed during the construction of the acquisition system. Work by Stutzke et al [49] has suggested techniques to help limit this sensor noise with good experimental practice.

The second category is extrinsic noise, or noise external to the system. The basis for this type of noise is the low frequency of the Earth’s magnetic field. Experimental research has been performed to measure the natural noise floor and map the magnetic characteristics of the Earth [50]. Data gathered in the United States (Colorado and California) suggest that the dynamic range, 0 to 100 kHz, of the natural noise floor shows the magnetic noise density to be on the order of 10^{-8} G/√Hz which decays by approximately 10 dB per decade [51].

Additionally, using the World Magnetic Model [52] provided by the National Oceanic and Atmospheric Administration (NOAA), information on magnetic fields was provided specifically for Morgantown, WV (39°38'04" N 79°57'22" W at an altitude of 555 m) for December 2011.

The Earth's total field (***F***) is composed of a horizontal (***H***) and vertical (***Z***) intensity, determined by angles of declination (***D***) and inclination (***I***), as shown in Figure 10 [53]. Recorded data from NOAA reports a total field of 31,787 nT (320 mG) and inward field, or z component, of -15,608 nT (-160 mG), with a change/year of 44.1 nT (440 µG) and -80.2 nT (-800 µG), respectively.

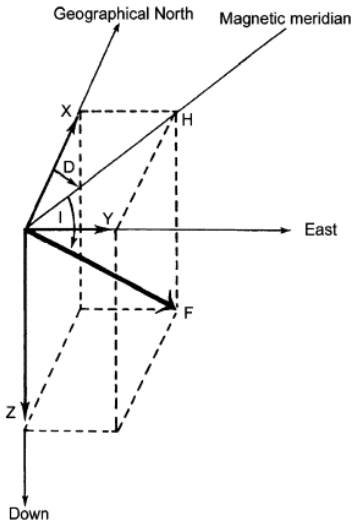

Figure 10 - Vector components of the Earth magnetic field [53]

The change in the inward field between December 1 and December 31, 2011 was 0.13 mG, averaging a rate of change of 0.01 mG/day. This data is sampled and averaged over the day. A high resolution digital fluxgate magnetometer, located in Fredericksburg, VA, continuously recorded data [54] for the United State Geological Survey (USGS) at 1 Hz, and has recorded the range of the inward field which varies 14.44 nT (0.144 mG) during a 60 minute operational window, as seen in Figure 11. This corresponds closely with other reports saying that the broad-scale, solar-quiet magnetic fields have an order of magnitude of 0.2 - 0.3 mG [55], and that the oscillations of these time-varying fields are on the order of 0.01 mG [56].

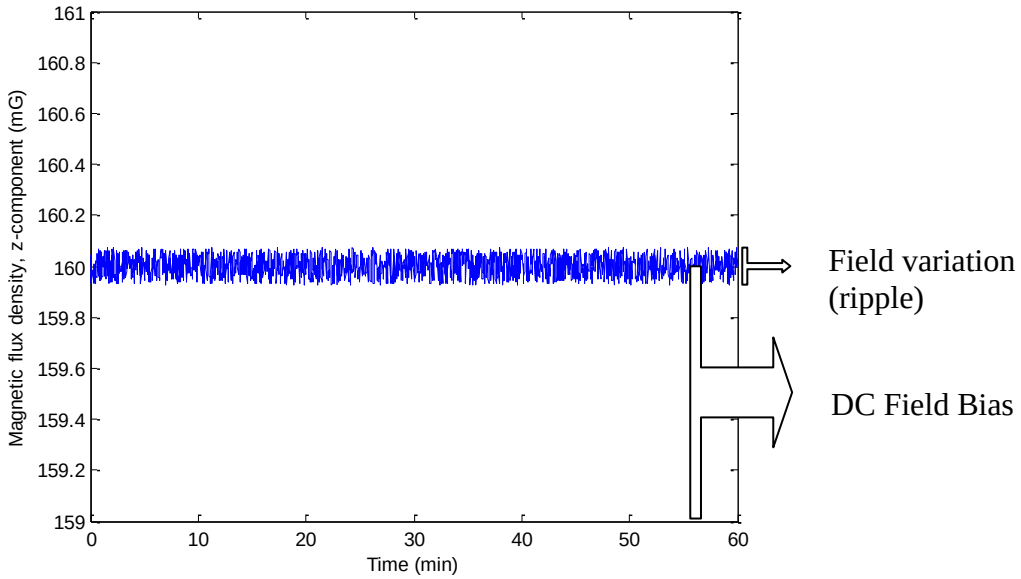

Figure 11 - Plot of recorded magnetic flux density sampled at 1 Hz for a 60 minute duration at Fredericksburg, VA (USGS)

In a later chapter, experimental data collected will show that the magnetic flux density range varies between 4 to 7 mG (ripple) on top of the DC z-component of the Earth's magnetic field, during 30 minutes of operation for the proposed magnetic sensor network in a laboratory setting. As discussed later, this larger variation is due to additional noise in the magnetic sensors, data acquisition hardware, and external noise (overhead lights, power lines, etc.) in the laboratory environment. 4 mG will be the noise variation used for the remainder of the derivations in this document.

2.6 Review of Position Estimation and Error Reduction

Bayesian filtering techniques, including Kalman filters, have been addressed for predicting and estimating position [57], [58]. Bayesian filters use probability models to determine dynamic changes in a system with noise [59]. Fox et al state, “Kalman filters are the most widely used variant of Bayes filters” [59]. The premise behind a Kalman filter is to predict the results based upon two moments—the mean and the covariance matrix.

The advantage of predicting based solely upon the mean and covariance is that it yields greater efficiency during computation. Simon [60] adds, "The Kalman filter not only works well in practice, but it is theoretically attractive because it can be shown that of all possible filters, it is the one that minimizes the variance of the estimation error." Kalman filters use a state transition model and control inputs to help predict future states of a system. A typical Kalman filtering algorithm includes two parts: predict and update equations. The algorithm is shown below [61].

Predict

Determine predicted (a priori) state estimate ($\hat{\boldsymbol{x}}$) and estimate covariance ($\boldsymbol{P}$) at instance *k*.

$$\hat{\boldsymbol{x}}_{\boldsymbol{k|k-1}} = \boldsymbol{A_k}\hat{\boldsymbol{x}}_{\boldsymbol{k-1|k-1}} + \boldsymbol{B_k}\boldsymbol{u_k} + \boldsymbol{w_k}, \quad \textbf{(2.6.1)}$$

$$\boldsymbol{z_{k|k-1}} = \boldsymbol{H_k}\hat{\boldsymbol{x}}_{\boldsymbol{k|k-1}} + \boldsymbol{\nu_k}, \text{ and} \quad \textbf{(2.6.2)}$$

$$\boldsymbol{P_{k|k-1}} = \boldsymbol{A_k}\boldsymbol{P_{k-1|k-1}}\boldsymbol{A_k}^T + \boldsymbol{Q_k}, \quad \textbf{(2.6.3)}$$

given

$$p(\boldsymbol{w_k}) \sim N(0, \boldsymbol{Q_k}), \quad \textbf{(2.6.4)}$$

$$p(\boldsymbol{\nu_k}) \sim N(0, \boldsymbol{R_k}), \text{ and} \quad \textbf{(2.6.5)}$$

where $\boldsymbol{A}$ is the state transition matrix, $\boldsymbol{B}$ is the control input matrix, $\boldsymbol{H}$ is the measurement output matrix , $\boldsymbol{u}$ is the control input vector, $\boldsymbol{w}$ is the process noise, $\boldsymbol{\nu}$ is the measurement noise, and $\boldsymbol{Q}$ is the covariance of process noise, and $\boldsymbol{R}$ is the covariance of the measurement noise..

Update

Calculate (a posteriori) updated innovation or measurement residual ($\hat{\boldsymbol{y}}$)**,** innovation covariance ($\boldsymbol{S}$), optimal Kalman gain (*K*), and updated (a posteriori) state estimate ($\hat{\boldsymbol{x}}$) and estimate covariance ($\boldsymbol{P}$) given true measurement ($\boldsymbol{z}$).

$$\hat{\boldsymbol{y}}_{\boldsymbol{k}} = \boldsymbol{z}_{\boldsymbol{k}} - \boldsymbol{H}_{\boldsymbol{k}}\hat{\boldsymbol{x}}_{\boldsymbol{k|k-1}}, \quad \textbf{(2.6.6)}$$

$$\boldsymbol{S}_{\boldsymbol{k}} = \boldsymbol{H}_{\boldsymbol{k}}\boldsymbol{P}_{\boldsymbol{k|k-1}}\boldsymbol{H}_{\boldsymbol{k}}{}^{T} + \boldsymbol{R}_{\boldsymbol{k}}, \quad \textbf{(2.6.7)}$$

$$\boldsymbol{K}_{\boldsymbol{k}} = \boldsymbol{P}_{\boldsymbol{k|k-1}}\boldsymbol{H}_{\boldsymbol{k}}{}^{T}\boldsymbol{S}_{\boldsymbol{k}}{}^{-1}, \quad \textbf{(2.6.8)}$$

$$\hat{\boldsymbol{x}}_{\boldsymbol{k|k}} = \hat{\boldsymbol{x}}_{\boldsymbol{k|k-1}} + \boldsymbol{K}_{\boldsymbol{k}}\hat{\boldsymbol{y}}_{\boldsymbol{k}}, \text{ and} \quad \textbf{(2.6.9)}$$

$$\boldsymbol{P}_{\boldsymbol{k|k}} = (\boldsymbol{I} - \boldsymbol{K}_{\boldsymbol{k}}\boldsymbol{H}_{\boldsymbol{k}})\boldsymbol{P}_{\boldsymbol{k|k-1}}, \quad \textbf{(2.6.10)}$$

where is the true measurement and $\boldsymbol{R}$ is the covariance of the measurement noise.

Additionally, Maybeck [62] examines Kalman filters in the presence of stochastic models. He introduces a two model system (predictor system) in which an indirect measurement, or guess, is used alongside a measurement where both can carry different weights. Maybeck [62] uses an additive probability density to determine a "good" measurement. A graphical representation of this can be seen in Figure 12. This can be compared to a system that uses a hybrid of actual and predicted information to achieve a final, reported value, which can be more accurate than either separate input.

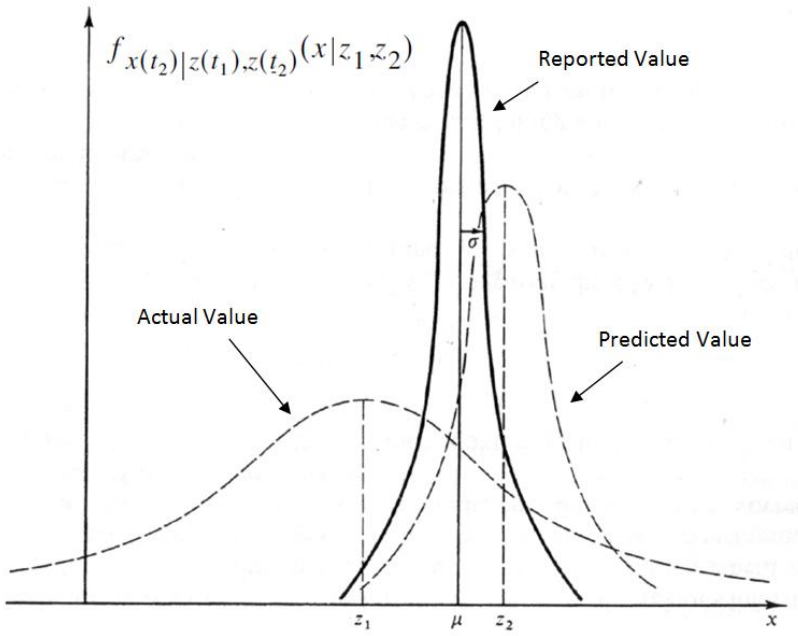

Figure 12 - Graphical representation of additive probability density [62]

Kalman filters have been used as position estimators in such applications as magnetic resonance imaging [63], speech enhancement [64], structural identification [65], ultrasonic ranging [66], global positioning [67], and robotic tracking [68], [69], [70]. Kalman [57] designed his work around the basic tenets behind positioning and tracking systems: prediction of random signals, ability to determine a random signal from random noise, and detection and location of specific signals in the presence of noise. Many, if not all, tracker-estimator and position predicting systems identified take advantage of these principles.

Chan, Hu, and Plant [71] have investigated one such Kalman filtering scheme. These researchers have derived their Kalman filter and detection system from least squares estimators. The authors use the system's state space model as the beginnings of the design process. The system components include a state-space model, control laws, and input noise. To simplify calculations, all filtering is performed using the rectangular coordinate system. This process has been implemented in several cases [66], [67], [68] in order to avoid more complex computations in two-dimensional cases.

Chan et al. [71] study the effects of the number of measurements taken versus the theoretical and experimental variance. As expected, the larger number of samples yields a smaller variance. The authors discuss their rather simple implementation of the least squares estimator, detecting systems, and Kalman filter. They discuss a mechanism used to hone the estimator; comparing the actual value, estimated value, and a set threshold value. To obtain better results, the estimator value changes based upon the deviation to theoretical. "The idea is to have a [threshold] high enough to reduce the false alarm rate and allow the filter to settle" [71]. This method could be easily adapted for other tracking schemes, like the one proposed by this current work.

A Kalman filter design has also been implemented for passive tracking. Weiss and Moore [72] introduce such a system that is based on the Extended Kalman Filter (EKF). They state, "Extended Kalman Filters are attractive for such applications but their performance can be significantly improved with additional processing" [72]. "The Extended Kalman Filter algorithm is an optimal recursive algorithm for nonlinear systems." [73] Dhaouadi et al. [73] summarize factors for the Extended Kalman Filter: knowledge of the system and its dynamics, description of

the system noise (including measurement error), and information about initial conditions. Given the following system equations (2.6.11) - (2.6.13) [74], the block diagram for the typical Kalman filter can be seen in Figure 13.

$$\boldsymbol{K_k = P_{k|k-1} H_k^T \left[H_k P_{k|k-1} H_k^T + R_k \right]^{-1}}, \tag{2.6.11}$$

$$\boldsymbol{\hat{x}_{k|k} = \hat{x}_{k|k-1} + K_k \left[z_k - H_k \hat{x}_{k|k-1} \right]}, \text{ and} \tag{2.6.12}$$

$$\boldsymbol{P_{k|k} = (I - K_k H_k) P_{k|k-1}} \tag{2.6.13}$$

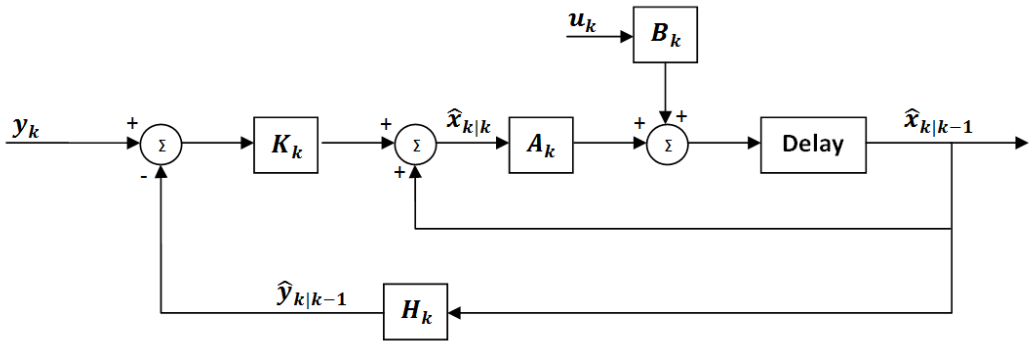

Figure 13 - Block diagram of Kalman Filter [74]

Both the Kalman and Extended Kalman Filters can be used as an observer (i.e. tracking problem) for a system that may or may not have the ability for user input. The Kalman filter can be used "on-line" (real time) or "off-line" (post processing). Although Kalman filters are typically used for position estimation, other methods such as particle filters [75] have also been shown to have equal performance. Either of these algorithms / filters would also be applicable to this topic of magnetic tracking. The integration of a Kalman filter for this system will be discussed in detail a later section of this document.

Chapter 3 – Research Approach and Methodology

Chapter 2 has provided background information pertinent to the magnetic location problem, including current location and tracking methods and algorithms, previous embodiments of systems already developed, and the theory behind both. This chapter will use guidance from other systems, as well as the provided theory in order to develop an approach to solving the proposed problem.

This chapter will discuss developing a model for a permanent magnetic source, permanent magnetic source specifications, including magnetic flux density, verification of the source with finite element modeling, description of the magnetic sensor network and its specifications, as well as an apparatus for experimental testing, and an algorithm for determining position and orientation, including position estimation and error reduction. Finally, specifications for a data acquisition system that will be needed to collect information, and the hardware needed to process the information will be addressed.

3.1 Developing a Model for a Permanent Magnetic Source

Before characterizing the magnetic source and specifications for this system, we must first examine how to model the source, and the geometry of the established magnetic field distribution. The magnetic source that is examined in this chapter will be a permanent magnet. Because magnetic fields of sources far from the point of measurement resemble that of a magnetic dipole, the dipole equation will serve as a starting point for developing a magnetic model. This magnetic dipole equation was introduced as (2.3.11) and is duplicated here.

$$\boldsymbol{B}(\boldsymbol{m},\boldsymbol{r}) = \frac{\boldsymbol{B_r}}{2} \cdot \left[\frac{3\hat{\boldsymbol{r}}(\hat{\boldsymbol{r}} \cdot \boldsymbol{m}) - \boldsymbol{m}}{|\boldsymbol{r}|^3}\right] + \boldsymbol{B}_{EARTH}, \tag{3.1.1}$$

where $\boldsymbol{B}$ is the magnetic flux density, $\boldsymbol{B_r}$ is the surface remanent magnetization, $\boldsymbol{B_{EARTH}}$ is the magnetic flux density of the Earth, $\boldsymbol{r}$ is the vector distance between source and measurement, $\hat{\boldsymbol{r}}$ is a unit vector along $\boldsymbol{r}$, μ_0 is the free space permeability, and $\boldsymbol{m}$ is the magnetic dipole moment.

Using the fact that **m** and **r** are vectors composed of three-dimensional components, (3.1.2) and (3.1.3), (3.1.1) can be expanded to include three dimensions of a position vector and three dimensions of dipole moment vector, as seen in (3.1.4).

$$\boldsymbol{r} = (\mathrm{x}, \mathrm{y}, \mathrm{z}), \tag{3.1.2}$$

$$\boldsymbol{m} = (\mathrm{m_x}, \mathrm{m_y}, \mathrm{m_z}), \tag{3.1.3}$$

$$\boldsymbol{B}(x, y, z, m_x, m_y, m_z) = \frac{\boldsymbol{B_r}}{2} \cdot \left[\frac{3(\mathrm{x}, \mathrm{y}, \mathrm{z})\left[(\mathrm{x}, \mathrm{y}, \mathrm{z}) \cdot (\mathrm{m_x}, \mathrm{m_y}, \mathrm{m_z})\right]}{\left(\sqrt{x^2 + y^2 + z^2}\right)^5} - \frac{(\mathrm{m_x}, \mathrm{m_y}, \mathrm{m_z})}{\left(\sqrt{x^2 + y^2 + z^2}\right)^3} \right] + \boldsymbol{B}_{EARTH,} \tag{3.1.4}$$

where $\boldsymbol{B}$ is the magnetic flux density, $\boldsymbol{B_r}$ is the surface remanent magnetization, (x, y, z) are vector components of $\boldsymbol{B}$, x, y, and z are components of the position vector in three-dimensional space, μ_0 is the free space permeability, and (m_x, m_y, m_z) are vector components of $\boldsymbol{m}$.

(3.1.4) contains information for all vector components of $\boldsymbol{B}$: B_x , B_y, and B_z. Because this system will be using a single-axis sensor network, the only relevant information will be contained in B_z and thus (3.1.4) can be reduced, accordingly.

$$B_z(x, y, z, m_x, m_y, m_z) = \frac{B_{r_z}}{2} \left[\frac{3z(\mathrm{xm_x} + \mathrm{ym_y} + \mathrm{zm_z})}{\left(\sqrt{x^2 + y^2 + z^2}\right)^5} - \frac{\mathrm{m_z}}{\left(\sqrt{x^2 + y^2 + z^2}\right)^3} \right] + B_{z_{EARTH}}, \tag{3.1.5}$$

where B_z is the z-axis component of $\boldsymbol{B}$, $\boldsymbol{B_{zEARTH}}$ is the z-component of the magnetic flux density of the Earth and B_{r_z} is the surface remanent magnetization in the z-direction.

The proposed system uses a model of a magnetic dipole, which is symmetric about the z-axis. Using this information and spherical conversions in (3.1.6), B_z can be rewritten as a function of three degrees of position and two degrees of orientation (θ, elevation above the x-y plane and φ,

rotation about the z-axis starting from -*x* and going clockwise). A definition of this coordinate system can be seen in Figure 14.

$$\begin{aligned} m_x &= \rho \sin(\theta)\cos(\varphi), \\ m_y &= \rho \sin(\theta)\sin(\varphi), \\ m_z &= \rho \cos(\theta), \text{ and} \end{aligned} \qquad \textbf{(3.1.6)}$$

$$\rho = \sqrt{m_x{}^2 + m_y{}^2 + m_z{}^2} = 1,$$

where m_x, m_y, and m_z are the components of the magnetic dipole moment, θ is elevation above the x-y plane, φ is rotation about the z-axis, and ρ is the spherical radius set to unity (for symmetrical geometries).

$$B_z(x, y, z, \theta, \varphi) = \frac{B_{r_z}}{2}\left[\frac{3z(x\sin(\theta)\cos(\varphi) + y\sin(\theta)\sin(\varphi) + z\cos(\theta))}{\left(\sqrt{x^2 + y^2 + z^2}\right)^5} - \frac{\cos(\theta)}{\left(\sqrt{x^2 + y^2 + z^2}\right)^3}\right] + B_{z_{EARTH}}, \qquad \textbf{(3.1.7)}$$

where B_z is the z-axis component of $\boldsymbol{B}$, B_{r_z} is the surface remanent magnetization in the z-direction, *x*, *y*, and *z* are positions in three-dimensional space of the field point, θ is elevation above the x-y plane, φ is rotation about the z-axis, and μ_0 is the free space permeability.

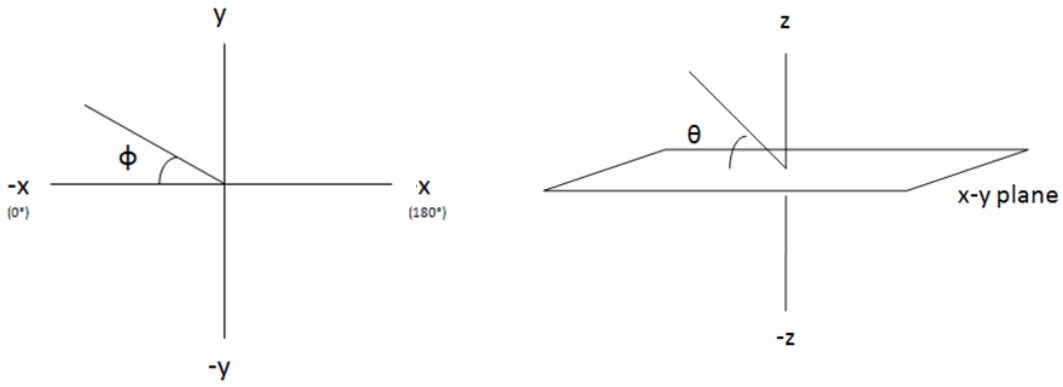

Figure 14 - Definition of model coordinate system

Equation (3.1.7) describes the B_z for an ideal magnetic dipole at (x, y, z) from a magnetic source, located at the origin, that is oriented θ degrees above the x-y plane and φ degrees about the z-axis. This equation is valid for the magnetic source anywhere in three-dimensional space with $0° \leq \theta \leq 90°$ and $0° \leq \theta, \varphi \leq 360°$.

3.2 Permanent Magnetic Source and Specifications

Tracking applications require a source to be tracked. Earlier sections have discussed the benefits of a permanent magnetic source, but have not yet examined physical characteristics. The following sections will examine characteristics such as physical shape, material and B-field characteristics to identify suitable candidates for a permanent magnetic source.

3.2.1 Magnetic Source Geometry

Choosing the physical shape of a permanent magnet is a critical process in the simplification of calculating position and orientation in three-dimensional space. Because the magnetic field distribution is linked closely to the geometry of the magnet, choosing a "geometrically simple" shape, such as a cylinder or disk, will generate a the magnetic field resembles that of a magnetic dipole, relatively close to the magnet.

Using computational electromagnetic software [76], the magnetic flux density calculated and magnetic field lines can be outlined for a disk magnet. Figure 15 shows the standardized magnetic flux density and field lines for a cylindrical 1 kG permanent magnetic dipole disc with a 1 inch diameter and 0.25 inch tall.

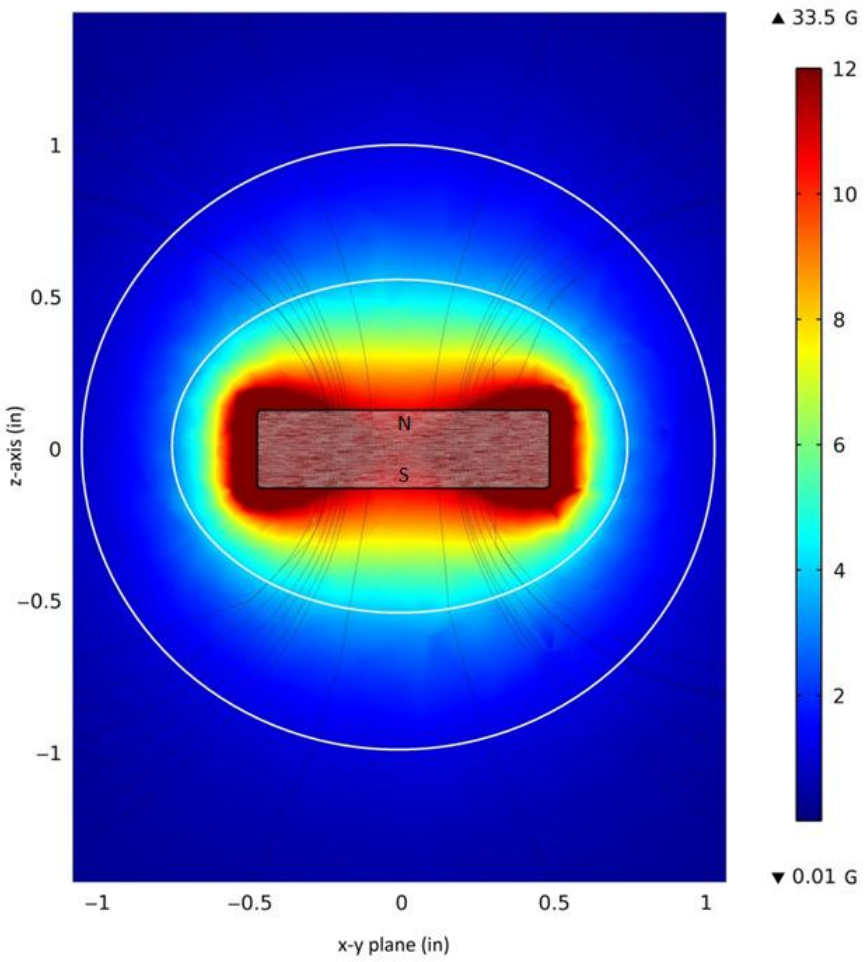

Figure 15 - Simulated magnetic flux density for 1 kG permanent magnetic source centered at the origin on the x-y plane at z = 0 inches.

From Figure 15, the flux density can be seen in two-dimensions with the largest magnetic flux density at the edges of the magnetic and the magnitude of the magnetic flux density approaching a spherical shape as it propagates from the magnet, as predicted [77], [78]. Because of the symmetry present in the permanent magnetic source, this figure can easily be interpreted in three-dimensions (by revolving around the z-axis). At positions very close to the source, magnetic flux density tends to form lobes, similar to the field lines. At positions a couple of times larger than the dimensions of the source, the total magnitude of the magnetic flux density approaches a spherical shape, as shown by the white outlines. The z-component of magnetic flux also approaches a spherical distribution on the x-y plane. Using this information, the three-dimensional position of the sphere can be easily determined.

3.2.2 Magnetic Flux Density of Source

A method of determining the orientation of the magnetic source needs to be addressed. Magnetic flux density, shown in Figure 15, is only one component of the magnetic signature. The magnetic poles of the permanent magnet are connected via field lines. The magnetic field lines or the path of the magnetic field from the North to South poles, of the magnet can be used to help determine orientation. Figure 16 shows the simulated [79] magnetic field lines for a permanent magnetic source.

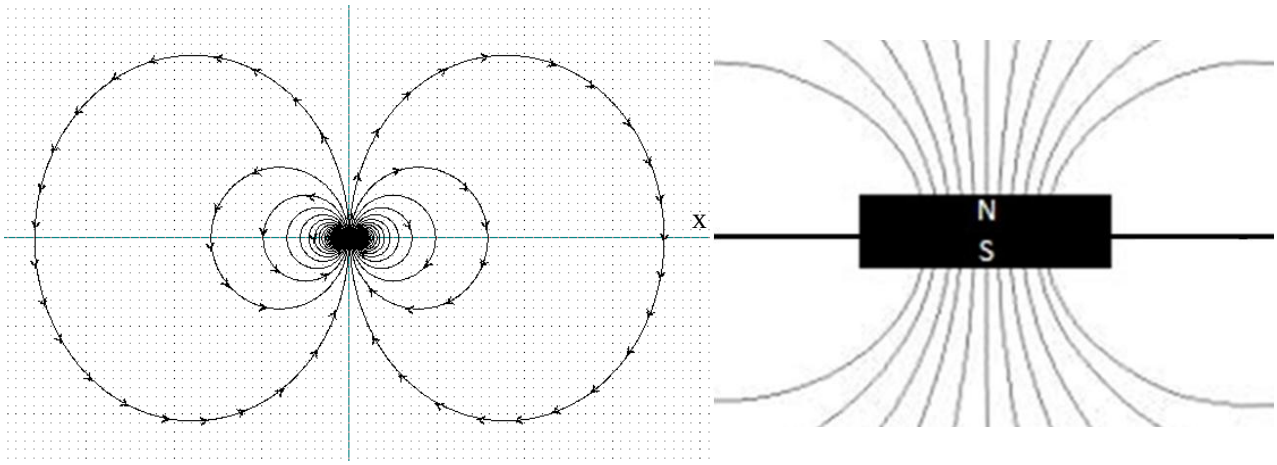

Figure 16 - Simulated magnetic field lines for normalized permanent magnetic source centered at the origin on the x-y plane at z = 0 ft.

Although there are an infinite number of field lines connecting the two poles of the permanent magnet, the directions of the field lines are always consistent—North to South. This fact can be used to aide in determining the orientation of the source.

A computer simulation was performed with a permanent magnet of unit strength with rotation 0°, 90°, 180°, and 270° about the x-axis. By looking at the magnetic flux density for various orientations, uniqueness can begin to be identified. The figures below (Figure 17 - Figure 24) show a simulated plot the magnetic flux density and followed by magnetic field lines, when the source is rotated at 0°, 90°, 180° and 270° about the x-axis, respectively. Plots of magnetic flux density are of a magnetic source (3.308 kG) at a distance of 9.84 ft (or 3 m) from the x-y plane.

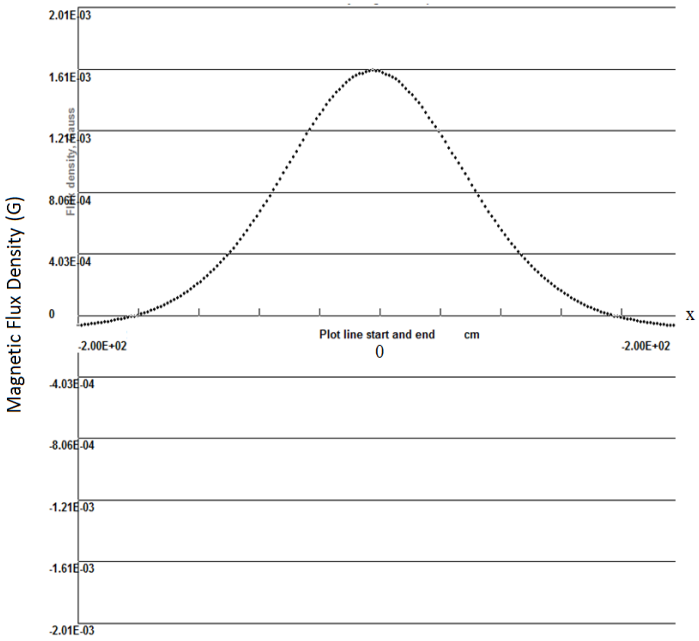

Figure 17 - Simulated magnetic flux density of a 1 kG magnetic source at z = 9.84 ft above origin with orientation of 0° about x-axis.

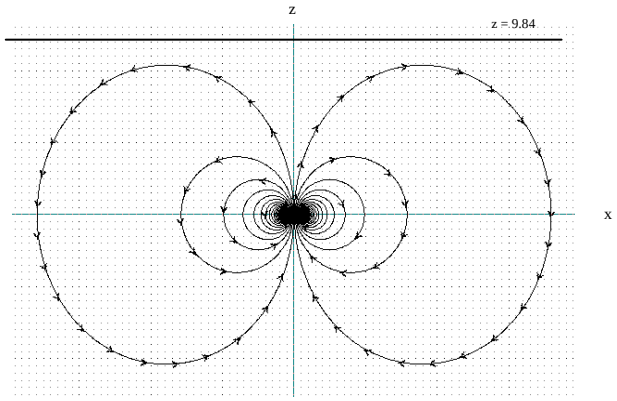

Figure 18 - Simulated magnetic field lines of a 1 kG magnetic source at origin with orientation of 0° about x-axis.

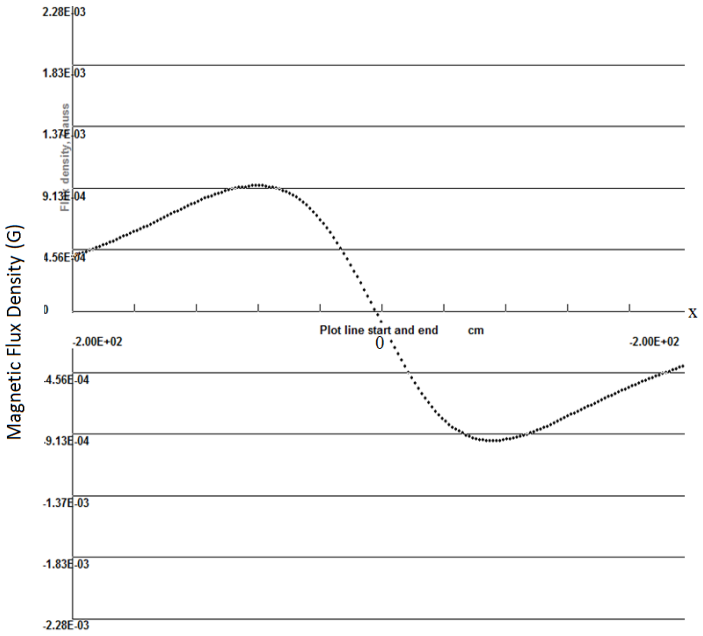

Figure 19 - Simulated magnetic flux density of a 1 kG magnetic source at z = 9.84 ft above origin with orientation of 90° about x-axis.

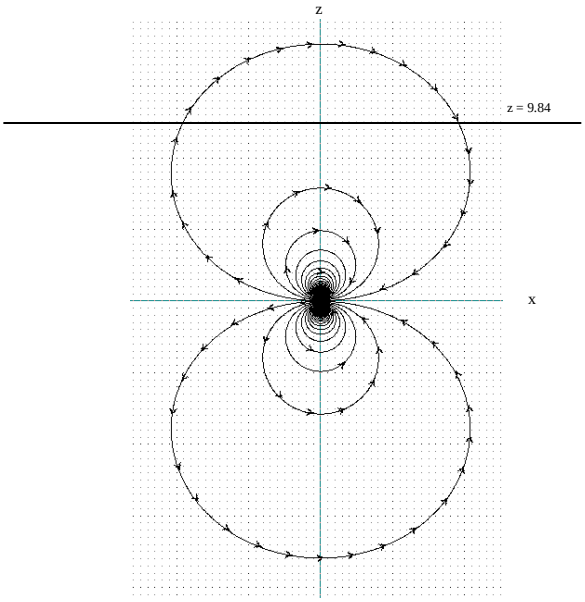

Figure 20 - Simulated magnetic field lines of a 1 kG magnetic source at origin with orientation of 90° about x-axis.

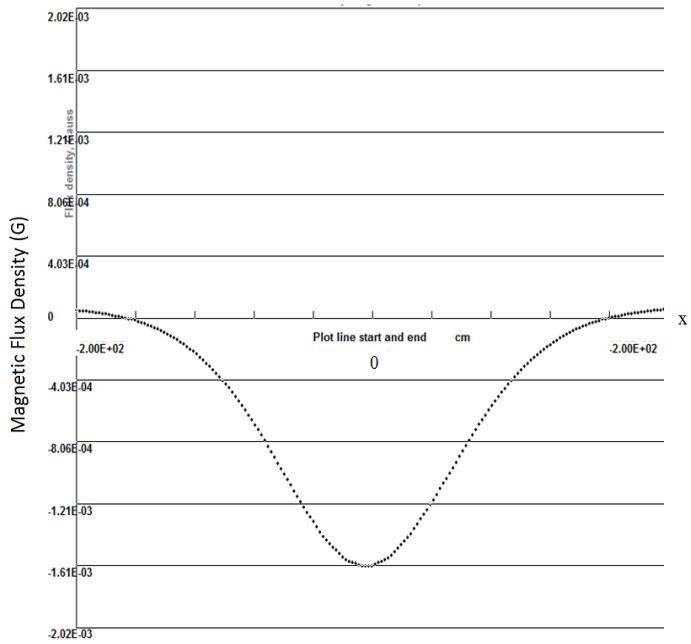

Figure 21 - Simulated magnetic flux density of a 1 kG magnetic source at z = 9.84 ft above origin with orientation of 180° about x-axis.

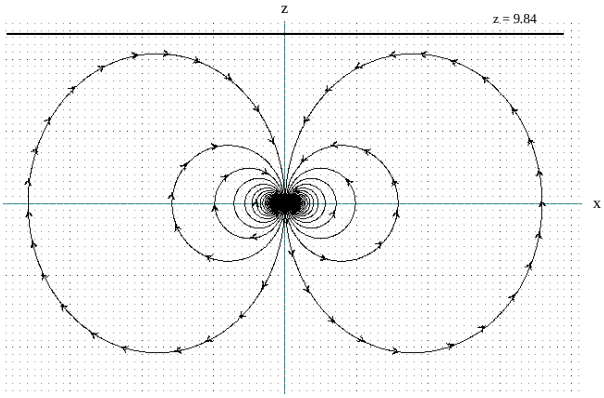

Figure 22 - Simulated magnetic field lines of a 1 kG magnetic source at origin with orientation of 180° about x-axis.

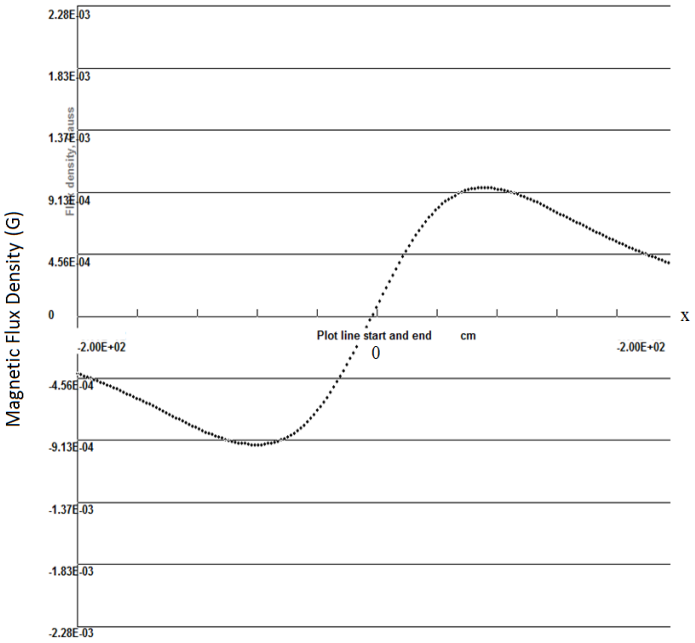

Figure 23 - Simulated magnetic flux density of a 1 kG magnetic source at z = 9.84 ft above origin with orientation of 270° about x-axis.

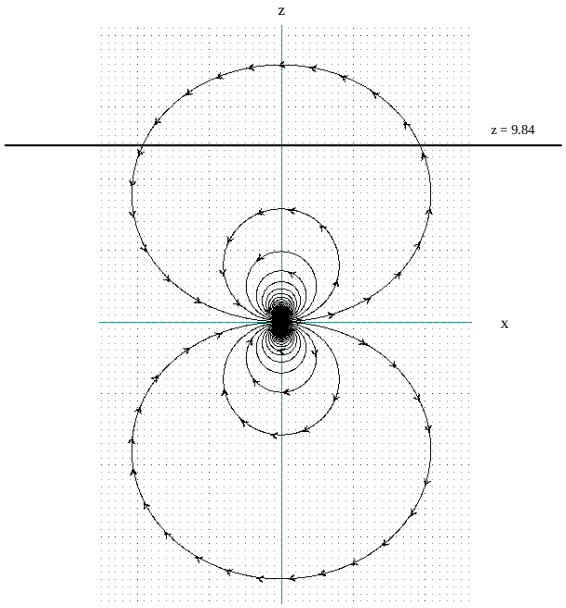

Figure 24 - Simulated magnetic field lines of a 1 kG magnetic source at origin with orientation of 270° about x-axis.

Although the magnitude of the magnetic flux density plots change as the detection plane gets closer to the source, the trends (positive and negative) remain the same. From the uniqueness of these four plots with respect to the sensor plane, it is clear that by tracking the magnetic field magnitudes and directions, the orientation of the source can be discovered. In order to determine orientation with any precision, more than four sets of information will need to be gathered. Since the solution to the general form of the magnetic field equations are complex, it would be very tedious to directly solve for the position and orientation of the source in three-dimensions, analytically. Since a detailed lookup table can be very large and may require its own algorithms, and a numerical (iterative) solution can be computational intensive, using an analytical expression (even if only approximated) would be computationally simpler. Magnetic symmetry, such as the geometry previously discussed in this document, and estimation can also be implemented to aide in quick, accurate computation.

3.3 Verification of Magnetic Model with Finite Element Modeling

Using COMSOL Multiphysics, a finite element computer simulation software package [76] was used to verify the validity of using the dipole model outside of its far-field constraint. For this computational verification, the COMSOL's AC/DC simulator [80] was used with the "magnetic field, no current (mfnc)" modeling package. The simulation contains a magnetic disk, with a 1 inch diameter and 0.25 inch height in a control volume 8 ft in length, width, and height. Table 5 includes information on the electromagnetic characteristics of both the neodymium magnet and the air, in the control volume.

Table 5 - Electromagnetic characteristics for computational simulation constants.

Medium	**Characteristic**	**Value**	**Source**
Air	Conductivity (σ) [S/m]	$5e^{-15}$	[81]
	Relative permittivity (ε_r)	1.00058986	[82]
	Relative permeability (μ_r)	1.0000003	[82]
Neodymium	Conductivity (σ) [S/m]	$1.6e^{6}$	[83]
	Relative permeability (μ_r)	1.05	[84]
	Remanent Magnetization (Br)	3.309 kG	[83]

Using the "magnetic field, no current" modeling package and a dynamic mesh (nodes between 5 and 100 mm), a linear solver was used to determine the simulated magnetic flux density at 12 inches from the magnetic source

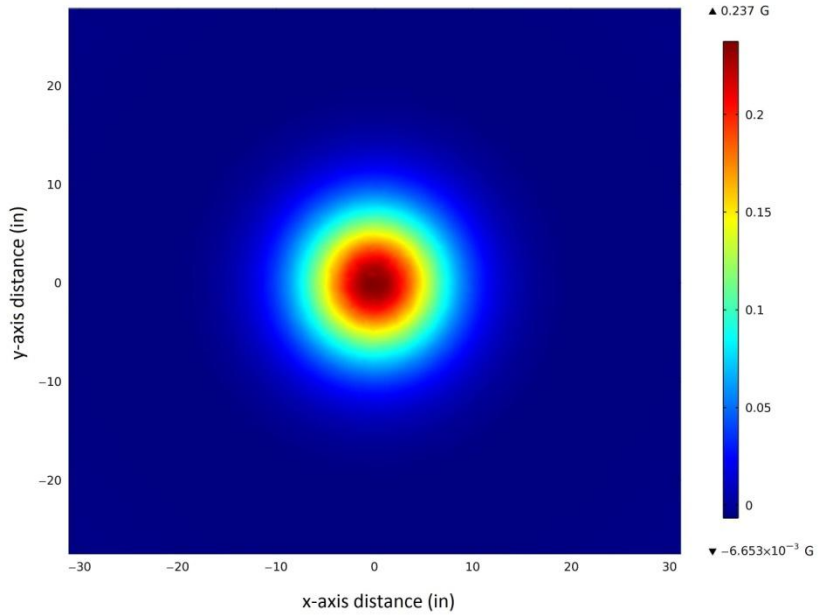

Figure 25 - Plot of simulated two-dimensional magnetic flux density over control volume from a distance of 12 inches away from magnetic source (with θ = 0°)

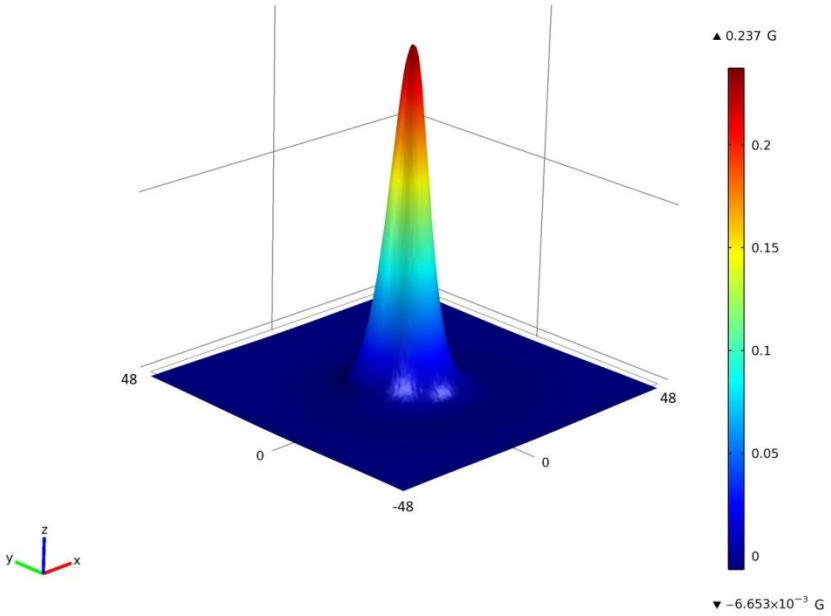

Figure 26 - Plot of simulated, extruded three-dimensional magnetic flux density over control volume from a distance of 12 inches away from magnetic source (with θ = 0°)

Figure 27, show a comparison of the magnetic flux density 12, 24, and 36 inches from the magnetic source.

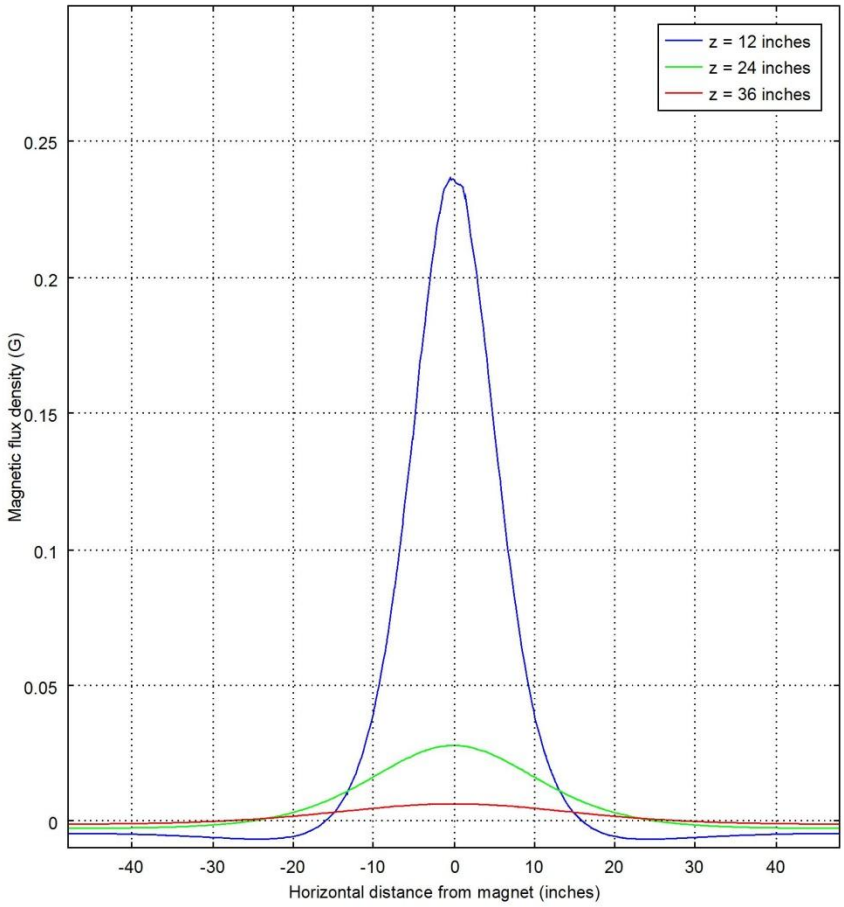

Figure 27 - Plot of simulated magnetic flux density over defined control volume.

A similar process was used to model a magnetic source rotated about the x-axis at angles of 15°, 30°, 45°, 60°, 75°, and 90° and computational results were then compared. Plots comparing analytical and simulated results for one case ($\theta = 0°$) are shown in Figure 28, Figure 29, and Figure 30 for a distance of 12, 24, and 36 inches away from the magnetic source, respectively.

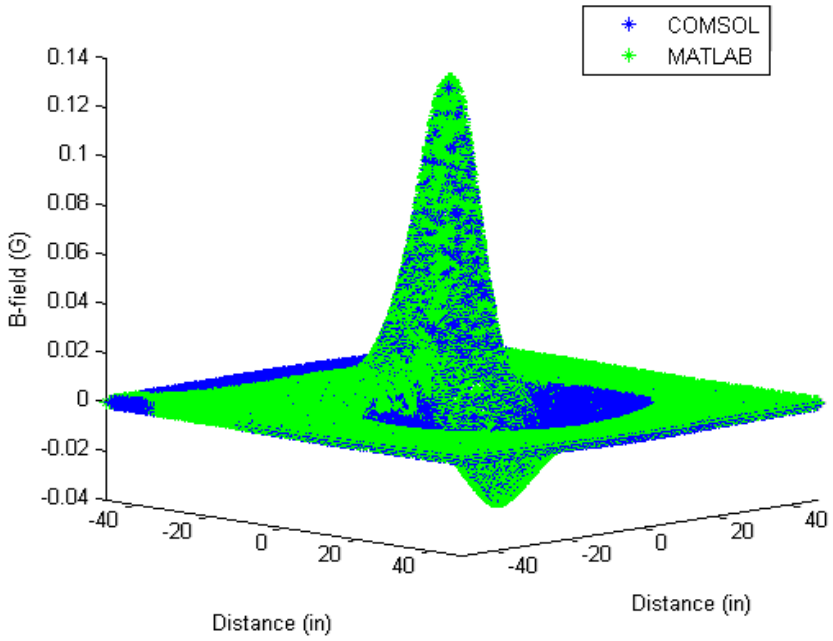

Figure 28 - Analytical model (MATLAB) vs. computational simulation (COMSOL) from a distance of approximately 12 inches away from magnetic source (with θ = 60°)

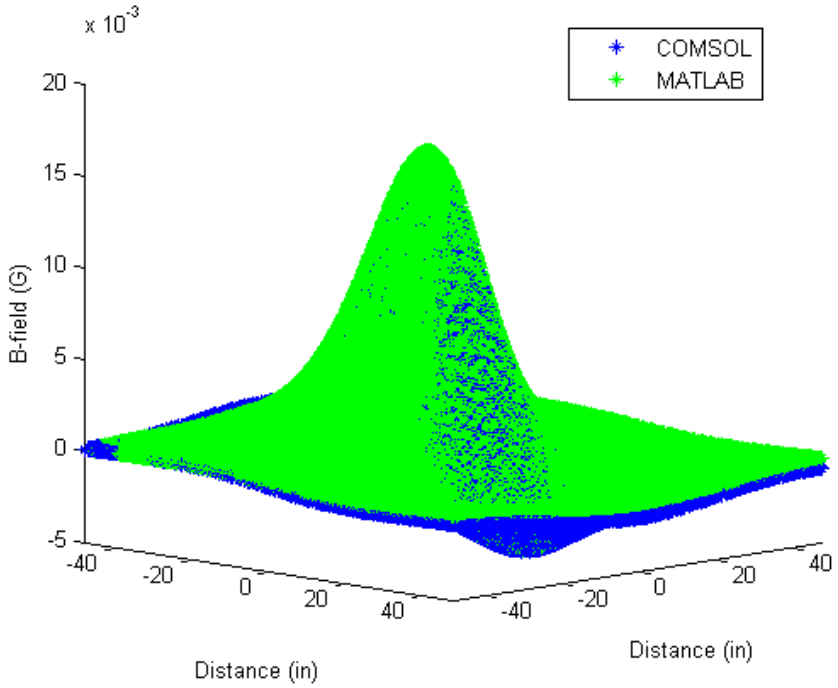

Figure 29 - Analytical model (MATLAB) vs. computational simulation (COMSOL) from a distance of approximately 24 inches away from magnetic source (with θ = 60°)

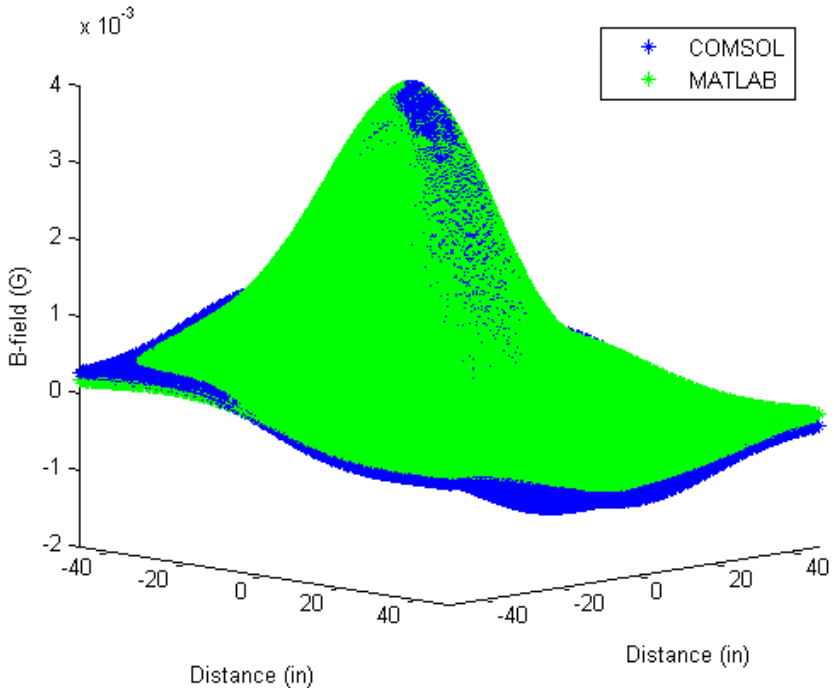

Figure 30 - Analytical model (MATLAB) vs. computational simulation (COMSOL) from a distance of approximately 36 inches away from magnetic source (with θ = 60°)

At a distance of 12, 24, and 36 inches, the mean percent error of the dipole model compared to the magnetic source is 10.77%, 7.66%, and 2.37%, respectively, collected from the data presented in Figure 28, Figure 29, and Figure 30. This is exactly what one would expect; as you move away from the magnetic source, it looks closer to a magnetic dipole. Additionally, the root mean squared error is also projected to be 3.87mG, 0.68 mG and 0.49 mG for approximately 36, 24, and 12 inches, respectively. These values can be used to aid in determining the sensitivity of the sensor needed to detect the magnetic field at these distances. These simulated values will also be validated and supported with experimental data, shown in the next chapter.

3.4 Magnetic Sensor Network and Specifications

The magnetic sensor network conceived for this research is composed solely of one dimensional magnetometers oriented in the z-axis. These sensors measure the magnetic flux density passing through the sensor, and cannot distinguish between magnetic flux from the magnetic source, Earth's field, or ambient magnetic noise. It was suggested in (3.1.1) that these magnetic flux

components are additive. Electromagnetic waves, specifically magnetic fields in free-space, obey the superposition principle, [85], [86]:

$$\boldsymbol{B_{net} = B_{Earth} + B_{Magnet} + B_{Noise},} \quad \textbf{(3.4.1)}$$

where $\boldsymbol{B_{net}}$ is the net magnetic flux density composed of: $\boldsymbol{B_{Earth}}$, the contribution of the Earth's magnetic flux density, $\boldsymbol{B_{Magnet}}$, the contribution of the magnet's magnetic flux density, and $\boldsymbol{B_{Noise}}$, the contribution of magnetic flux density noise, both intrinsic and extrinsic.

Using a 3.309 kG permanent magnet 12 inches away from the sensor, uniformly distributed magnetic noise of 4 mG, and a DC Earth field component of 160 mG, Figure 31 and Figure 32 show the superposition of all magnetic flux densities as seen in (3.4.1).

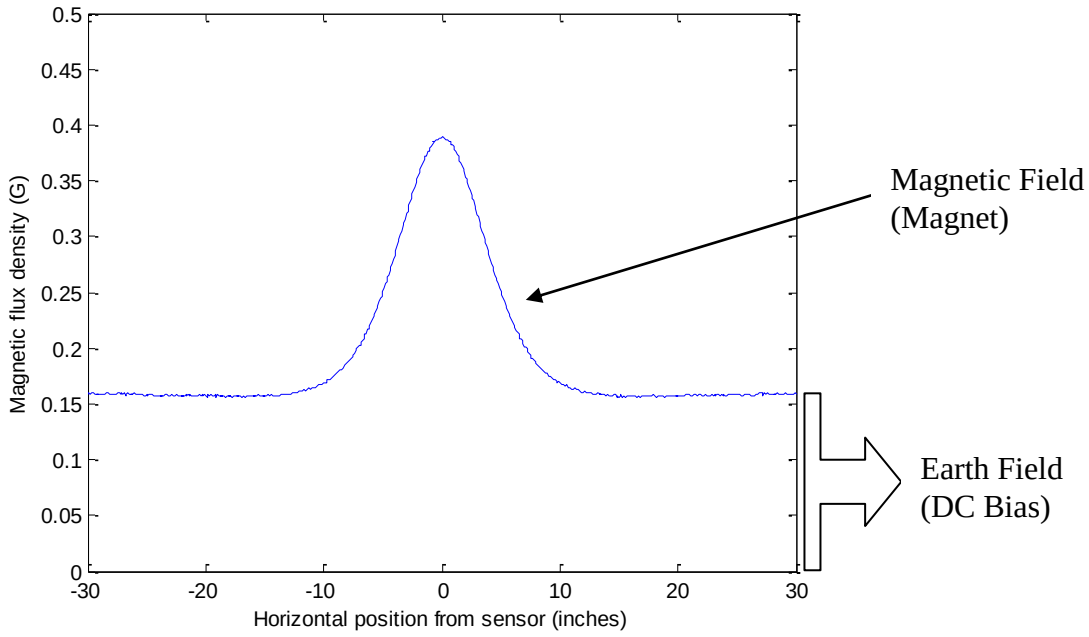

Figure 31 - Plot of the superposition of the magnetic flux densities of a permanent magnet, DC Earth field component, and magnetic noise

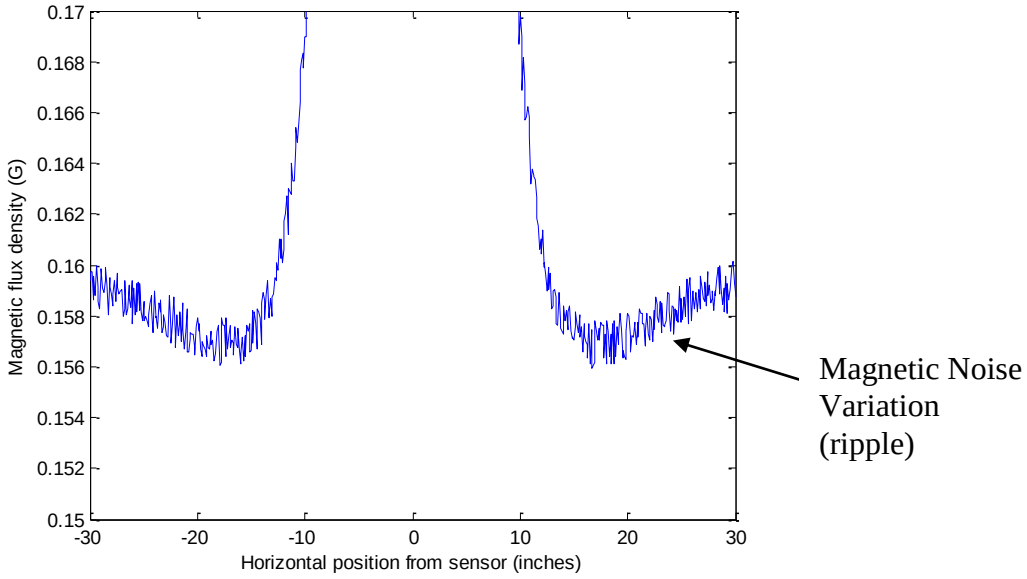

Figure 32 - Scaled plot of the superposition of the magnetic flux densities to show magnetic noise variations

For remainder of the derivations in this dissertation, it is assumed that the Earth's DC field can be measured before the introduction of the magnetic source, as shown in Figure 31, and for the duration of the testing will remain relatively constant, as shown in Figure 11, and thus can be removed as shown in (3.4.1). The remainder of the net B-field will include magnetic flux density components of the magnetic source and magnetic noise.

For the development of the layout and design of the sensor network, characteristics of a Neodymium disc magnetic was used because of its larger remanent magnetism. The following information was used in developing a permanent magnetic sensor network.

Table 6 - Table of magnet characteristics and sensor characteristics used for modeling measureable magnetic field distance (N52 NdFeB) [87],[88]

Magnet Characteristic	Value	Unit
B_r (Internal)	13.2	kG
B_r (Surface)	3.309	kG
Thickness	0.25	inch
Diameter	1	inch
Field Characteristic		
Magnetic noise variation (ripple)	4	mG

Given this information, a plot of the maximum detectable distance for the magnetic sensor can be created (with the DC Earth field component removed). The sensitivity of the magnetic sensor used, as seen in Table 6, is 4 mG, which is the minimum detectable magnetic field for this specific sensor as recorded earlier. This information can then be used, in conjunction with (3.1.7) to determine the maximum detectable distance of the magnet, as seen in Figure 33.

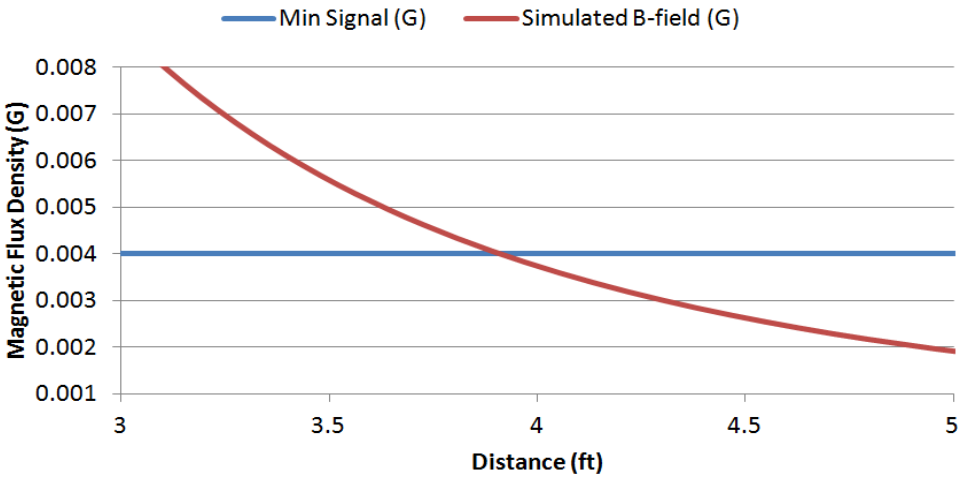

Figure 33 - Scaled plot of magnetic flux density versus distance for a permanent magnetic with surface remanent magnetization Br = 3.309 kG and a noise floor of 4 mG

Using this sensor, with the given magnetic characteristics, there is a maximum detectable distance of approximately 3.9 ft. Obviously, this is the maximum detectable distance (worst case) based on data recorded in the laboratory. Since that scheme is not implemented in this research, a safe testing distance would be under 3 ft away from the sensor network.

3.5 Design of Test Apparatus and Sensor Network

Previous sections have discussed potential magnetic sources and magnetic flux sensors. For this experiment a 13.2 kG neodymium magnet (surface remanent = 3.309 kG) will be used as a source and single, z-axis magnetic sensors as receivers. In order to apply a location algorithm, as previously discussed, at least three sensors will need to be relatively close together (~6 in). The proximity of the sensors needs to be close enough to measure only a small change in the B-field

due to the magnetic source, and not span the entirety of the field. In order to accomplish this, sensor clusters will be constructed and will include three single-axis magnetic sensors. Additionally, this triad arrangement increases the sensor network coverage over that of a single three-axis magnetic sensor. These sensors, placed at a known spacing and orientation, are shown in Figure 34.

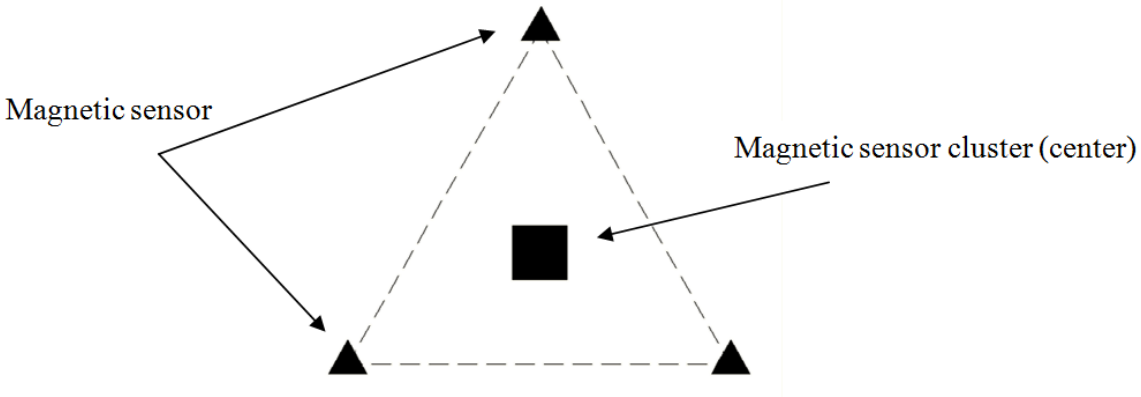

Figure 34 - Sample sensor cluster layout

Each magnetic sensor (▲) is able to contribute one measurement value at each location. The center of the cluster (■) then possesses the mean measurement value and surface normal direction computed by the individual sensors. Because the system is calculating three-dimensional position, and possibly velocity, at least 2 sensor clusters (6 sensors) need to be located within the minimum detectable distance of the magnetic source. To more easily simplify calculations, uniformly spaced sensor clusters were chosen. The spacing between all clusters will initially be 1 ft from center-to-center of each cluster, and adjusted as necessary.

This sensor network has two purposes. The first is to determine the position of the magnetic source. The second, although not pursued in this document or implemented in this experiment, is to determine the ambient magnetic noise. As previously discussed, passive sensor networks lack the ability to have the sensing element turn on and off, making the detection of ambient noise more complicated. To account for this measurement, this system will take advantage of the fact that the projectile is moving, and assumes that the projectile constantly moves around the

detection field. That being the case, this sensor network will have two zones, the projectile zone and the noise zone. This concept is illustrated in Figure 35, below.

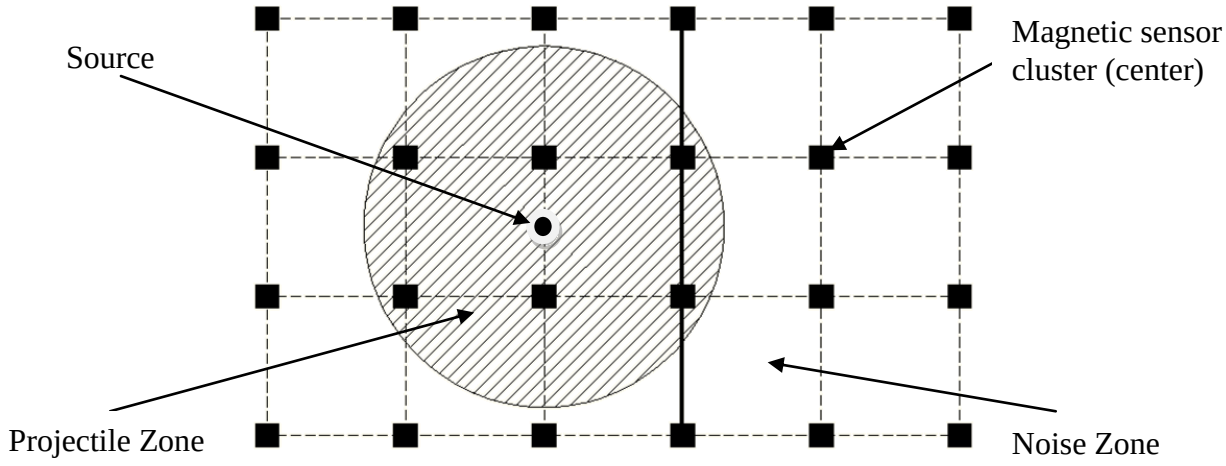

Figure 35 - Zones of sensor network (using centers of clusters)

This illustration assumes that the magnetic source is at an orientation of θ = 0° or 180°. If the source was in any other orientation, the projectile zone would be elliptical. Additionally, the circular/elliptical projectile zone assumes a uniform magnetic noise floor.

In order to accomplish both of these tasks, an adequately sized test apparatus is needed to measure both the position of the source while inside the detection distance and to measure the magnetic noise when outside of the detection distance. The horizontal surface of the experimental apparatus will be outfitted with single axis magnetic sensor clusters discussed in the previous section. The centers of the sensor clusters are to be uniformly spaced to simplify the position calculations to be performed, and will be used to collect information about the magnetic source. This information will be fed into a data acquisition system that will record the information and calculate the three-dimensional position and orientation. Calculations and methodology will be discussed further in the next section.

3.6 Algorithm for Determining 3D Position and Orientation

In this section, methods for determining the three-dimensional position and orientation will be examined. Initially, two dimensional positioning is explored by investigating a projection from three-dimensional space, initially with an ideal magnetic source with θ = 0°. Then orientation, both rotation and elevation, are introduced, and implemented on the original position algorithm. Finally, the z-axis position component is addressed. Tracking and estimation is also applied as a tool to predict the future position.

To test the validity of this research, that a single axis sensor network can locate and track a permanent magnetic source, a simulation is constructed. This simulation uses the theory discussed and statistical analysis to describe the position and orientation of a three-dimensional source. A model depicting magnetic field strength and magnetic field direction are implemented. Since, at a distance greater than the diameter, a disk magnet closely resembles a magnetic dipole, the equation (3.1.7), duplicated here, was used to determine the magnetic flux density (in the z-direction), assuming the magnet is at the origin.

$$B_z(x,y,z,\theta,\varphi) = \frac{B_{r_z}}{2}\left[\frac{3z(x\sin(\theta)\cos(\varphi) + y\sin(\theta)\sin(\varphi) + z\cos(\theta))}{\left(\sqrt{x^2+y^2+z^2}\right)^5} - \frac{\cos(\theta)}{\left(\sqrt{x^2+y^2+z^2}\right)^3}\right] + B_{z_{EARTH}}, \quad \textbf{(3.6.1)}$$

where B_z is the z-axis component of $\boldsymbol{B}$, B_{r_z} is the surface remanent magnetization in the z-direction, *x*, *y*, and *z* are positions in three-dimensional space of the field point, θ is elevation, φ is rotation about the z-axis, and μ_0 is the free space permeability

Using (3.6.1) and an x, y range of -2 ft to 2 ft, at z = 1 ft, a magnetic magnetization of 3.309 kG, and assuming no B-field contribution from the Earth or ambient noise and the magnet is flat (θ = 0°), the following magnetic flux density of an ideal magnetic source can be seen in Figure 36.

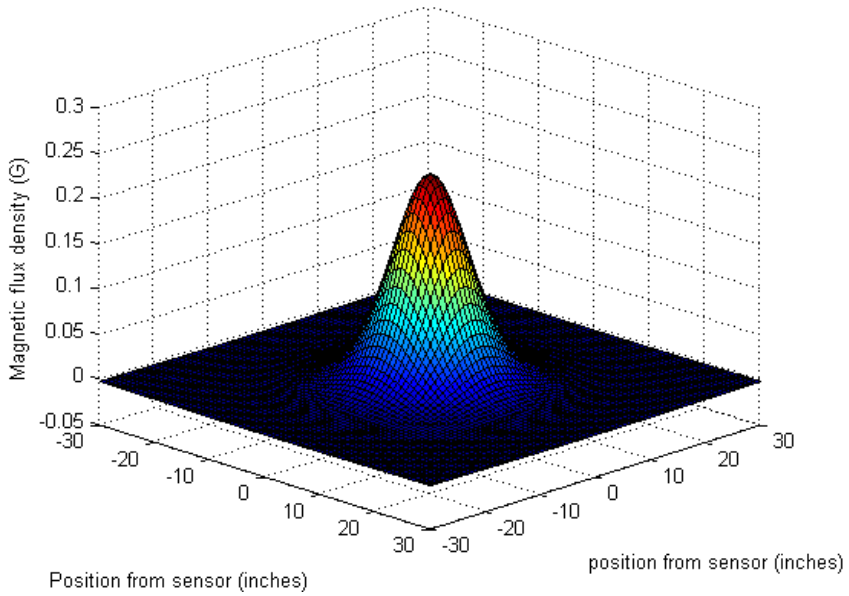

Figure 36 - Magnetic flux density (z-direction) for ideal magnetic dipole located at the center of the sensor network (θ = 0°) 12 inches vertically away from the sensor

In order to implement the algorithm previously discussed, vectors normal to the surface of the magnetic volume must be identified. In this application, the surface normal vector is calculated via a three point "patch" on the surface of the volume. A custom algorithm uses a set of n patches ($n \geq 2$) from the magnetic model. A sample of the output of this code (n = 4, 12 sensors) can be seen in Figure 37 below. Each point (∇) on the plot represents a cluster of magnetic sensors as shown in Figure 34.

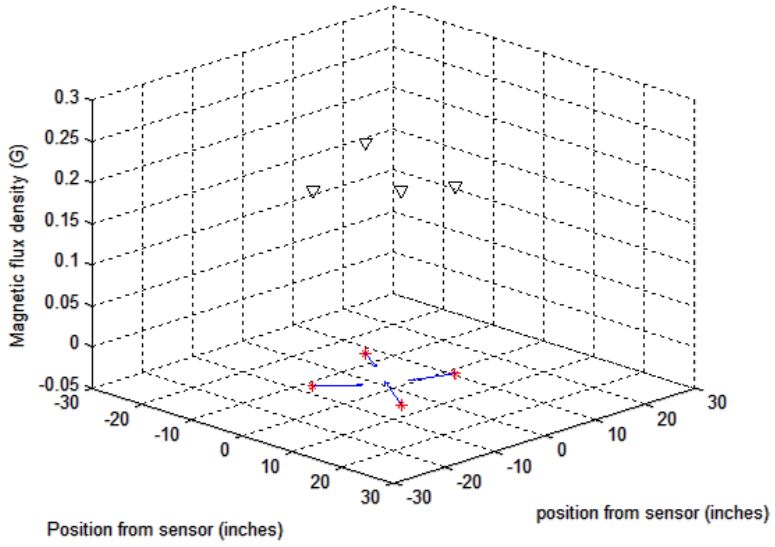

Figure 37 - Patches (n = 4, 12 sensors) selected from magnetic volume

In this sample, four surface patches have been extracted from the ideal magnetic model. Using the average of the points and the cross product formulas below, the center of the patch and the normal vector to the surface through the center of the patch can be determined.

Given a set **Patch** is generated by the subset of the positions of three individual sensors at coordinates $\mathbf{S_1}$, $\mathbf{S_2}$, and $\mathbf{S_3}$:

$$\boldsymbol{Patch} \in \{\boldsymbol{S_1}, \boldsymbol{S_2}, \boldsymbol{S_3}\}$$

$$\begin{aligned} \mathbf{S_1} &= (S_{1x}, S_{1y}, S_{1z}), \\ \mathbf{S_2} &= (S_{2x}, S_{2y}, S_{2z}), \text{ and} \\ \mathbf{S_3} &= (S_{3x}, S_{3y}, S_{3z}), \end{aligned} \tag{3.6.2}$$

where $\boldsymbol{S_1}$, $\boldsymbol{S_2}$, and $\boldsymbol{S_3}$ are the positions of each magnetic sensor in ***Patch***, and S_x, S_y, and S_z are the three-dimensional coordinates of each position.

Patch center and surface normal can be described by:

$$\boldsymbol{Patch_{center}} = \frac{1}{3}(S_{1x} + S_{2x} + S_{3x}, S_{1y} + S_{2y} + S_{3y}, S_{1z} + S_{2z} + S_{3z}), \text{ and} \tag{3.6.3}$$

$$\boldsymbol{Patch_{normal}} = (\boldsymbol{S_1} - \boldsymbol{S_2}) \times (\boldsymbol{S_1} - \boldsymbol{S_3}), \tag{3.6.4}$$

and the same can be defined for the remaining patches.

Using vectors defined by the center of these patches and the surface normal through the centers, a geometric union, or intersect of these vectors is not possible in three-dimensional space. However, if this information is projected on a two-dimensional plane (x-y plane), the intersection of these vectors appears at the position of the magnetic source, as shown in Figure 38.

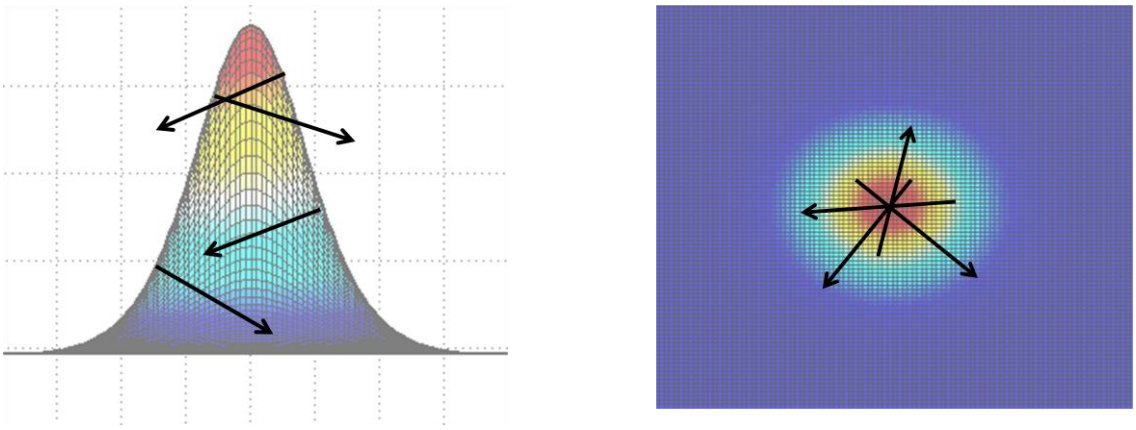

Figure 38 - Simulated plot of the intersection of Patch normal vectors in 3D (left) and 2D (right) space

This two-dimensional intersection is due to the simple, uniform shape of the B-field. $Patch_{center}$ and $Patch_{normal}$ can be described in two-dimensional space as:

$$\boldsymbol{Patch_{center}} = \boldsymbol{P} = \left(\mathrm{P_x}, \mathrm{P_y}\right), \text{ and} \quad \textbf{(3.6.5)}$$

$$\boldsymbol{Patch_{normal}} = \boldsymbol{n} = \left(\mathrm{n_x}, \mathrm{n_y}\right) \quad \textbf{(3.6.6)}$$

Given points $\boldsymbol{P}$ and surface normal directions $\boldsymbol{n}$, the same type of analysis can be performed on the x-y plane to determine the coordinates (x,y) of the magnetic source. Using point P as a starting reference in this plane, a new vector (ray) can be defined in the direction of the two-dimensional projection of the surface normal vector **n**. This can be seen in Figure 39.

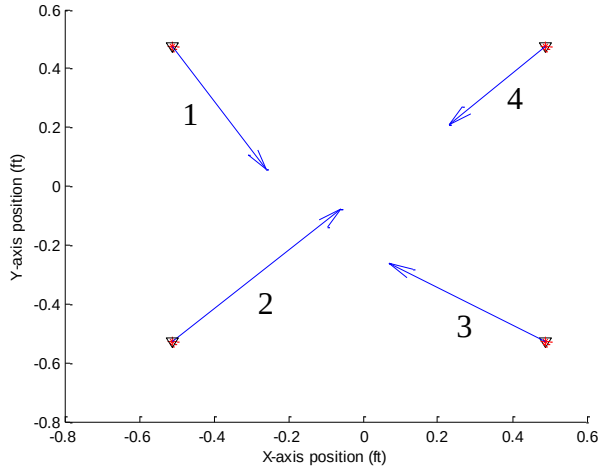

Figure 39 - Intersection of normal vectors in two-dimensional space on the x-y plane

In order to determine the intersection of the vectors, a two line, four point intersection matrix was implemented using Kramer's Rule. The following matrix [89] uses two points on the first vector and two points on the second vector to determine the two dimensional intersect point (x,y):

$$\left(P_{1x}, P_{1y}\right), \left(P_{1x} + n_{1x}, P_{1y} + n_{1y}\right), \text{and} \tag{3.6.7}$$

$$\left(P_{2x}, P_{2y}\right), \left(P_{2x} + n_{2x}, P_{2y} + n_{2y}\right) \tag{3.6.8}$$

which are four points which corresponds to a simultaneous solution of:

$$\begin{vmatrix} x & y & 1 \\ P_{1x} & P_{1y} & 1 \\ P_{1x} + n_{1x} & P_{1y} + n_{1y} & 1 \end{vmatrix} = 0, \text{ and } \begin{vmatrix} x & y & 1 \\ P_{2x} & P_{2y} & 1 \\ P_{2x} + n_{2x} & P_{2y} + n_{2y} & 1 \end{vmatrix} = 0 \tag{3.6.9}$$

In order to obtain the maximum number of intersection points possible, a statistical $\binom{n}{2}$ scheme was used. This allows for the use of 6 intersection points for n = 4 patches. The algorithm was adapted to determine $\binom{n}{2}$ intersection points. The following plot, Figure 40, shows the x-y intersection of the patches.

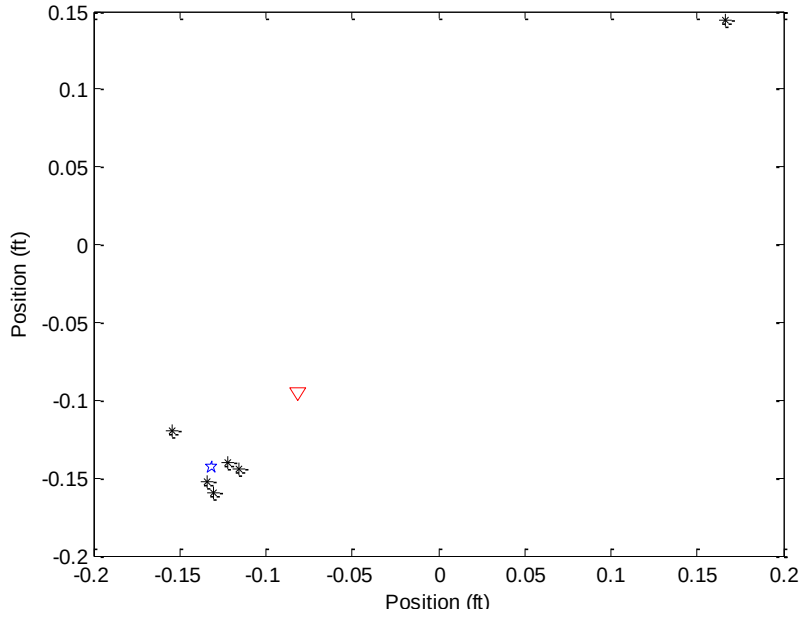

Figure 40 - (x,y) position for all combination of point-normal intersections

The intersection points are denoted as (*) and for n = 4 patches, there are six points. The mean of the intersection points is denoted by (∇). To compensate for the phenomenon of statistical outliers, additional statistical analysis will be implemented to account for these points. The mean will be calculated and any data that is outside one standard deviation of the mean will be disregarded. The intersection with outliers removed is denoted by (✯). This statistical analysis will only be able to be implemented if there are three or more patches (or at least two intersection points). These coordinates along with the *z* off-set (initially zero), a final three-dimensional position can be offered.

The solution presented thus far assumes that the orientation is always aligned on the z-plane ($\theta = 0$). In general, this is not the case and the algorithm must be adapted to account for non-zero orientations. One method to determine elevation is to look at the maximum and minimum sensor values. We have seen that each magnetic orientation produces a unique magnetic field component B_z (Figure 15 - Figure 24), so there should be a function that describe this orientation. Using equation (3.1.7), the ratio of the maximum sensor value to the minimum value across the entire network was obtained for $0° \leq \theta \leq 90°$. The results were fitted empirically to an exponential curve with a goodness-of-fit of 99.84%. The results can be seen in Figure 41 and described by (3.6.10).

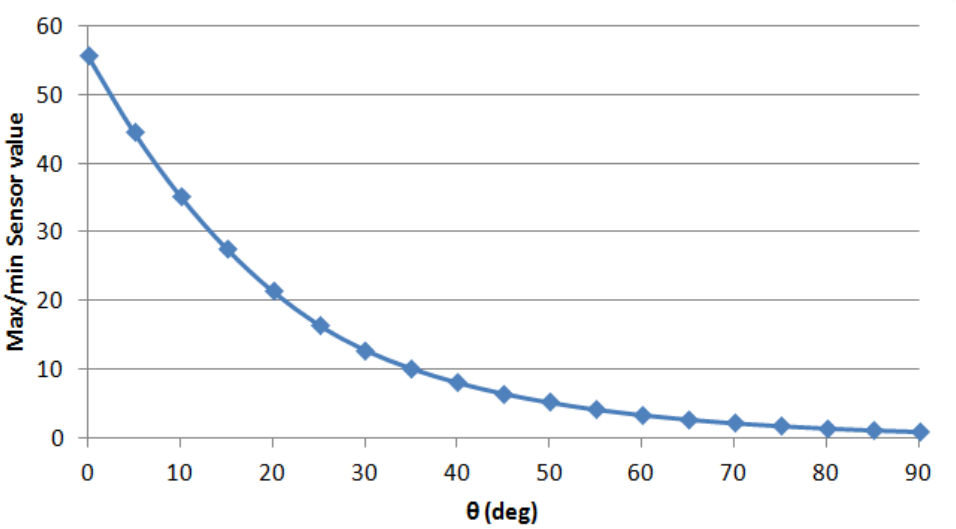

Figure 41 - Plot of elevation angle vs. ratio of simulated sensor values (max/min) for $12 \leq z \leq 48$ in

$$\frac{Sensor_{max}}{Sensor_{min}} = 52.256 * e^{-0.045\theta}, \quad \textbf{(3.6.10)}$$

where $Sensor_{max}$ is the maximum sensor value in the network, $Sensor_{min}$ is the minimum sensor value in the network, an θ is the angle of elevation from the x-y plane.

Given (3.6.10), and two sensor values (maximum and minimum), and expression for the elevation of the magnetic source can be written as:

$$\theta = 87.91 - 22.22 * \ln(Sensor_{max}/Sensor_{min}) \quad \textbf{(3.6.11)}$$

Although a more complex peak finding algorithm could be used, this method was chosen for simplicity, and a direct relation to the sensor outputs.

Likewise, the angle of rotation, φ, can be determined by the location of the maximum sensor value and the minimum sensor value. A dense sensor network was created, Figure 42, with $-2 \leq x, y \leq 2$ ft and a linear sensor spacing of 0.1 inches, where the source is rotating about the origin. Using the maximum and minimum sensor value locations as a reference, angle of rotation, φ, can be determined by the following equation:

$$\varphi = \tan^{-1}\left(\frac{Sensor_{max_x} - Sensor_{min_x}}{Sensor_{max_y} - Sensor_{min_y}}\right), \quad \textbf{(3.6.12)}$$

where $Sensor_{max}$ is the maximum sensor value in the network (with x and y components) and $Sensor_{min}$ is the minimum sensor value in the network (with x and y components).

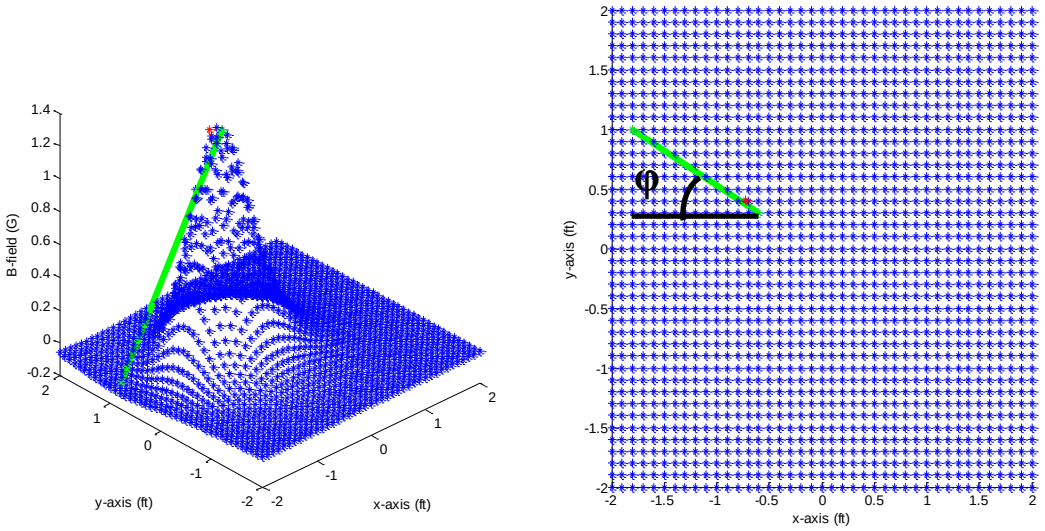

Figure 42 - Plot of simulated rotation angle vs. sensor position

Figure 42 shows the rotation angle, φ, with respect to all sensor positions. φ uses the coordinate systems developed in Section 3.1, and the position of the maximum value sensor as a reference. The resolution of this angle will depend fully on the number and position of sensors in the network. As the number of sensors in the network decrease, resolution for φ will grow.

Once the most likely θ and φ are determined, they can then be used in conjunction with the *x, y* coordinates to determine the z-axis position. Using the same generated sensor network, and the model of an ideal, on-axis dipole, the following plot was created to show the equivalent B_r for a magnet rotated by $0° \leq \theta \leq 90°$. The express for Figure 43 can be seen in (3.6.13). Because of the complexity of the analytical expression for the magnetic B-field, this was simplified using a quadratic model with a goodness-of-fit of 99.57% over the range from $0° \leq \theta \leq 90°$.

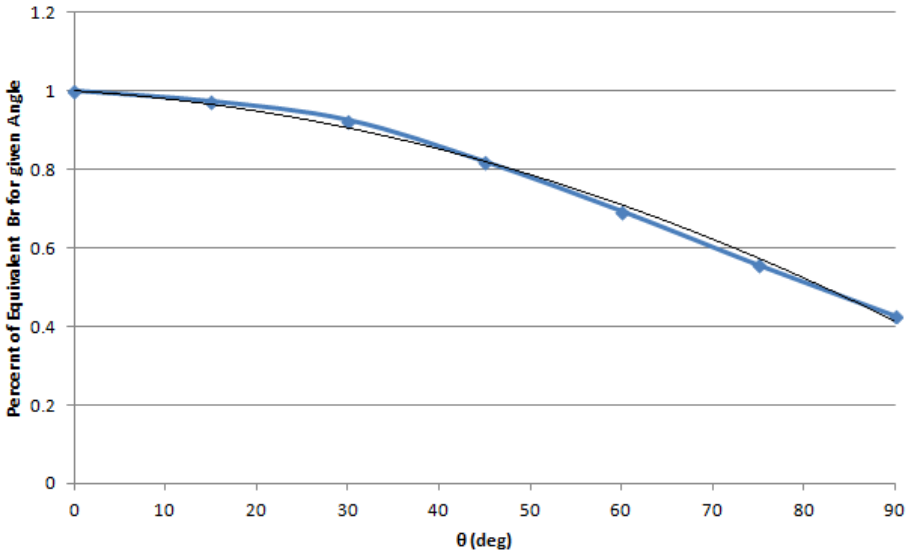

Figure 43 - Plot of θ vs. Equivalent B_r in the z-axis based on maximum sensor value

$$B_{r_z} = -6 * 10^{-5} * \theta^2 - 0.0015 * \theta + 1 \quad \textbf{(3.6.13)}$$

Given the model for an ideal, on axis dipole, the z component of position can be determined based on the elevation, θ, and the maximum sensor value. This simplification can be exploited because of the position of the magnetic sensors. As the sensor network becomes sparser, error will be introduced into this approximation and a more complex model must be used. (3.6.13) can be used in conjunction with (3.6.14), an equation for an on-axis magnetic sensor measurement, to determine the on-axis distance away from the magnetic sensor, as seen in (3.6.15).

$$Sensor_{max} = \frac{B_{r_z}}{z^3}, \quad \textbf{(3.6.14)}$$

$$z = \sqrt[3]{\frac{B_{r_z}}{Sensor_{max}}} = \sqrt[3]{\frac{-6 * 10^{-5} * \theta^2 - 0.0015 * \theta + 1}{Sensor_{max}}}, \quad \textbf{(3.6.15)}$$

where $Sensor_{max}$ is the maximum sensor value in the network, θ is the elevation, and B_{rz} is the maximum on axis B-field generated by rotation the magnet.

The initial method for determining position assumed no elevation of the magnetic source (θ = 0°). Since an elevation and rotation component now exists, the x-y position must be modified. As the magnetic source is rotated the position of the maximum and minimum sensor points begin to collapse in on themselves, and an offset correction must be provided. Note that during operation, the magnetic source can be as close as 12 inches to the sensor network, Figure 44, shows a model for an offset based on the output of the proposed solver algorithm for 12, 24, 36, and 48 inches. The data in this plot was generated by a radius of 10 inches; however, the process would be the same for any rotating magnetic source.

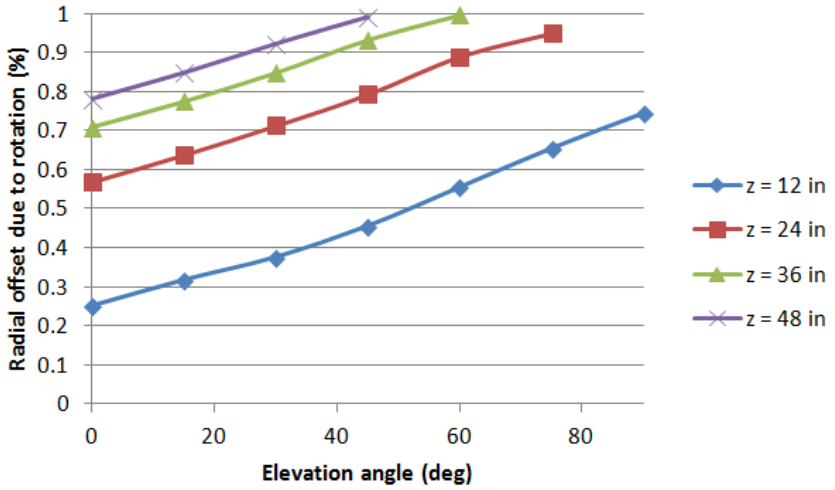

Figure 44 - Radial offset percentage for elevated magnet (z = 12, 24, 36, and 48 inches)

These lines can be collapsed to a single expression (3.6.16) where percent radial offset can be described as a function of both the angle of elevation (θ, linear) and approximate z-axis position (z, quadratic) with a goodness-of-fit of 99.22% for $12 \leq z \leq 48$ inches, $0° \leq \theta \leq 45°$ and additional elevations in Figure 44.

$$Offset_{percent-radial} = 0.0051 * \theta + \left(-0.0652 * \left(\frac{z}{12}\right)^2 + 0.5058 * \frac{z}{12} - 0.2067\right) \quad \textbf{(3.6.16)}$$

And the position (x,y) can be modified from the θ = 0° elevation to the actual orientation of the magnetic source via equations (3.6.17 and (3.6.18).

$$x = x_{\theta=0} + \left(Radius * Offset_{percent-radial}\right)\cos(\theta) \quad \textbf{(3.6.17)}$$

$$y = y_{\theta=0} + \left(Radius * Offset_{percent-radial}\right)\sin(\theta) \quad \textbf{(3.6.18)}$$

By using the methods in this section, we have determined the three dimensional position (x, y, z) and orientation (θ and φ) based sole from the geometry of the B-field and the outputs of an array of single axis (z-axis) magnetic sensors.

3.7 Position Estimation and Error Reduction

It may become necessary to use a position estimation technique to aid in the determination of the source position (to assist in either position calculation or to address constraints in real-time processing), especially as interference from magnetic noise increases. One form of error reduction has been built into this algorithm. The method implemented uses a simple statistical analysis to remove major outliers. The outliers in this simulation will most likely be due to ambient and environmental noise.

Another error reduction method that can easily be implemented into this tracking system is filtering. One such algorithm seen in the previous section, Kalman filtering, uses a kinetic model to aide in position prediction. A three-dimensional, six input (position and velocity) was developed for this novel system to better approximate the object's position, and to show that a basic filter is suitable in this application.

As for developing the filter, the state transition model, control model, and other inputs are based upon the motion equations governing the system. For an object moving in free space with only the effect of gravity, discrete kinematic equations can be described as:

$$\boldsymbol{X_{k+1}} = \boldsymbol{X_k} + \boldsymbol{V_k}\Delta t + \frac{1}{2}\boldsymbol{A_k}\Delta t^2, \text{ and} \quad \textbf{(3.7.1)}$$

$$\boldsymbol{V_{k+1}} = \boldsymbol{V_k} + \boldsymbol{A_k}\Delta t, \quad \textbf{(3.7.2)}$$

where $\boldsymbol{X}$ is position, $\boldsymbol{V}$ is velocity, $\boldsymbol{A}$ is acceleration, and Δt is the time step between each iteration, k.

Vector equations for position, velocity, and acceleration are expanded such that $\boldsymbol{X} = (x_k, y_k, z_k)$, $\boldsymbol{V} = (\dot{x}_k, \dot{y}_k, \dot{z}_k)$, and $\boldsymbol{A} = (\ddot{x}_k, \ddot{y}_k, \ddot{z}_k)$ and the following state-space model can be formed.

$$\begin{bmatrix}\boldsymbol{X_{k+1}}\\ \boldsymbol{V_{k+1}}\end{bmatrix} = \begin{bmatrix} x_{k+1}\\ y_{k+1}\\ z_{k+1}\\ \dot{x}_{k+1}\\ \dot{y}_{k+1}\\ \dot{z}_{k+1}\end{bmatrix} = \begin{bmatrix} 1 & 0 & 0 & \Delta t & 0 & 0\\ 0 & 1 & 0 & 0 & \Delta t & 0\\ 0 & 0 & 1 & 0 & 0 & \Delta t\\ 0 & 0 & 0 & 1 & 0 & 0\\ 0 & 0 & 0 & 0 & 1 & 0\\ 0 & 0 & 0 & 0 & 0 & 1\end{bmatrix}\begin{bmatrix} x_k\\ y_k\\ z_k\\ \dot{x}_k\\ \dot{y}_k\\ \dot{z}_k\end{bmatrix} + \begin{bmatrix} \frac{1}{2}\Delta t^2 & 0 & 0\\ 0 & \frac{1}{2}\Delta t^2 & 0\\ 0 & 0 & \frac{1}{2}\Delta t^2\\ \Delta t & 0 & 0\\ 0 & \Delta t & 0\\ 0 & 0 & \Delta t\end{bmatrix}\begin{bmatrix}\ddot{x}_k\\ \ddot{y}_k\\ \ddot{z}_k\end{bmatrix} \quad \textbf{(3.7.3)}$$

Based on the Kalman filtering algorithm, the following implementation can be used based on Newtonian physics.

$$\boldsymbol{X_{k+1}} = A_k\boldsymbol{X_k} + B_k\ddot{\boldsymbol{X}}_{\boldsymbol{k}} + \boldsymbol{w}_k, \text{ and} \quad \textbf{(3.7.4)}$$

$$\boldsymbol{Z_k} = H_k\boldsymbol{X_k} + \boldsymbol{\nu}_k, \quad \textbf{(3.7.5)}$$

where A_k is the state transition model, B_k is the acceleration input matrix, H_k is the model output matrix, $\boldsymbol{Z}_k$ is the true measurement, $\boldsymbol{w_k}$ is the process noise, and $\boldsymbol{\nu_k}$ is the measurement noise.

Because A_k and B_k are constants based on kinematic models, and will not change during operation, simplifications of $A_k = A$ and $B_k = B$ can be applied. Additionally, calculations will assume equal time steps per iteration, based on the sampling frequency ($\Delta t = 1/f_s$). A simplistic model for the process noise, Q_k, can then be introduced based on the model's acceleration inputs and variance.

$$Q_k = diag\left\{{\sigma_{p_x}}^2, {\sigma_{p_y}}^2, {\sigma_{p_z}}^2, {\sigma_{\dot{p}_x}}^2, {\sigma_{\dot{p}_y}}^2, {\sigma_{\dot{p}_z}}^2\right\}, \quad \textbf{(3.7.6)}$$

where ${\sigma_p}^2$ is the process noise variance of the position and ${\sigma_{\dot{p}}}^2$ is the process noise variance of the velocity, in x, y, z, respectively.

Note, this is the most basic model for process noise. It includes no coupling between components, or even between positions and velocities of the same component. Although a more complex model can and should be created, the output of the system will show that even this very simplistic model will increase the effectiveness of the estimation algorithm. The process noise variance of the position and velocity can be modeled [61] (for a simplistic case) based on the maximum acceleration in the system, where

$${\sigma_x}^2 = {\sigma_y}^2 = {\sigma_z}^2 = \frac{a_{max}(\Delta t)^2}{2} \quad \textbf{(3.7.7)}$$

$${\sigma_{\dot{x}}}^2 = {\sigma_{\dot{y}}}^2 = {\sigma_{\dot{z}}}^2 = a_{max}\Delta t \quad \textbf{(3.7.8)}$$

The output matrix, based both on position and velocity states, can be defined as:

$$H_k = diag\{1,1,1,1,1,1\}, \quad \textbf{(3.7.9)}$$

where the first set of three values are for *x*, *y*, *z* position and the second set are for V_x, V_y, V_z.

The most simplistic covariance of measurement noise, based solely on uncoupled variances of position and velocities (like the process noise) and on the accuracy and repeatability of the sensor used, can be defined as:

$$R_k = diag\left\{{\sigma_{m_x}}^2, {\sigma_{m_y}}^2, {\sigma_{m_z}}^2, {\sigma_{\dot{m}_x}}^2, {\sigma_{\dot{m}_y}}^2, {\sigma_{\dot{m}_z}}^2\right\}, \quad \textbf{(3.7.10)}$$

where ${\sigma_m}^2$ is the measurement noise variance of the position and ${\sigma_{\dot{m}}}^2$ is the measurement noise variance of the velocity, in x, y, z, respectively.

$Q_k = Q$, $R_k = R$, and $H_k = H$ (matrices are constant) can be applied for this simplified case. The Kalman filtering algorithm also requires a set of initial states for the state transition model as well as for the estimate covariance. These values are dependent upon whether the initial states are known (measurements are trusted) or unknown (model is trusted).

Initial states based from unknown position and velocity can assume a position at the origin.

$$\begin{bmatrix} \widehat{\boldsymbol{X}}_{\boldsymbol{k}} \\ \widehat{\dot{\boldsymbol{X}}}_{\boldsymbol{k}} \end{bmatrix} = \begin{bmatrix} \hat{x}_k \\ \hat{y}_k \\ \hat{z}_k \\ \hat{\dot{x}}_k \\ \hat{\dot{y}}_k \\ \hat{\dot{z}}_k \end{bmatrix} \xrightarrow{yields} \begin{bmatrix} 0 \\ 0 \\ 0 \\ v_x \\ v_y \\ v_z \end{bmatrix} \tag{3.7.11}$$

Whereas initial states based from known position and velocity can assume the actual position and velocity:

$$\begin{bmatrix} \widehat{\boldsymbol{X}}_{\boldsymbol{k}} \\ \widehat{\dot{\boldsymbol{X}}}_{\boldsymbol{k}} \end{bmatrix} = \begin{bmatrix} \hat{x}_k \\ \hat{y}_k \\ \hat{z}_k \\ \hat{\dot{x}}_k \\ \hat{\dot{y}}_k \\ \hat{\dot{z}}_k \end{bmatrix} \xrightarrow{yields} \begin{bmatrix} x_0 \\ y_0 \\ z_0 \\ \dot{x}_0 \\ \dot{y}_0 \\ \dot{z}_0 \end{bmatrix} \tag{3.7.12}$$

Initial estimate covariance based on known position and velocity yields:

$$P_{0|0} = \begin{bmatrix} 0 & 0 & 0 & 0 & 0 & 0 \\ 0 & 0 & 0 & 0 & 0 & 0 \\ 0 & 0 & 0 & 0 & 0 & 0 \\ 0 & 0 & 0 & 0 & 0 & 0 \\ 0 & 0 & 0 & 0 & 0 & 0 \\ 0 & 0 & 0 & 0 & 0 & 0 \end{bmatrix} = \mathbf{0} \tag{3.7.13}$$

This estimate covariance matrix assumes that there is a small amount of measurement noise (and/or ambient noise, or other errors) and that the measurement values should be "trusted" more than the estimator "values".

Initial estimate covariance based on unknown position and velocity can be assumed as:

$$P_{0|0} = \begin{bmatrix} L_x & 0 & 0 & 0 & 0 & 0 \\ 0 & L_y & 0 & 0 & 0 & 0 \\ 0 & 0 & L_z & 0 & 0 & 0 \\ 0 & 0 & 0 & L_{\dot{x}} & 0 & 0 \\ 0 & 0 & 0 & 0 & L_{\dot{y}} & 0 \\ 0 & 0 & 0 & 0 & 0 & L_{\dot{z}} \end{bmatrix}, \quad \textbf{(3.7.14)}$$

where $diag\{L_x, L_y, L_z, L_{\dot{x}}, L_{\dot{y}}, L_{\dot{z}}\}$ is suitably larger than the states of $\boldsymbol{X}$ and $\boldsymbol{V}$.

This estimate covariance matrix assumes that there is a larger amount of measurement noise (and/or ambient noise, or other errors) and that the model should be "trusted" more than the measurements. Both matrices will evolve with the estimator over time.

A tracker-observer system can then be developed using this algorithm. One real-world case examined is that of projectile motion. In this case, a projectile is moving in free-space with only the force of gravity acting upon it. In more complicated cases, the motion equations presented here will need to be modified to account for friction or other influential forces (such as aerodynamic drag).

In an example of this model, the projectile travels 0.25 seconds with initial velocity of 120 inches/sec until it is deflected 90° and continues to travel in a new projectile motion for 0.25 seconds with a new initial velocity of 60 inches/sec. Simulation used a process noise based on a_{max} = 100g and a measurements noise $\sigma_m{}^2 = 0.00001$ ft^2, suggested by [90] as an appropriate estimate for the HMC 1021z magnetometer, as a with a sampling frequency of 1 kHz. The results can be seen in Figure 45 and Figure 46.

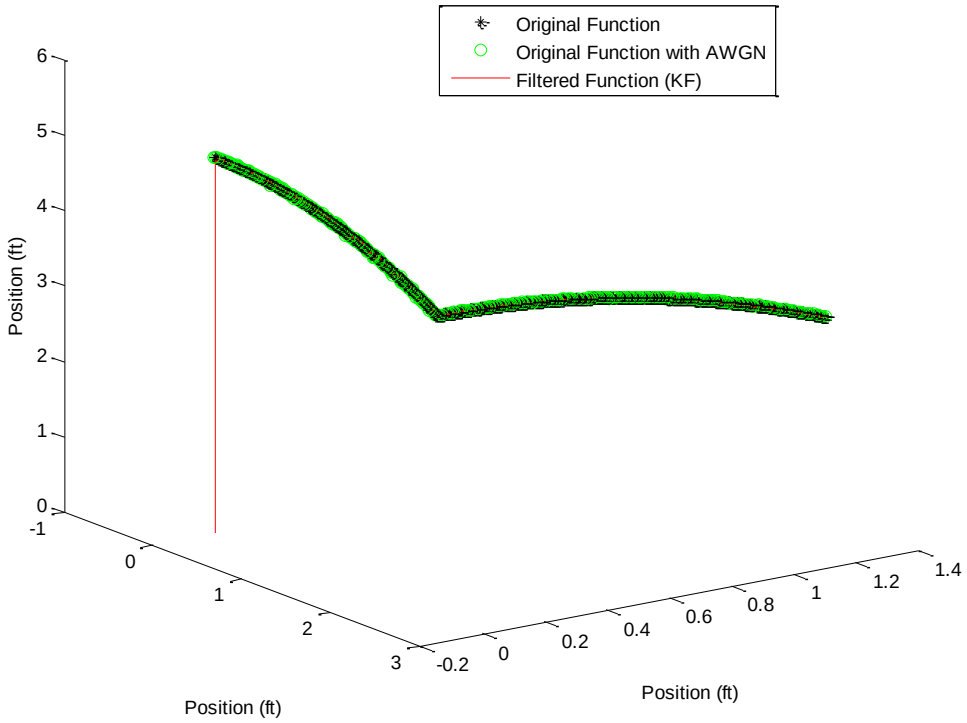

Figure 45 - Path of projectile with and without AWGN and with applied Kalman filter

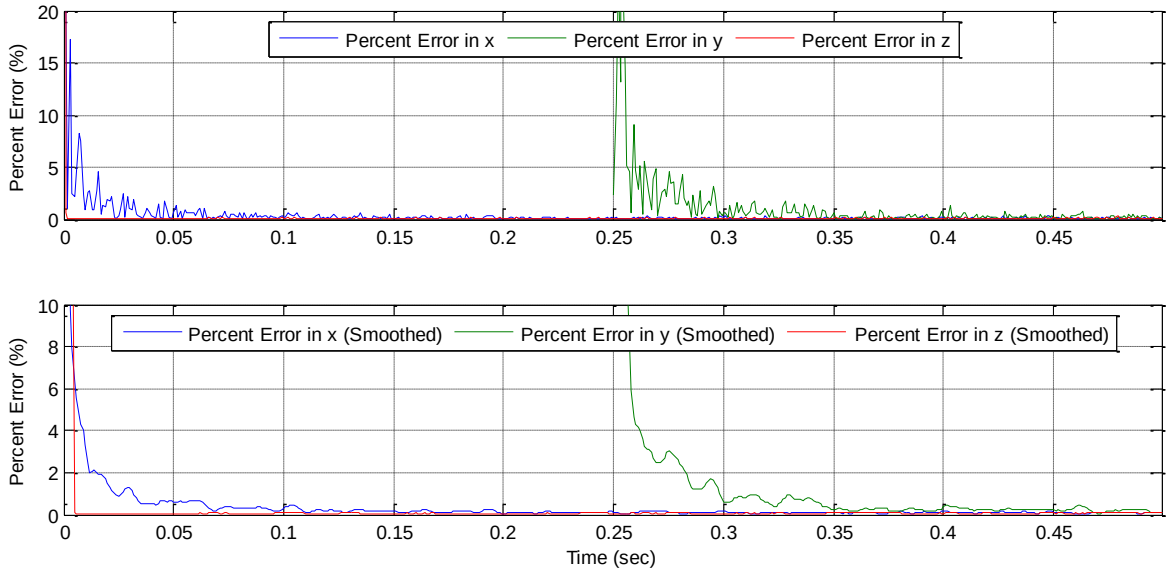

Figure 46 - Percent error of Kalman filter and smoothed Kalman filter in free-space

Figure 46 shows the convergence of a solution for the initial motion (between 0 and 0.25 seconds) as well as the second motion (between 0.25 and 0.5 sec). The first motion converges with error under 5% within 0.02 second (18 iterations) and the second within 0.01 seconds (9 iterations) and both eventually settle below 0.1% error over the length of the simulation, with

minimal initial overshoot. This figure also shows the error smoothed with a moving average filter (n = 10).

By using a Kalman filter, with an initial position estimation, based on a kinematic model, noisy measurement data can be used, as shown, to predict the position and velocity of a projectile with minimal error. Using this algorithm or a similar one in conjunction with the magnetic tracking algorithm proposed earlier, a system can be developed to track a magnetic source moving in three-dimensional space.

3.8 Data Acquisition System and Specifications

The three dimensional position calculations will need to be calculated in real-time, or near real time. Because the speed of the projectile will affect the calculated position, it is important to select hardware that is able to acquire data fast enough. The following, calculated with simple kinematic motion, is a table of sampling frequencies required to achieve centimeter and millimeter resolution travel at various speeds, assuming that this sampling frequency corresponds to the operational output frequencies of the magnetic sensor circuit (magnetometer, amplifier, etc.). Additional speeds and frequencies can easily be determined in a similar manner.

Table 7 - Sampling frequencies for 0.5" and 0.1" resolutions

Speed (mph)	Speed (in/sec)	Frequency for 0.5" resolution (Hz)	Frequency for 0.1" resolution (Hz)
1	17.6	35.2	176
5	88	176	880
10	176	352	1760
15	264	528	2640
20	352	704	3520
25	440	880	4400
50	880	1760	8800
100	1760	3520	17600

Data acquisition (DAQ) systems commonly have sampling frequencies up to 50 kHz for most of the commercial, off-the-shelf units. The range, in conjunction with a moderately fast personal

computer, should easily calculate the position of the magnetic source at position (x,y,z) and orientation with approximately centimeter accuracy in the three-dimensional positioning and using the algorithm discussed previously. Better accuracy can be achieved in the system, but at the cost of the sample rate and data acquisition system. The sampling frequency can be adjusted, as needed, to accommodate processing time after motion and noise equations are evaluated experimentally.

The data acquisition system must also be able to accept all of the inputs necessary to calculate the three-dimensional position. The layout on the sensor network in the previous section suggests 24, 1- or 2-axis magnetic sensors will be used, each requiring its own differential input. As the size of the sensor network grows or shrinks, the number of required inputs would as well. If possible, a data acquisition system capable of recording all sensors simultaneously would be ideal. Given these requirements, several systems were investigated. One of the possible solutions specifications [91] is shown in Table 8 below.

Table 8 - Data acquisition system specifications

Description	**Value**
Number of analog inputs (single ended)	80
Number of analog inputs (differential)	40
Number of analog outputs	2
Number of digital inputs and outputs	24
Sampling frequency	250,000 samples/sec
Resolution	16 bit

This data acquisition systems allows for 40 magnetic sensors (differential input) to be used separately, or a maximum of 13 sensor clusters. This would allow for a maximum grid acquisition rate of 6.4 kHz, and a minimum sensor resolution of 183 µG over the full scale of the sensor (±6 G). Additionally, multiple DAQ systems (ideally with identical sampling rates and resolutions) could be used to achieve the required number of sensor inputs. A block diagram of this system, including the magnetic sensors, signal conditioning, pre/post-processing, data acquisition, and interconnects, can be seen in Figure 47.

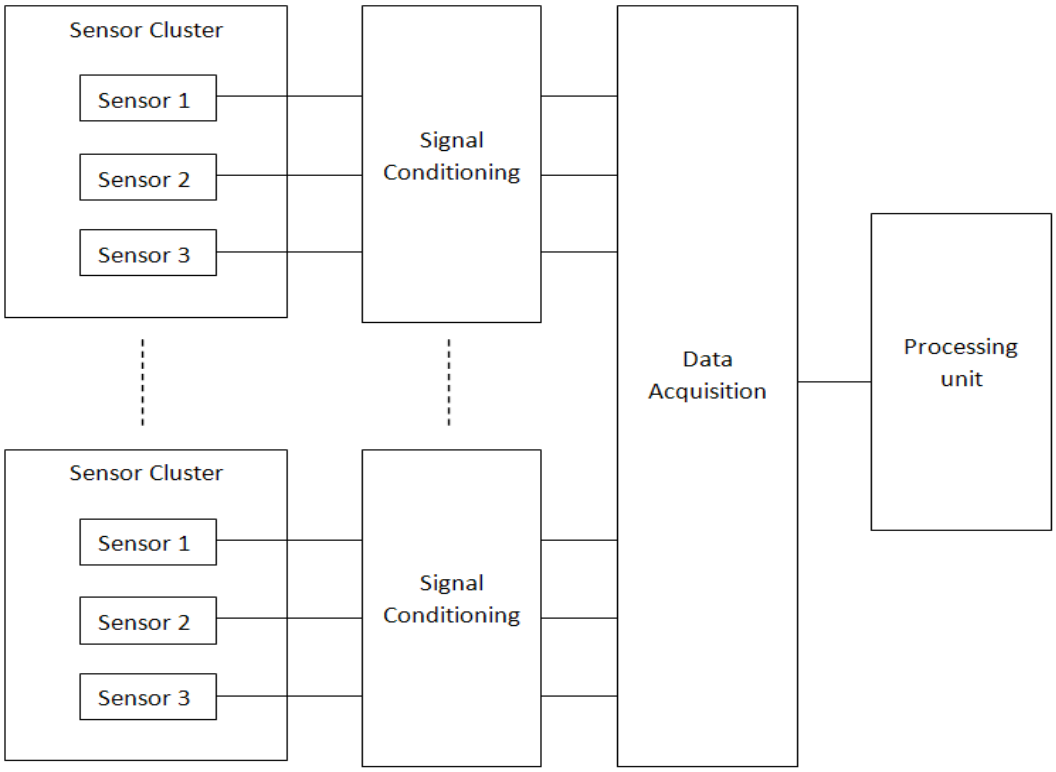

Figure 47 - Block diagrams of system with single acquisition system

In order to increase the maximum detection rate of the sensor network, additional data acquisition systems (A/D converters) can be used simultaneously. It is possible that each of the sensor clusters can have its own acquisition hardware, and the results can be polled to the processing unit at the same time. Microprocessors located on each sensor cluster can be used for this job. This allows for 40 possible sensor clusters, or 120 magnetic sensors. A block diagram of this method can be seen in Figure 48. However, this increase in data collection would be at the cost of additional and potentially expensive hardware that would be required for each sensor cluster, and was not further investigated in this research.

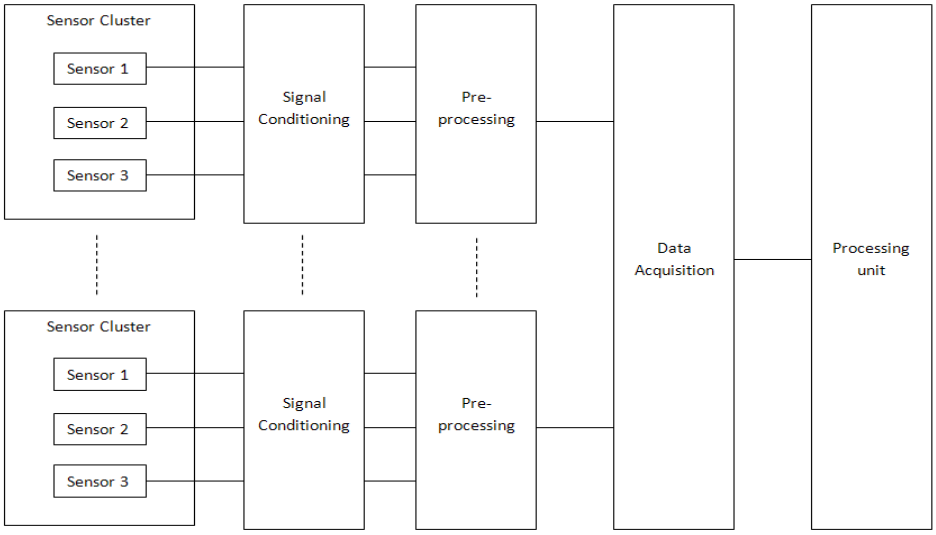

Figure 48 - Block diagrams of system with multiple pre-processors

Additionally, in order to increase the minimum resolution of the sensor, an acquisition system with a higher A/D resolution would also work. These systems come with a higher cost as well. The minimum detectable signal of the magnetic sensor noise is approximately 4 mG. The following chart, Table 9, shows the relation between minimum detectable signal and A/D resolution for a DAQ with an input range of ±5 V, a signal input range of 0-5 V, and a sensor sensitivity of 1 mV/mG, as discussed in the next chapter.

Table 9 - A/D resolution versus minimum detectable sensor signal

n-bit Resolution	Min. Detectable Signal (mG)
8	78.13
10	19.53
12	4.88
14	1.22
16	0.31
18	0.08

This suggests that for maximum sensor potential, at least a 14 bit A/D converter should be used, assuming that the minimum detectable signal can be reached with any experimental setup. Using a lesser resolution would result in a more accurate determination of not only position, but magnetic noise as well.

Chapter 4 – Experimental Approach and Design

Chapter 3 has outlined possibilities for an experimental apparatus—including the benefits and limitations of certain magnetic materials and their geometry, specifications of magnetic sensors, and possible configurations for sensor networks. Additionally, a method for determining position and orientation of a magnetic signature as well as a potential tracking and filtering algorithm has been proposed and evaluated under ideal circumstances. This chapter will describe the specification of the selected system components for the experimental apparatus, including magnetic sensors, the design of the experimental sensor network, and data acquisition hardware.

4.1 Magnetic Sensor and Support Circuitry

The basis of the magnetic tracking network is its single axis magnetic sensors. For this network, the Honeywell HMC 1021z [87] magnetic sensor was chosen based on time and cost constraints. This sensor is housed in an 8-PIN SIP package with the magnetically sensitive axis pointing up. Design characteristics are listed in Table 10.

Table 10 - HMC 1021z magnetic sensor design characteristics

Characteristic	Typical Value
Supply	5 VDC
Field Range	±6 G
Disturbing Field	20 G
Max Expose Field	10 kG
Sensitivity	1.0 mV/V_E/G
Resolution	85 μG
Bandwidth	DC to 5 MHz

In order to detect the magnetic field, support circuitry was needed. Because there is no amplification in the magnetic sensor, an amplifying circuit needed to be added. This sensor also has the ability to degauss itself if magnetically saturated; note that support circuitry for this sensor is also needed, specifically for signal amplification. A simple block diagram of the circuit used is provided below.

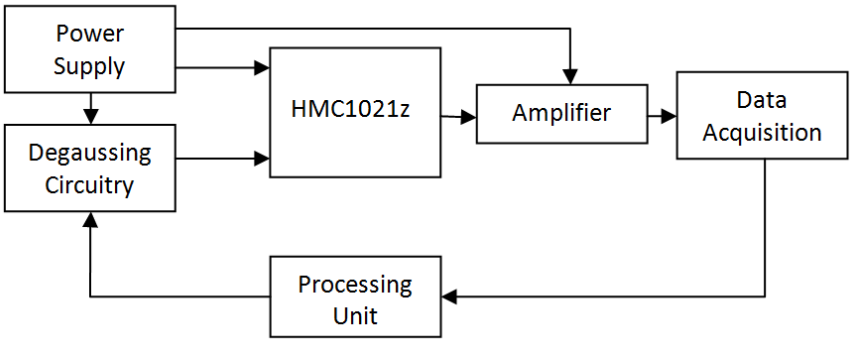

Figure 49 - Block diagram of magnetic sensor and support circuitry

The HMC1021z is a magnetoresistive sensor [87] that is comprised of a set of magnetically-variable resistors in a Wheatstone bridge configuration. The output of these sensors (mV) can be related to the magnetic field input (Oe) by the following manufacture plot, Figure 50 [87].

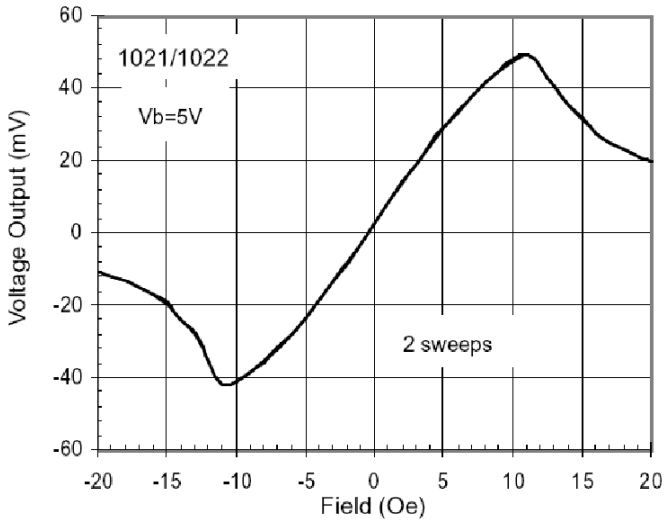

Figure 50 - Sensor output vs. magnetic field input for HMC1021z [87]

The following derivation relates the magnetic field strength input (in Oe) to the sensor output (in mV) for the linear portion between ± 10 Oe:

$$\boldsymbol{B}[G] = \mu_r \boldsymbol{H}[Oe], \quad \textbf{(4.1.1)}$$

where $\boldsymbol{B}$ is the magnetic flux density in G, $\boldsymbol{H}$ is the magnetic field strength in Oe, and μ_r is relative permeability (μ_r = 1.05 for Neodymium).

$$H = \frac{B}{1.05} \quad \textbf{(4.1.2)}$$

From Figure 50,

$$V = 4.7788 * H + 2.6172, \text{ and} \quad \textbf{(4.1.3)}$$

$$V = 4.5512 * B + 2.6172, \quad \textbf{(4.1.4)}$$

where V is the sensor output in mV.

(4.1.3) describes the relationship between the H-field and the sensor output for -10 Oe < H < 10 Oe, and (4.1.4) describes the relationship between the B-field and the sensor output for -10.5 G < B < 10.5 G, assuming a linear relationship over the domain. The output the sensor network will be -45.17 < V < 50.4 mV, and only valid in the specified field range. Note that 10 G corresponds to a distance of approximately 0.15 ft (1.8 inches) directly above the magnetic sensor for a 3.309 kG magnet, and will need to be accounted for in the design of the experimental apparatus.

The output of the magnetoresistive sensor will require amplification to take advantage of the DAQ. For this, a differential operational amplifier (op-amp) was used. A circuit diagram of a differential op-amp can be seen in Figure 51.

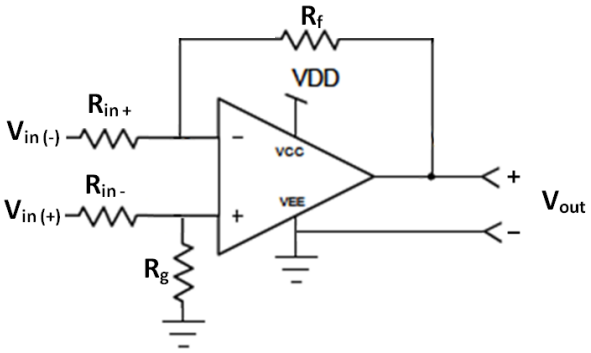

Figure 51 - Circuit diagram of differential operational amplifier

Using nodal analysis, the output voltage of this op-amp can be described as a function of the input voltages, where

$$V_{out} = \left[\frac{R_f + R_{in(+)}}{R_g + R_{in(-)}} \cdot \frac{R_g}{R_{in(+)}}\right] V_{in(+)} - \left[\frac{R_f}{R_{in(+)}}\right] V_{in(-)}, \quad \textbf{(4.1.5)}$$

where V_{out} is the output voltage, $V_{in(+)}$ and $V_{in(-)}$ are the input voltages, $R_{in(+)}$ and $R_{in(-)}$ are the input resistance, R_f is the output resistance, and R_g is the sink resistance.

In simplistic design case of $R_{in(+)} = R_{in(-)}$ and $R_f = R_g$, the output of the amplifier is given by

$$V_{out} = \frac{R_f}{R_{in}} * \left(V_{in(+)} - V_{in(-)}\right) \quad \textbf{(4.1.6)}$$

and the DC gain is given as:

$$G = \frac{R_f}{R_{in}}, \quad \textbf{(4.1.7)}$$

where G is the amplified DC gain.

$$V_{out} = \left[\frac{\left(sC + R_f{}^{-1}\right)^{-1} + R_{in(+)}}{R_g + R_{in(-)}} \cdot \frac{R_g}{R_{in(+)}}\right] V_{in(+)} - \left[\frac{\left(sC + R_f{}^{-1}\right)^{-1}}{R_{in(+)}}\right] V_{in(-)}, \quad \textbf{(4.1.5)}$$

where V_{out} is the output voltage, $V_{in(+)}$ and $V_{in(-)}$ are the input voltages, $R_{in(+)}$ and $R_{in(-)}$ are the input resistance, R_f is the output resistance, R_g is the sink resistance, C is the output capacitance, and s is a complex variable (jw).

Given design consideration of $R_{in(+)} = R_{in(-)} = 4.99\ k\Omega$, $R_f = R_g = 1\ M\Omega$, and $C = 1nF$, the frequency response of the magnetic sensor and support circuitry over operating conditions is shown in the following figure.

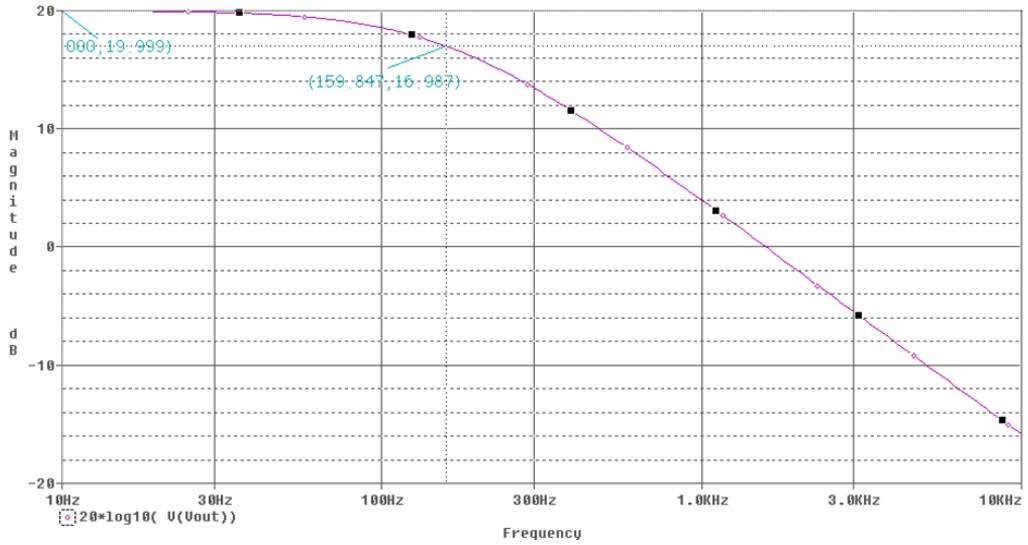

Figure 52 - Frequency response of single axis magnetic sensor and amplification, filtering circuitry

The filtered, cut-off frequency of the feedback impedance this amplifier is given by (4.1.9), as shown in Figure 52 to be 160 Hz at -3 dB from DC.

$$f_c = \frac{1}{2\pi R_f C}, \quad \textbf{(4.1.9)}$$

where f_c is the cut-off frequency and C is the output capacitance.

This configuration has an op-amp circuit gain of 200, implementing a low-pass filter with cut-off frequency of approximately 160 Hz. These design criteria (C, R_f) can easily be adjusted to accommodate any frequency response desired in future embodiments of this research.

The HMC1021z also has the ability to degauss itself, if the magnetic sensor becomes saturated. In order to do this, a 0.5A current, pulsed at a duration of 2 µsec, is required—once in the positive and once in the negative directions (to clear both sides). A pair of complementary power MOSFETs, in totem configuration, is used to achieve this, as shown in Figure 53. The Honeywell suggested magnetic detection circuitry schematic [87], shown in Figure 53, was used.

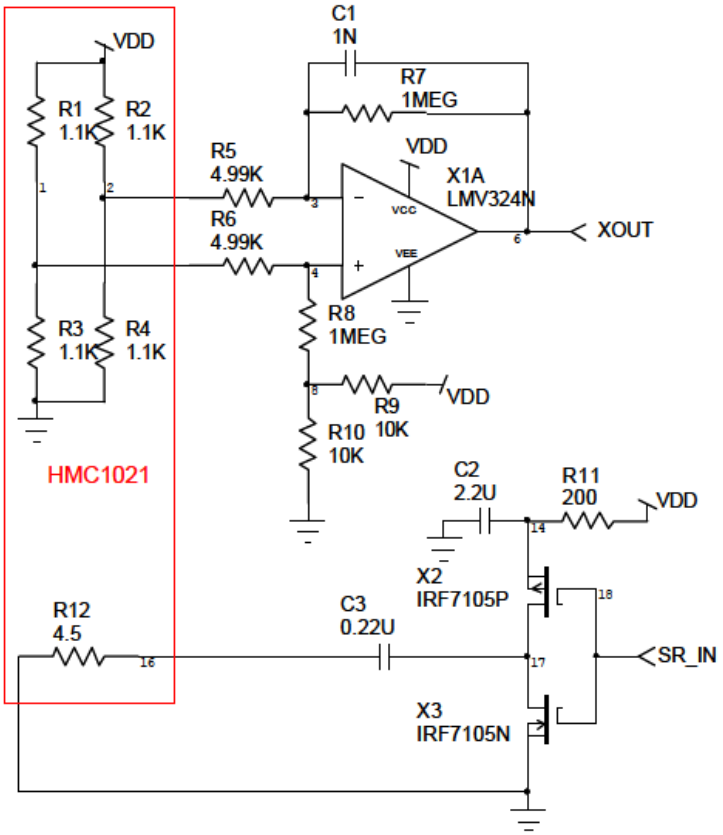

Figure 53 - Magnetic sensor circuit schematic [87]

The circuit implemented here uses a 5 V excitation. The single-input supply sensor uses a simple voltage divider to center the output at 2.5 V to achieve signed measurements. Given a sensitivity of 1.0 mV/$V_{EXCITATION}$/G (typical), with $V_{EXCITATION}$ = 5 V and a gain of 200 (typical), the

apparent sensitivity becomes 1 V/G. This allows for magnetic measurements between ± 2.5 G. Using the magnetic source selected (3.309 kG), the minimum detectable distance is 0.3 ft (i.e. if the source is any closer it will saturate the magnetic sensor) once the Earth's magnetic field is taken into account.

During operation, magnetic noise and transience from the Earth's magnetic field can play a large role in the effectiveness of a DC magnetic sensor network. This noise must be accounted for in the maximum detectable distance of the sensor. Figure 54 illustrates a 30 minute data sample of transient Earth field. This data shows mean magnetic noise of 269 mG, with a mean variation of approximately 4 mG, with a maximum of 6.6 mG over the time period examined. Note, that this contains a combination of magnetic source signal and magnetic noise, both intrinsic and extrinsic.

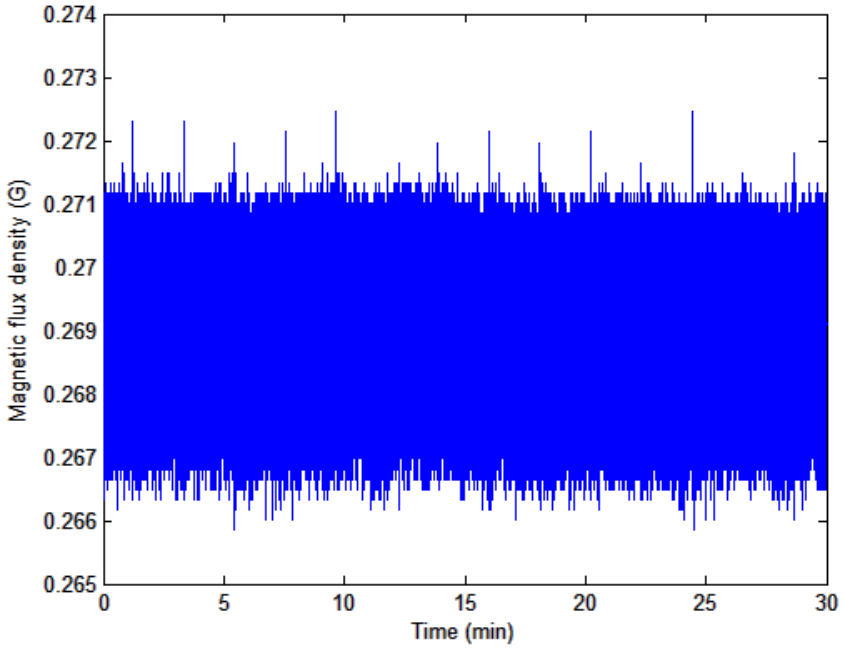

Figure 54 - Transient noise from magnetic sensor and support circuitry

Additionally, operational noise can be introduced based on sampling frequency, using 0.1 Hz as an approximation of a DC magnetic source, Figure 55 approximates a magnetic noise density of 800 nV/√Hz, or 160 μG/√Hz [87] (given a typical sensitivity of 5.0 mV/G). This is much lower than the other systematic noises presented here.

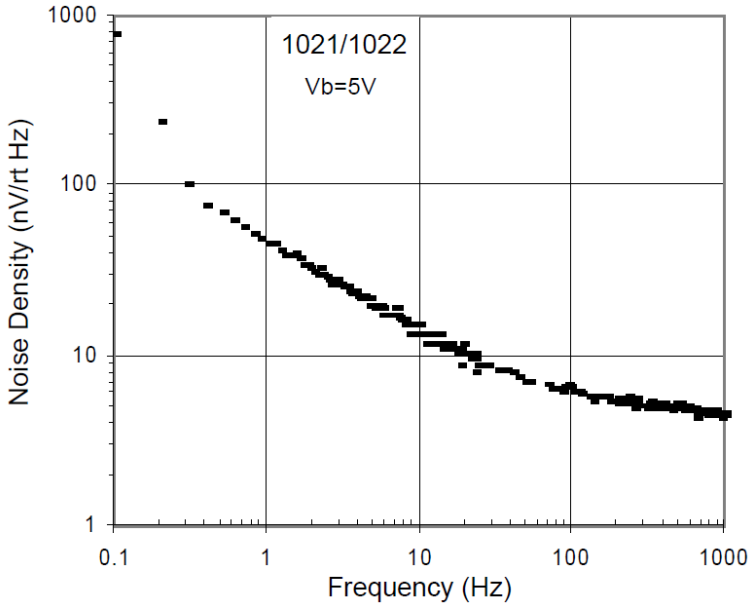

Figure 55 - Magnetic sensor (HMC 1021z) noise vs. frequency[87]

The manufacturer's suggested schematic, and the parts included, was used to build twelve single-sided printed circuit boards. A detailed list of parts and their measured values is included in Appendix A. A PCB layout schematic is included in Appendix B. Input / Output terminals on the PCB are available to (1) supply power, (2) retrieve sensor data after it has been amplified and filtered, and (3) allow the user or computer to set and reset the sensor's internal saturation circuitry. A sample of the PCB made is shown in Figure 56.

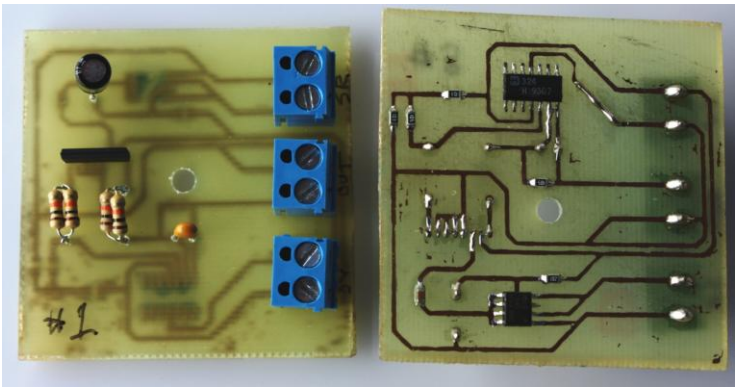

Figure 56 - Sample PCB including magnetic sensor and support circuitry

4.2 Magnetic Sensor Network Layout

The magnetic sensor network is composed clusters of twelve magnetic sensors. Each sensor cluster is affixed to a 1 x 1 ft Plexiglas board. The board is referenced from the center, and each individual sensor is positioned on the board (Figure 57) so its exact position is known. The exact positions of the individual sensors are used to calculate the average value of the magnetic field and the magnetic surface normal vector used for magnetic source position computation.

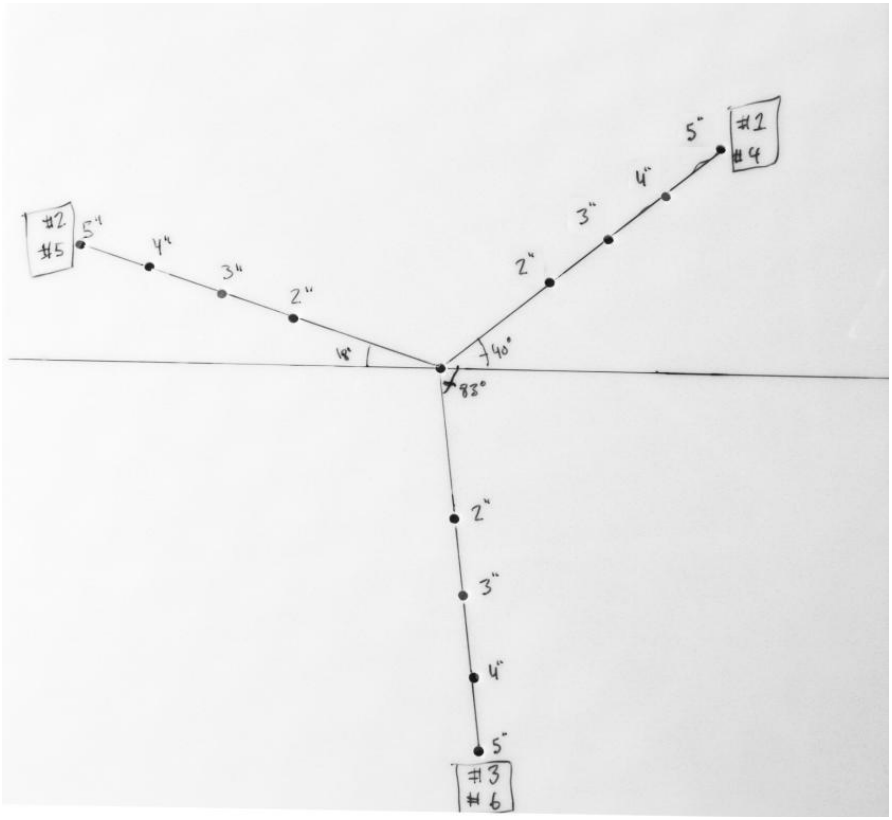

Figure 57 - Sensor cluster - Positions of magnetic sensors

For the purposes of testing, and simplicity, all sensors and sensor clusters will be coplanar. Each of the four sensor clusters are arranged on a larger platform. This platform will allow the centers of the sensor clusters to be spaced one, two, and three feet apart from one another. The density and scalability of this design will be simulated in the following sections. Figure 58 shows a simulation of one possible configuration for the magnetic sensor network. The absolute position of all (12) sensors in the network can be found in Appendix C.

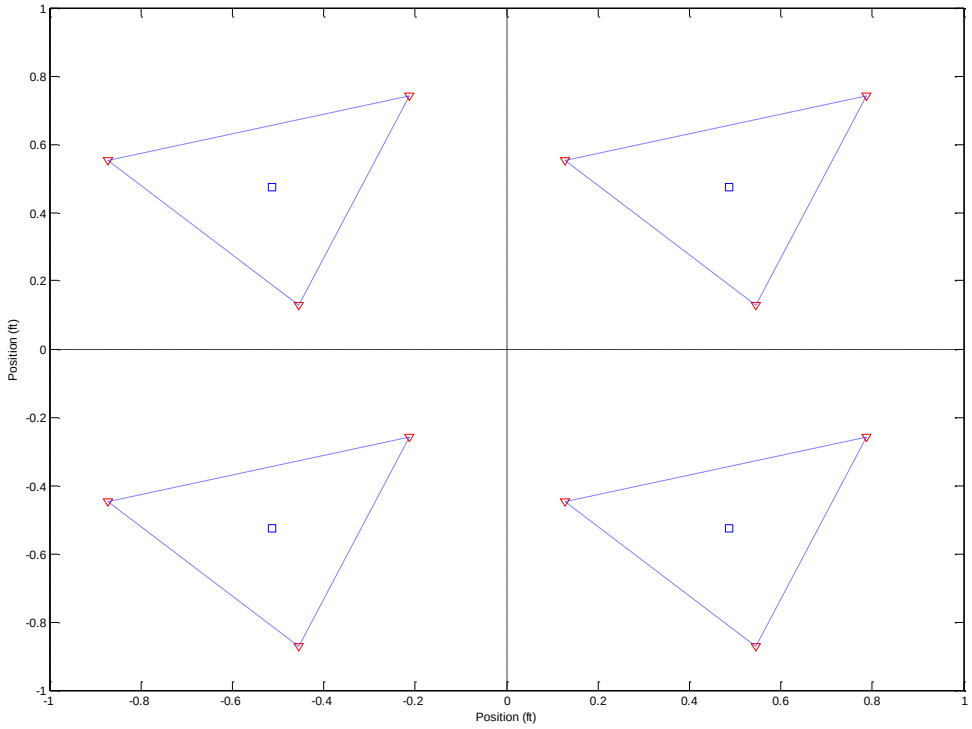

Figure 58 - Simulated sensor network with 12 sensors, 4 sensor clusters

Although the initially proposed network uses only 4 uniformly spaced sensor clusters, this sensor network layout yields the potential for many more, non-uniformly spaced sensor clusters to be added. During initial testing, because of the distance between these clusters, poor quality of position calculation resulted. For this reason, a modified sensor cluster design was created and tested. The clusters nearest to the magnetic source will then have the best signal to noise ratio, and relying on these alone will produce a higher quality position results. This augmented sensor network, shown in Figure 59, has (15) non-overlapping clusters, with the possibility of more overlapping sensor clusters.

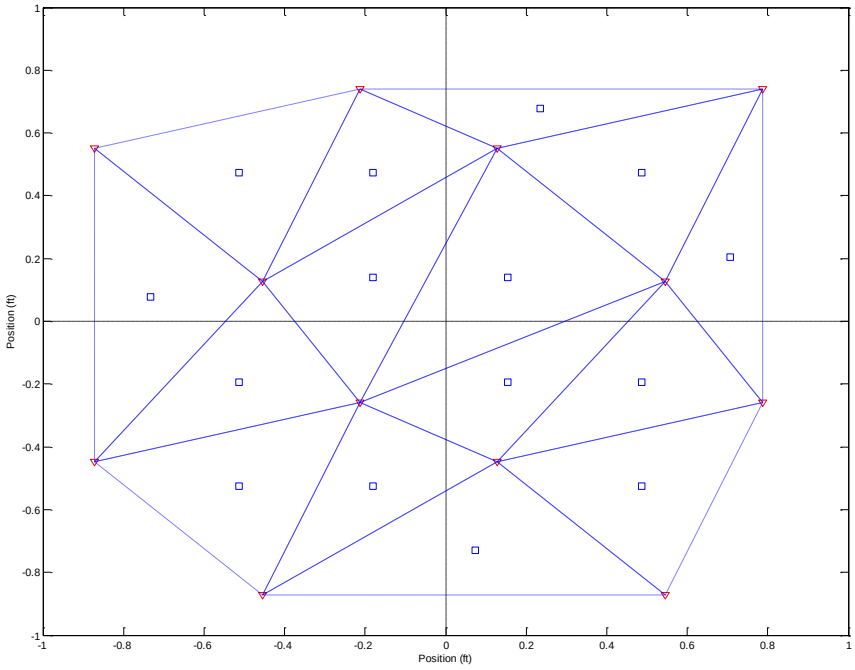

Figure 59 - Simulated sensor network with 12 sensors, 15 sensor clusters

This is the configuration that was used in the experimental sensor network. Figure 60, shows the actual magnetic sensor network. The absolute position of the center of all (15) clusters in the network can be found in Appendix D.

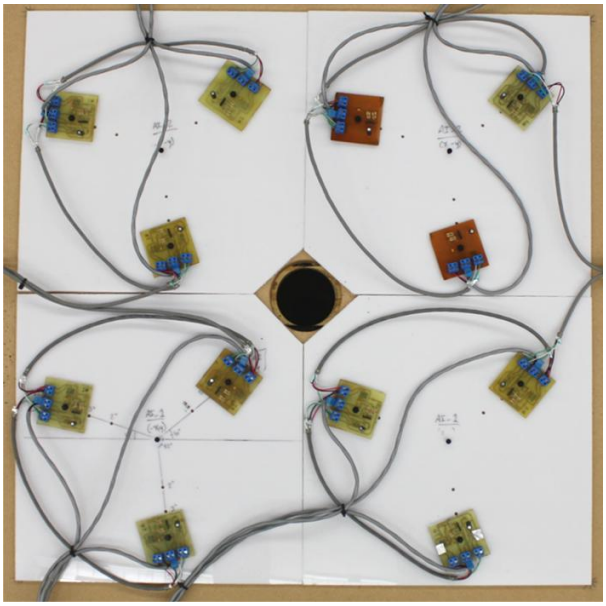

Figure 60 - Experimental sensor network with 12 sensors

Using this sensor network configuration, in conjunction with the experimental and simulated data from the previous section, projections can made on the signal strength and number of sensors used to detect a magnetic source. The following simulations, based on a magnetic source of 3.309 kG and the above sensor network layout can be seen for a source one foot (Figure 61) and two feet (Figure 62) above the origin, plotted against the 4 mG average noise floor.

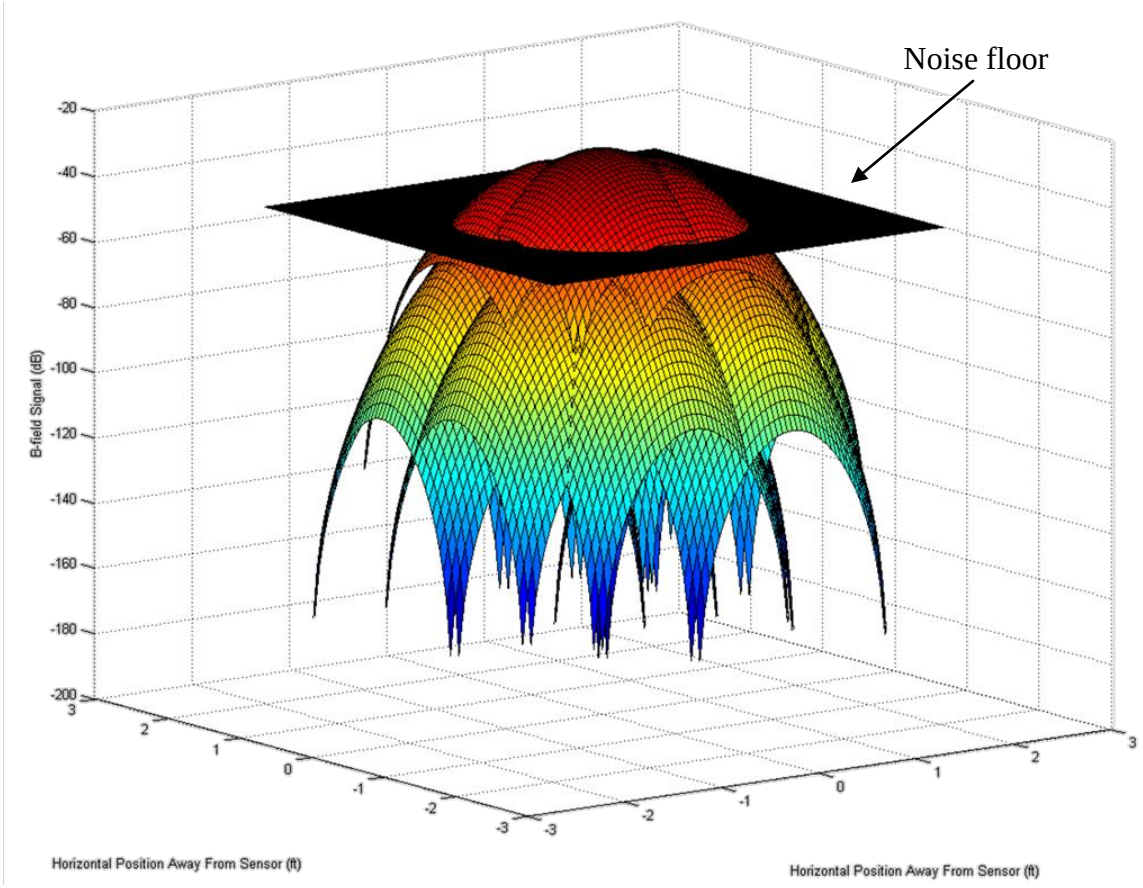

Figure 61 - Sensor network response (dB) for magnetic source 1 ft above origin

Where the magnetic flux density (signal) is represented in dB as:

$$dB = 20\log_{10}(Signal) \quad \textbf{(4.2.1)}$$

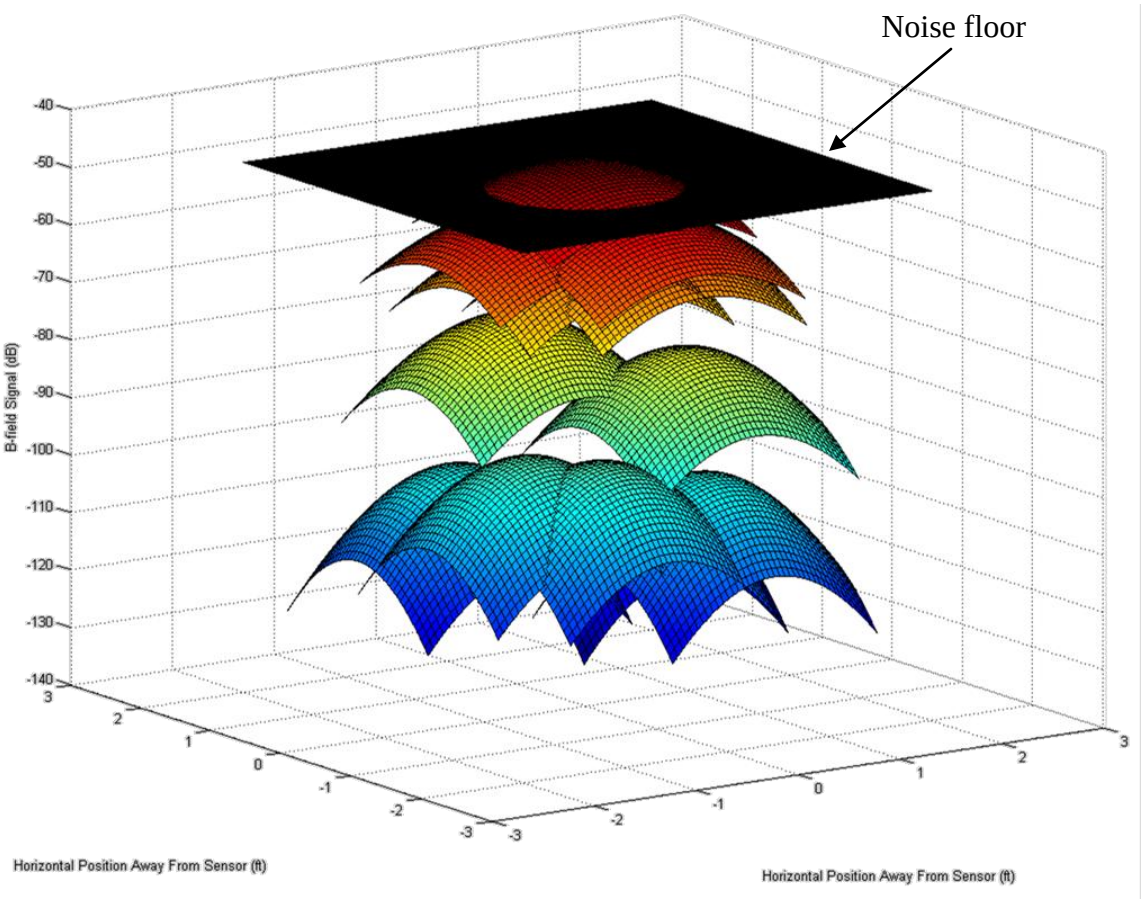

Figure 62 - Sensor network response (dB) for magnetic source 2 ft above origin

These figures indicate the signal response (in dB) from the interaction of each sensor with the magnetic source. For any position on the sensor network, there are between 7 and 9 magnetic sensors that are able to obtain measurements above 4 mG when the magnetic source is 1 ft above the center. Likewise, for any position on the sensor network, there are between 1 and 3 magnetic sensors that are able to obtain measurements above 4 mG when the magnetic source is 2 ft above the center. This second projection is why tracker-estimators with good initial position estimation are a good addition to this tracking algorithm.

4.3 Data Acquisition System for a Magnetic Sensor Network

The data acquisition hardware for the magnetic sensor network has multifaceted requirements including: required number of analog sensor inputs (12 differential), adequate sampling rate (> 1kHz per sensor), and appropriate resolution (>14 bit). Due to cost constraints, the single DAQ card proposed in previous sections is not feasible. Instead, two seemingly identical, 8 differential analog input, 16 bit DAQ cards were used (NI DAQCard-AI-16XE-50 [92] and NI PCI-6013 [93]). The primary design characteristics are listed in Table 11.

Table 11 - Data acquisition system specifications for NI DAQCard-AI-16XE-50 and NI PCI-6013

Description	**Value**
Number of analog inputs (DIFF)	8
Number of digital inputs and outputs	8
Sampling frequency	200,000 samples/sec
Resolution	16 bit
DAQ Input Range	-5 VDC to +5 VDC
Signal Input Range	0 VDC to +5 VDC

Changing the resolution of the DAQ system will alter the maximum detection distance of the sensor network. Previous calculations show that the maximum detectable range of a magnet with B_r = 3.309 kG will be 9.05 ft for a magnetic sensor with a sensitivity of 85 μG [87] (on-axis, with no external noise) measured on-axis. Assuming that the external noise floor averages 4 mG, as shown with experimental data, the maximum detectable range of the sensor network then is reduced to approximately 3.9 ft (on-axis), once accounting for the steady-state Earth's magnetic field. Figure 63 shows a diagram of the experimental sensor network, including magnetic sensors, signal conditioning, data acquisitions, and processing unit.

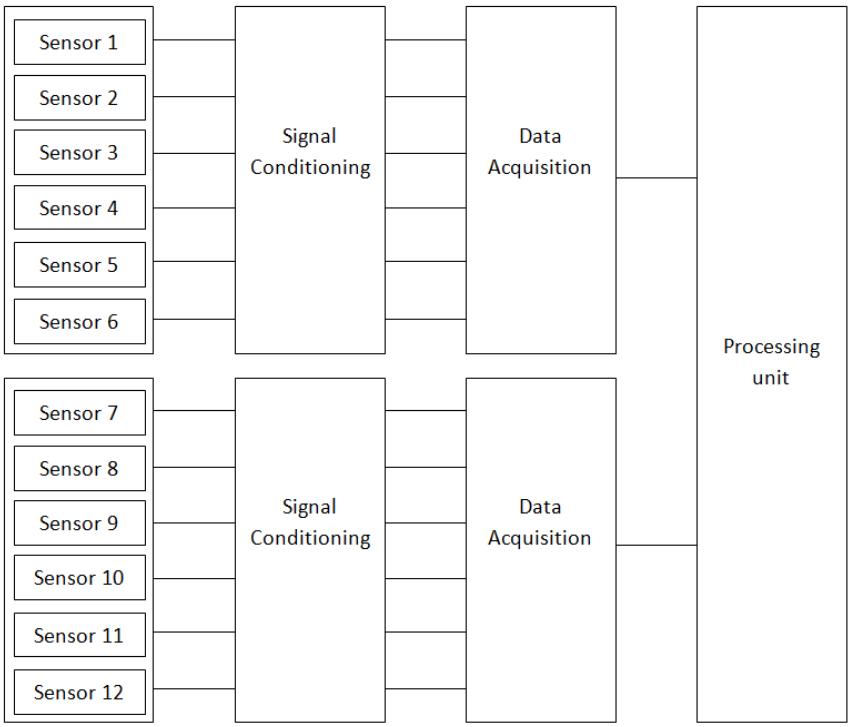

Figure 63 - Block diagrams of experimental sensor network

4.4 Experimental Testing Apparatus

In order to test the validity of the tracking system, an experimental testing apparatus that is capable of manipulating both three-dimensional position and orientation was designed and built. To accomplish this, two testing apparatus were constructed, one for three-dimensional position and one for orientation.

4.4.1 Rotational Experimental Testing Apparatus

To verify that the system is successfully able to track the changes in orientation of a magnetic source, a rotational testing apparatus was designed. This apparatus spins a magnetic source with a radius of 10 inches around the center, 12 inches above the sensor network, as seen in Figure 64. This vertical distance ensures that the magnetic sensors will not saturate, given conditions stated in the previous section.

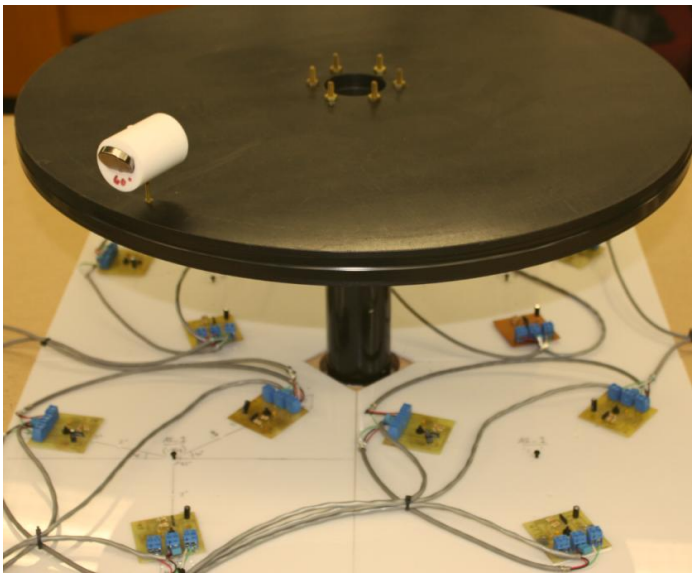

Figure 64 - Rotational testing apparatus

The magnet is held in place at angles of $\theta = 0°$, 15°, 30°, 45°, and 60° using slugs affixed to the rotating plate. This configuration allows for the sensor network to detect sources up to ±60° around the x-axis and around the y-axis. These slugs can be seen in Figure 65.

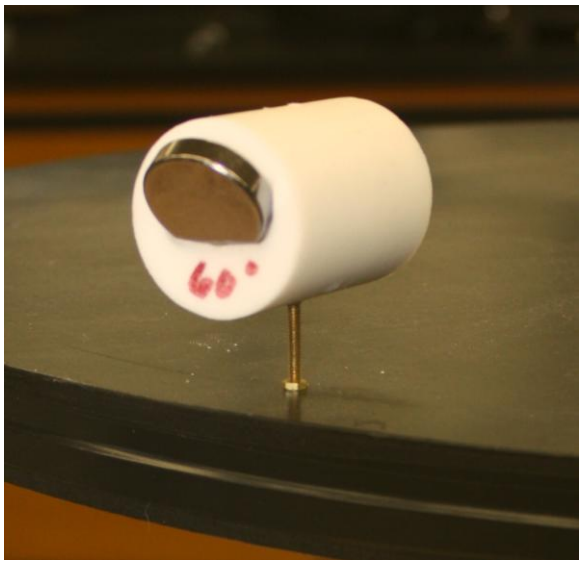

Figure 65 - Magnetic slug holder

The platform is rotating at approximately 33 revolutions per minute (62.8 inches/rev or 34.56 inches/sec), which can be used as an input to the Kalman tracking algorithm. Rotating at a constant velocity, data will be collected using the five angles stated, and compared to the theoretical. Because the magnetic field strength is weaker for a source at 90° above the sensor network, it is expected that the results of the higher angles (45° and 60°, and higher) will be much noisier than the smaller angles. This will be verified with experimental testing.

4.4.2 Linear Experimental Testing Apparatus

To verify that the system is able to track changes in three-dimensional space, a linear testing apparatus was designed. This apparatus allows the magnetic source to traverse the entire sensor network, accelerating under the force of gravity with friction loss, as seen in Figure 66. This apparatus is 5 feet in length, at an incline of 15° starting 2 feet and ending 1 foot above the sensor network, and uses the same magnetic slug holders as the rotational apparatus, which will allow experimental testing to verify that as the magnetic source approaches 90°, the magnetic strength approaches zero. These dimensions ensure the sensors will be able to detect the magnetic source, as described in the previous section.

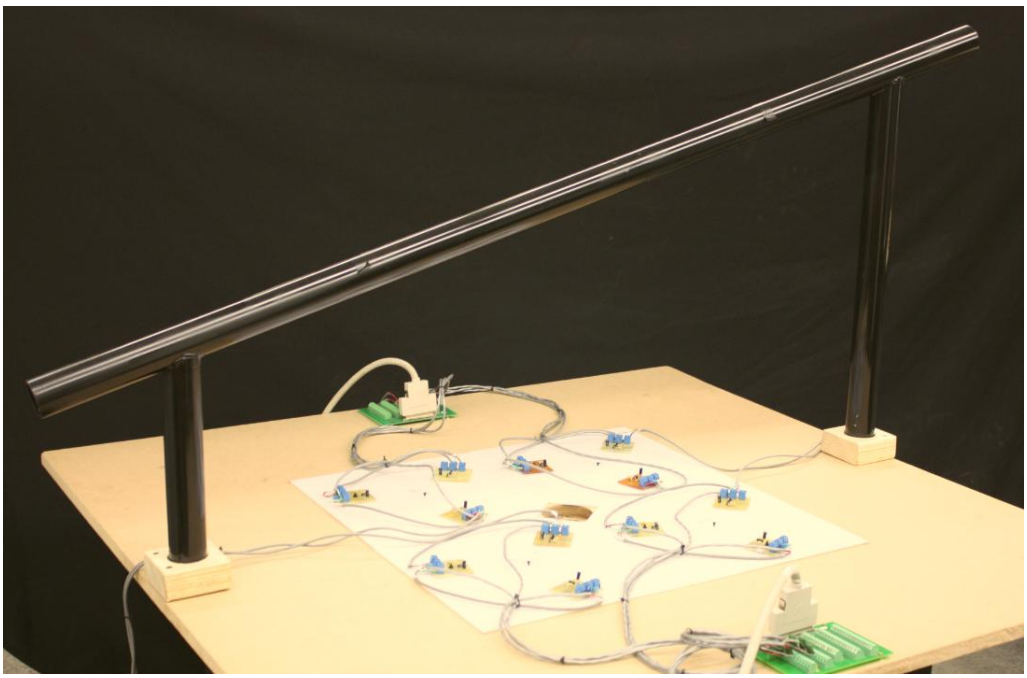

Figure 66 - Linear testing apparatus

Initial testing will limit the linear track to the 2 by 2 ft section above the sensor network, which can be expanded to cover the entire span track (4 ft). Because the magnetic strength is inversely proportional to distance cubed, weaker strengths will be recorded at the start of the tracking.

The combination of the rotational and linear testing apparatuses will validate the effectiveness of tracking system in all three dimensions of position and two degrees of orientation of the magnetic source.

Chapter 5 – Results

The previous chapter has outlined an experimental approach and design, including two experimental testing apparatuses. This chapter will discuss sensor network calibration as well as the experimental results for both the rotational and linear scenarios.

5.1 Sensor Network Calibration

In order to collect meaningful data, the sensor network had to be: (1) calibrated to achieve uniform gains across all magnetic sensors (hardware level), (2) tuned to report identical results at a fixed distance (software level), and (3) able to compensate for the offset due to the Earth's magnetic field.

The hardware calibration was initially performed using components for the amplifier circuitry (Appendix A). The magnetic sensor had an initial output range of 5 mV/G and the amplifier circuitry that was added supplied a hardware gain of approximately 200. This value varied between 200.72 and 206.90 due to the variance in the components used (Appendix A). Each sensor was normalized, compensating the variance in resistances.

A baseline reading was taken before every experiment. Sensors are able to detect positive and negative B-fields with outputs between 0 and 5 volts and an ideal zero field reading of 2.5V. This calibration removed the mean magnetic field of the Earth, as well as the mean magnetic noise from the power supply and the motor for the rotational platform.

This configuration only takes advantage of half of the DAQ input, essentially reducing it to a 15 bit resolution device. These values were used to create an offset and force baseline readings back to 2.5 V. The cause of the initial deviations from 2.5 V was the tolerance of the components that had been used to build the magnetic sensor board, mainly the amplification circuitry.

A sensor calibration routine was used to tune the sensors to a specified value at a fixed distance. An eight-point calibration was performed on each sensor, at distances 6 to 13 inches (on axis) from the sensor. Pre- and post-calibration data can be seen in Figure 67 and Figure 68, and the remaining sensor calibration data can be seen in Appendix A (Calibration Gain).

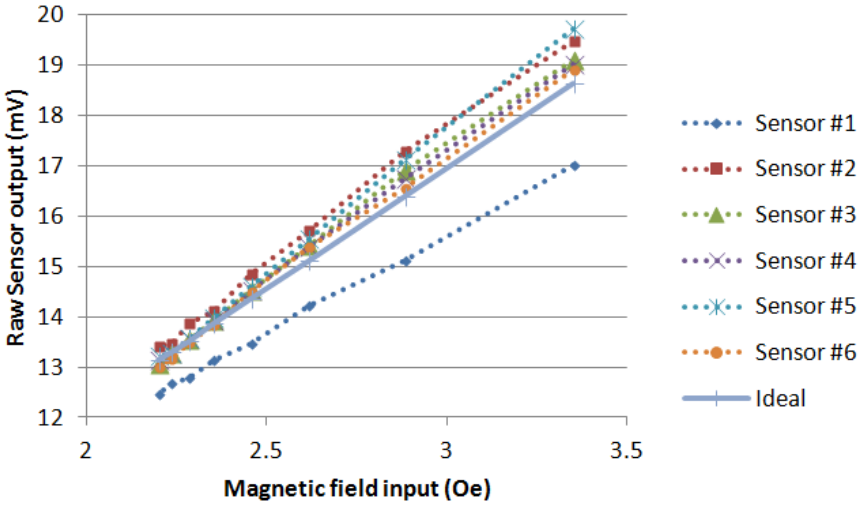

Figure 67 - Pre-calibration data

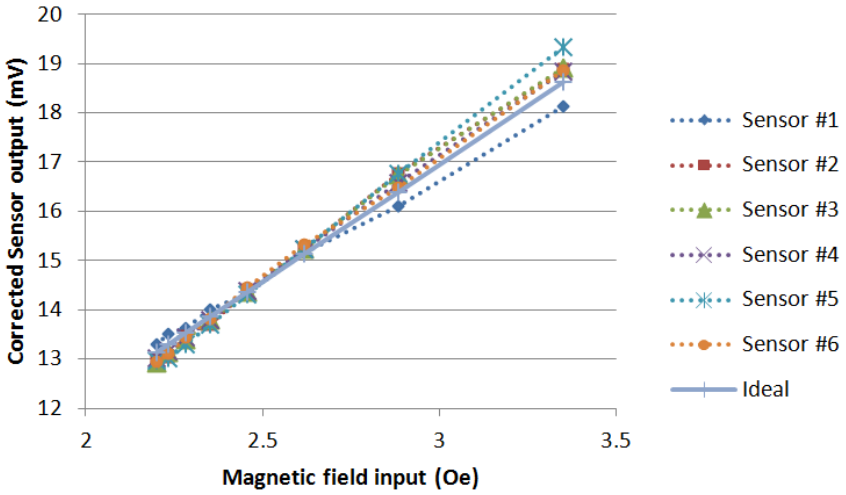

Figure 68 - Post-calibration data

Before calibration, the standard deviation was 163.5 mV (with amplifier gain) and 0.986 mV (output of sensor). After calibration, the standard deviation was 47.1 mV (with amplifier gain) and 0.325 mV (output of sensor).

5.2 *Results of Rotational Testing*

Custom software was developed and used to analyze the data collected for the rotational case, including two-dimensional position and orientation. This data was sampled at 1 kHz for 1 circular revolution. The output of the sensor network is shown in Figure 69

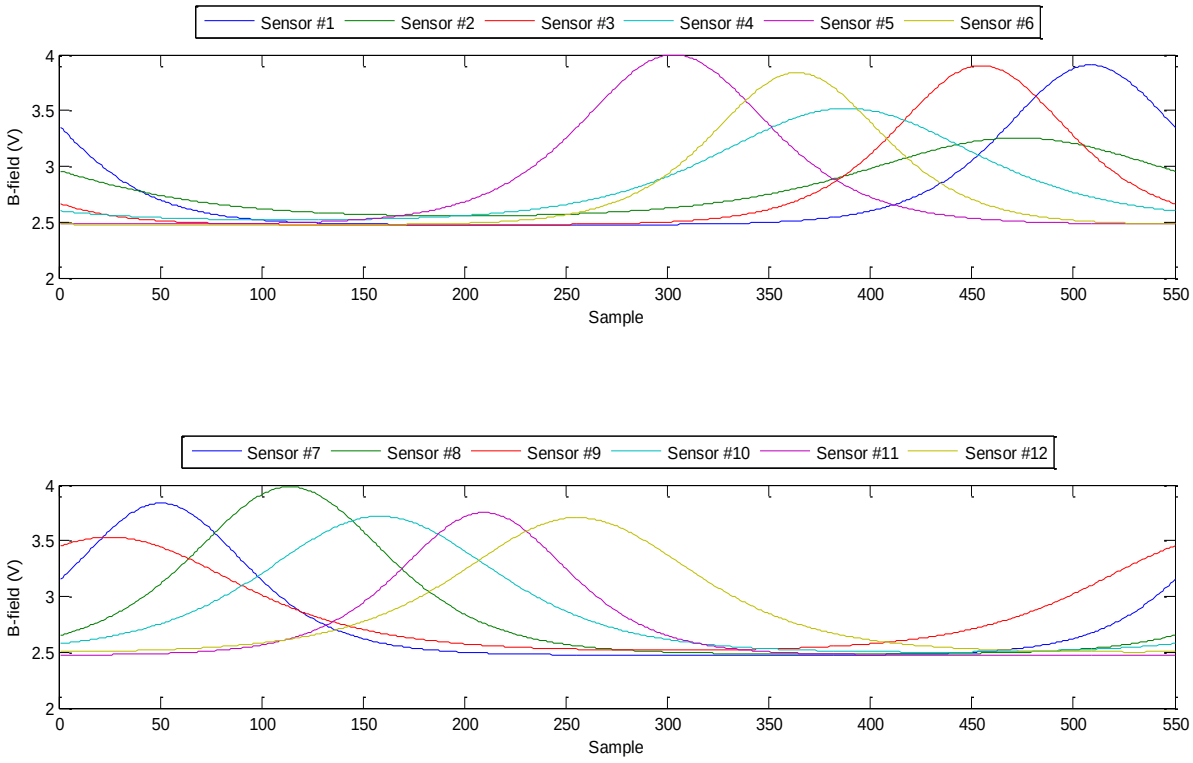

Figure 69 - Output of magnetic sensors for rotating test apparatus (θ = 0°)

From these plots, it can be seen that the magnetic source is moving in the proximity of each magnetic sensor, completing one rotation, traveling at approximately 33 revolutions per minute about a 10 inch radius (34.56 inches/sec), around the sensor network.

In order to remove the effect of this non-uniform sensor network layout, stray ambient noise, and system power noise due to the power supply and rotation apparatus, a simulated plot of position was created using an ideal magnetic source traveling about the sensor network and was calculated using mean position while θ = 0°, 15°, 30°, 45° and 60° (Appendix G), shown in

Figure 70. This dataset was used as a baseline for systematic error, which was removed from all position calculations.

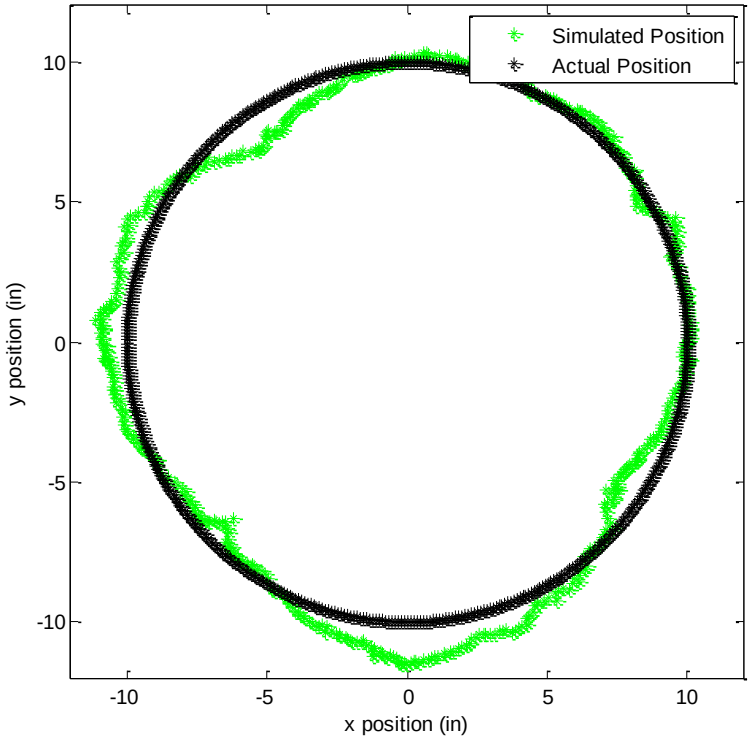

Figure 70 - Simulated position for rotating test apparatus using ideal magnetic source as a baseline for systematic error

A plot of the calculated radial position is shown in Figure 71. These positions are calculated using the method discussed in Chapter 3. In the figure, the black points are the theoretical (actual) position of the magnet, rotating in a circle with a radius of 10 inches. The blue points are the calculated position based on the position algorithm. The red points are the estimated position of the magnetic source based on the calculated points and the Kalman estimation algorithm with a variance of 0.01 inches^2. Figure 72 shows a three-dimensional plot of the same information. The initial position for the Kalman estimator is at the origin, (0,0,0) inches.

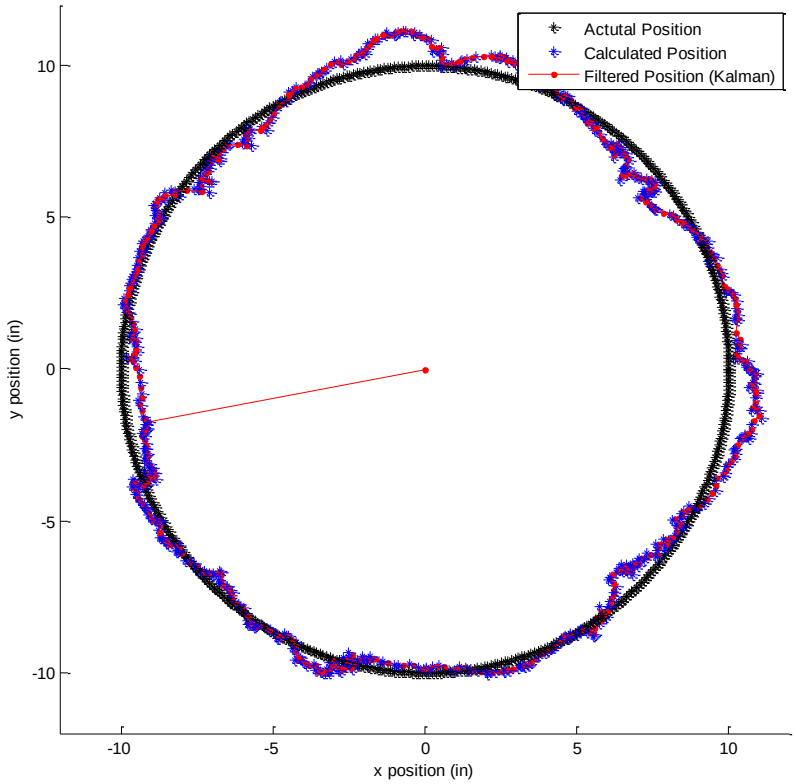

Figure 71 - Radial position for rotating test apparatus (θ = 0°, 15 clusters)

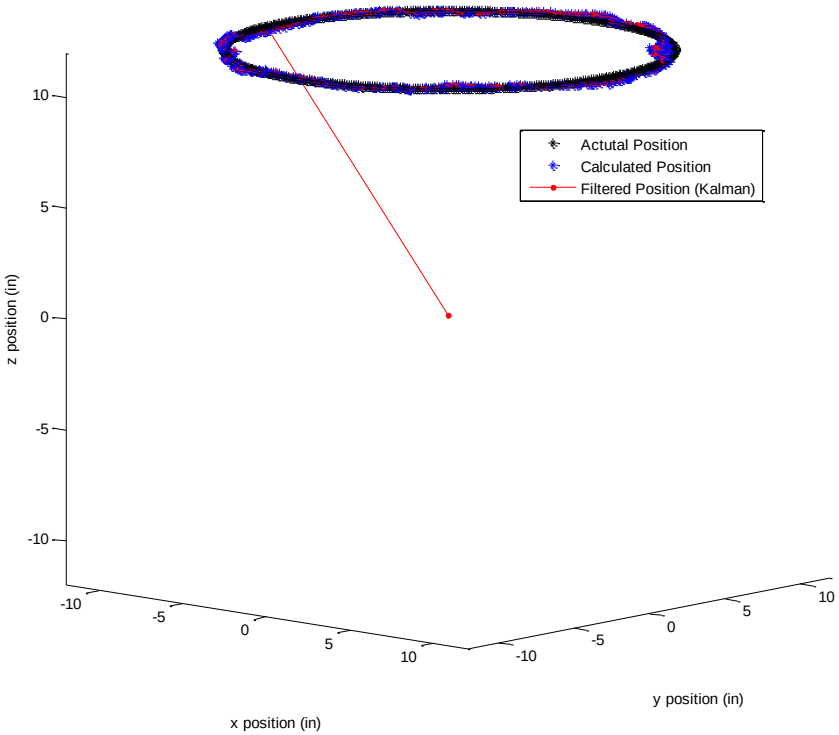

Figure 72 - Position for rotating test apparatus (θ = 0°, 15 clusters)

Figure 73 shows a plot of the calculated angles (elevation and rotation). The red line is the calculated θ (elevation above the x-y plane), which is also the actual angle of the magnetic source in its holder. The blue line is the calculated φ (rotation about the z-axis) for one revolution around the sensor network. The dashed lines show the actual value of the corresponding color.

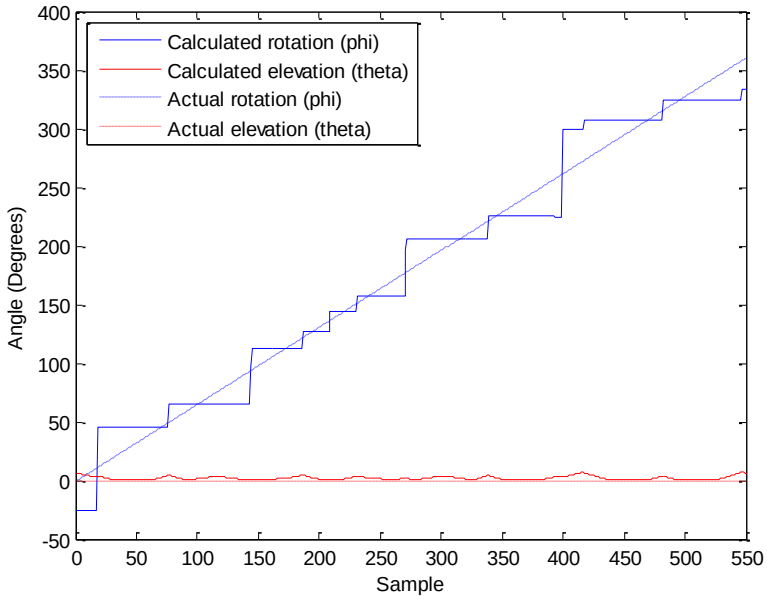

Figure 73 - Orientation for rotating test apparatus (θ = 0°, 15 clusters)

Figure 74 shows a plot of percent error for the simulation. The blue line shows percent error in the radial direction, and the green line shows percent error in the z-direction. The red line shows the overall percent error (both radial and z-directions). The dashed lines show an average value of the corresponding color, between 0% to 30% error.

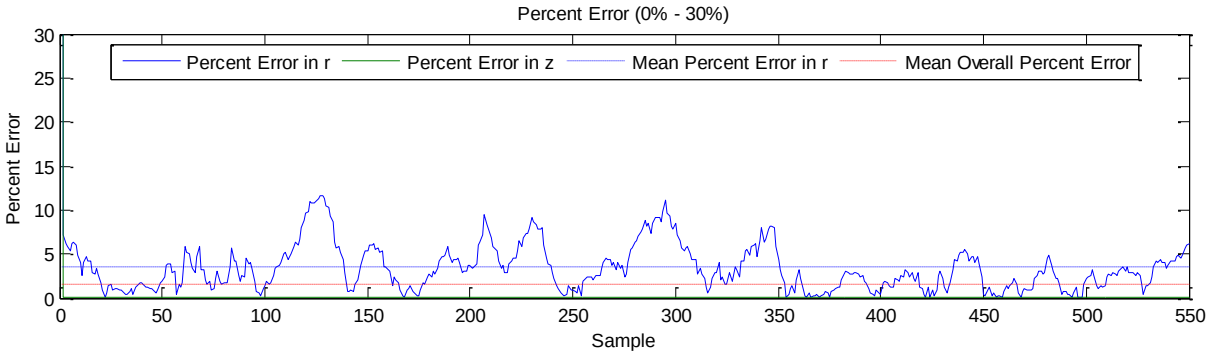

Figure 74 - Percent error for rotating test apparatus (source angle = 0°, 15 clusters)

Using the same method, additional sets of experimental data were collected and analyzed with the magnetic source at angles of 15°, 30°, 45°, and 60° (Appendix G). Additional data and solution sets are in Appendix G. Using the experimental data collected, a summary of results can be seen in Table 12 (position) and Table 13 (orientation).

Table 12 - Summary of results for rotating test apparatus (position)

	Position			
Magnetic Source Angle	Mean Radial Error (%)	Mean Z Error (%)	Mean Overall Error (%)	Max Overall Error (%)
0°	3.54	0.19	1.55	4.90
15°	2.45	0.19	1.10	2.78
30°	2.41	0.19	1.08	3.18
45°	3.20	0.19	1.40	4.63
60°	5.65	0.19	2.41	6.37
75° †	5.61	0.19	2.38	6.40
90° †	4.19	0.19	1.79	5.34

† 75° and 90° were not experimentally tested, these are simulated results.

Overall error is reported at less than 2% on average with 6.4% for the worst case. The majority of this error can be attributed to the systematic (Figure 70) and environmental magnetic noise. Additional error can be attributed to the number and spacing of the magnetic sensors. The layout used for this experimental was a first attempt, and is not optimized.

Table 13 - Summary of results for rotating test apparatus

	Orientation	
Magnetic Source Angle	Mean Difference (Rotation, °)	Mean Difference (Elevation, °)
0°	13.50	2.19
15°	13.79	18.72
30°	13.85	22.65
45°	13.92	23.16
60°	13.76	27.95

Because the models for θ and φ were developed using a more dense sensor network (> 10 sensors per ft^2), estimates for those angles in a 12 sensor (3 sensors per ft^2) network was poor.

The average rotation angle was 13.5°, which is directly limited by the number and position of the sensors, as previously discussed. The average elevation angle performed poorly because, in this scenario, the magnetic source was never directly above a sensor for a period of time, which is what the model was based upon. A simulated case, containing 441 sensors (spaced every 0.5 inch across the sensor network, 27 sensors per ft^2) in the same footprint, shows the operability of the model within a more dense sensor network. A plot of this layout can be seen in Figure 75, with simulated values for θ and φ included in Figure 76. Table 14 shows a summary of predicted elevation angles and differences from theoretical.

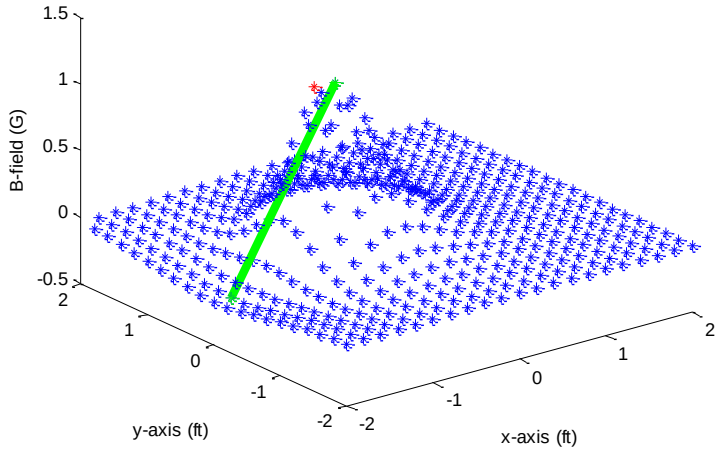

Figure 75 - Simulated network with 441 uniformly spaced sensors (27 sensors per ft^2)

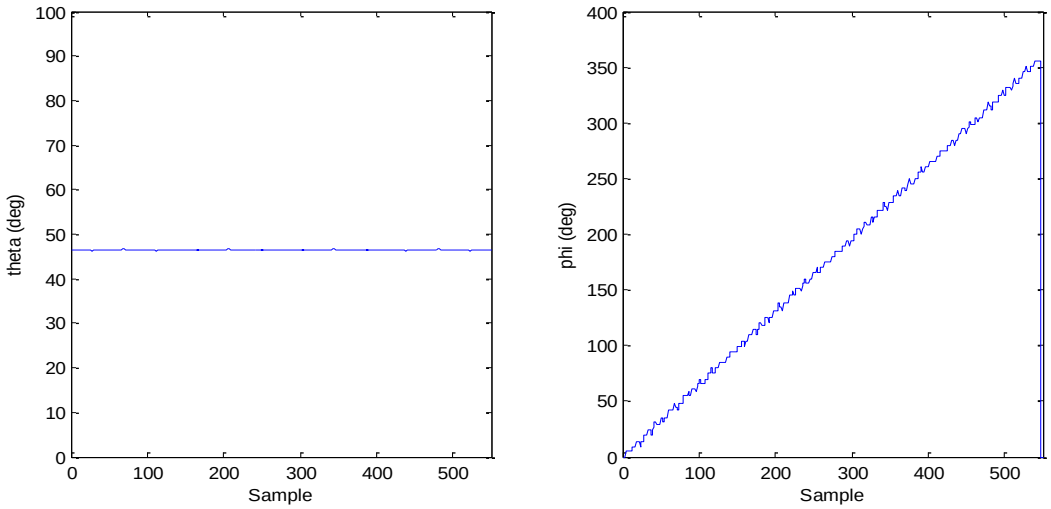

Figure 76 - θ and φ in simulated network with 441 uniformly spaced sensors (27 sensors per ft^2)

Table 14 - Theoretical vs. simulated θ for network with 27 sensors per ft^2

Theoretical (Actual) θ	Calculated θ	Difference in θ
0°	-1.84°	1.84°
15°	14.05°	0.95°
30°	31.40°	1.40°
45°	46.58°	1.58°
60°	61.32°	1.32°
75°	75.20°	0.20°
90°	89.21°	0.79°

It is apparent from this data that this model responds much better to networks with a dense grid of sensors. Figure 77 shows a simulated plot of sensor network density vs. percent error (θ, φ, and z) for a sensor network 4 ft by 4 ft, θ = 30°, and a sample size of 500.

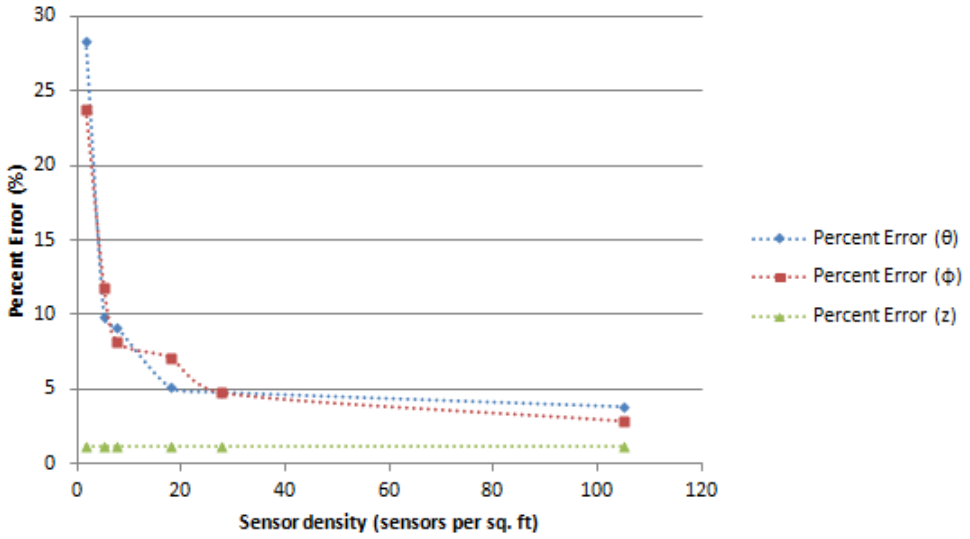

Figure 77 - Simulated plot of sensor network density vs. percent error (θ, φ, and z) for a 16 ft^2 sensor network

This scenario was created in regards to sample sizes > 100 samples and elevation angles between 0° and 90°. This information can be used to plan a suitable sensor network layout for a future embodiment of this project.

5.3 Results of Linear Testing

Custom software was developed and used to analyze the data collected for the linear case, only in three-dimensional space with a fixed orientation. This data was sampled at 1 kHz, or approximately 500 samples per pass. The output of the sensor network is shown in Figure 78,

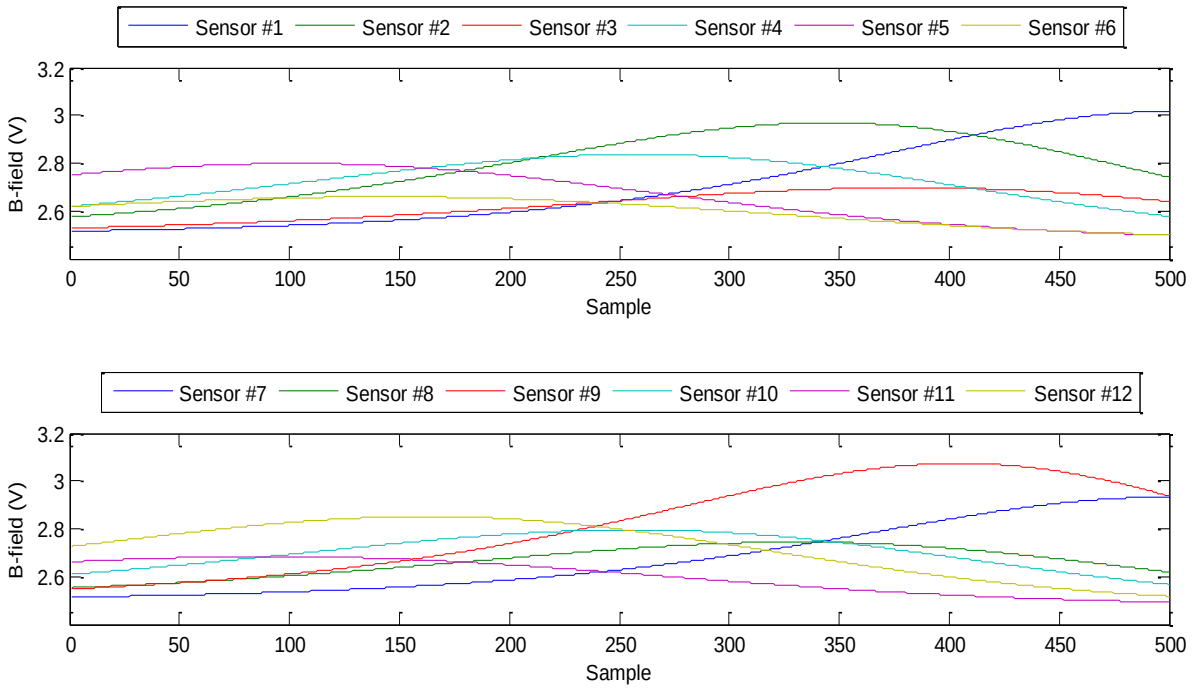

Figure 78 - Output of magnetic sensors for linear test apparatus (θ = 0°)

From these plots, it can be seen that the magnetic source moving closer to magnetic sensors as the simulations progresses. Because the magnetic source is sliding down the test apparatus, the source is indeed getting close to the sensor network.

In order to remove the effect of this non-uniform sensor network layout and other systematic noise, a simulated plot of position was created using an ideal magnetic source traveling about the sensor network, which was calculated using mean position while θ = 0°, 15°, 30°, and 45° (Appendix H), shown in Figure 79. This dataset was used as a baseline for systematic error and was removed from all position calculations.

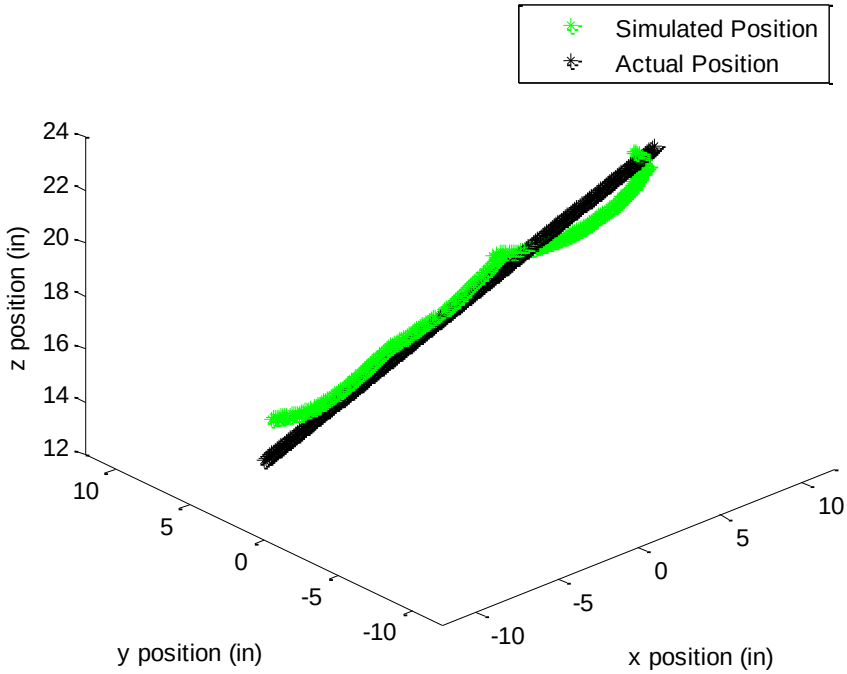

Figure 79 - Simulated position for linear test apparatus using ideal magnetic source as a baseline for systematic error

A plot of the calculated three-dimensional position is shown in Figure 80. These positions are also calculated using the theory discussed in Chapter 3. In the figure, the black points are the actual position of the magnet, starting two feet above, traversing, and ending one foot above the sensor network. The blue points are the calculated positions, and the red points are the estimated positions of the magnetic source based on the calculated points and the Kalman estimation algorithm. The initial position for the Kalman estimator is (0,12,24) in.

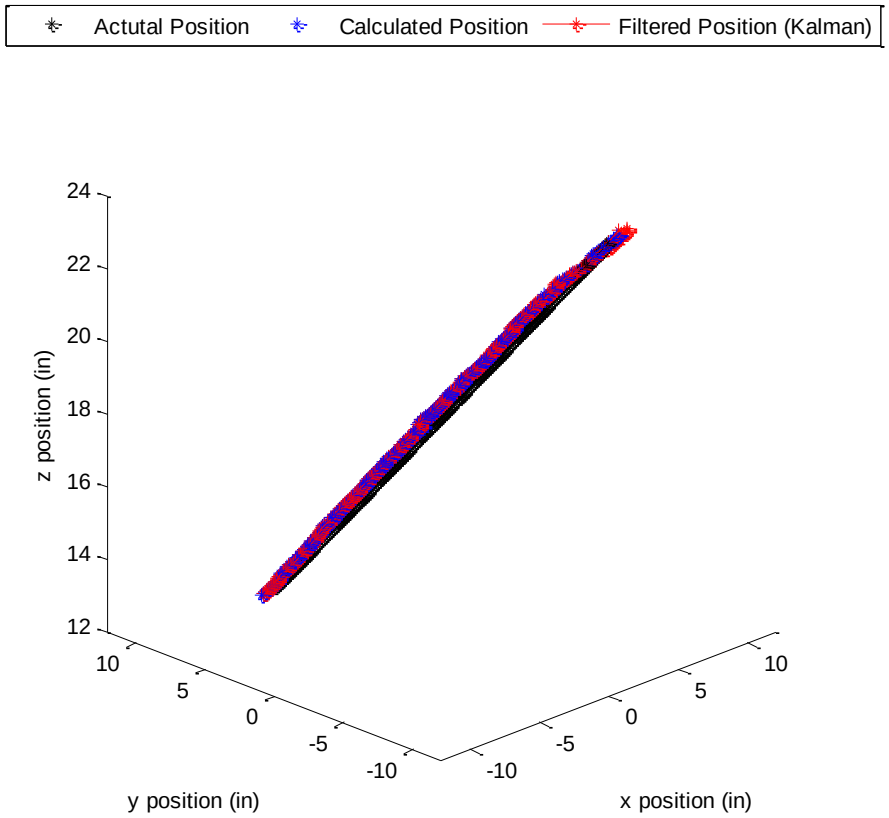

Figure 80 - Position for linear test apparatus (θ = 0°, 15 clusters)

Figure 81 shows a plot of difference error for the simulation. The blue line shows the difference error in the x-axis, the green line shows the difference error in the y-axis, and the red line shows the difference error in the z-axis. The dashed lines show an average value of the corresponding color. The bottom plot shows the same information, but magnified between 0 to 5 inches for clarity.

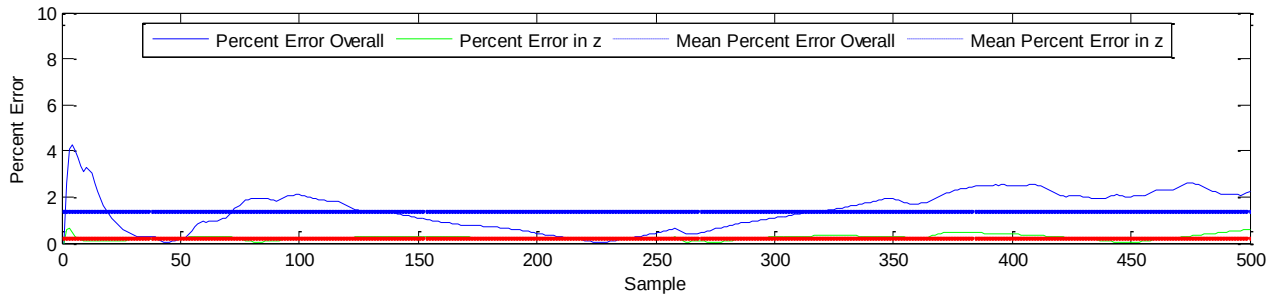

Figure 81 - Percent error for linear test apparatus (θ = 0°, 15 clusters)

Using the same method as the previous section, five sets of experimental data were collected and analyzed with the magnetic source at angles of 0°, 15°, 30°, and 45° running through the linear test apparatus. The first experimental data set was for the magnetic source at an angle of 0°, which is presented here. Additional data sets and plots for the linear test apparatus with other magnetic source angles is in Appendix H. Using the experimental data collected, a summary of the results can be seen in Table 12

Table 15 - Summary of experimental results for linear test apparatus

	Position			
Magnetic Source Angle	Mean Z-Axis Error (%)	Mean Overall Error (%)	Mean Z-Axis Difference (in)	Max Z-Axis Difference (in)
0°	0.24	1.40	0.03	0.09
15°	0.19	1.38	0.03	0.08
30°	0.15	0.87	0.02	0.04
45°	0.19	1.13	0.03	0.14

Once systematic and calibration errors were removed, three dimensional positioning was calculated with little error. This would be expected because the magnetic sensors that were implemented were z-axis sensors. Examining the baseline (Figure 79), the use of a sensor network with only 12 sensors was a detriment to determining three-dimensional position, especially with large magnetic elevations. The mean difference was 0.51 inches and mean maximum difference was 1.37 inches. Using the same simulated case as before, containing 441 uniformly spaced sensors (density of 27 sensors per ft^2) in the same footprint, the results used to determine the z-axis position of a magnetic source. These simulated values can be seen in Table 16, with an actual value of z = 12 inches.

Table 16 - Theoretical vs. simulated z for network with 441 sensors (density of density of 27 sensors per ft^2)

θ (deg)	Simulated z (inches)	Difference in z (inches)
0°	12.38	0.38
15°	12.26	0.26
30°	12.13	0.13
45°	12.01	0.01
60°	11.88	0.12
75°	11.74	0.26
90°	11.70	0.30

It is apparent from this data that this model responds much better to networks with a dense grid of sensors. This can be attributed to the fact that since there are more sensors, the magnetic source spends more time directly above them. This information, along with rotation and elevation angles, can also be used to plan a suitable sensor network layout for a future embodiment of this project.

5.4 Summary of Results

This research set out to show that is was possible to accurately track a permanent magnetic source, including three-dimensional position and orientation with a single-axis sensor network using B-field geometry. The two experimental test apparatuses developed here, one rotational apparatus to determine two-dimensional position and orientation, and one linear apparatus to determine three-dimensional position, were used to verify this hypothesis.

The data collected using the rotation experiment has shown that position with a fixed height can be calculated within 6.4% percent error (worst case) using 12 magnetic sensors in a sensor network with area of 576 inches^2 while averaging approximately 3.86% percent error (mean) during operation. Correcting factors for elevation and rotation were also developed and applied. These correction factors, derived for a dense sensor network, were limited operating on a network with only 12 sensors. Simulated results, though, using a dense sensor network show that θ can be determined with less than a 2° difference over the range of $0° \leq \theta \leq 90°$, with an average of 1.15°. These values will vary and can be optimized with the density of the sensor network.

Data collected using the linear experiment has shown that three-dimensional position can be calculated within approximately 1.5% percent error with an established baseline, for the experimental conditions used. For the baseline, given the experimental setup used, the z-axis component can be determined within 1.7 inches with an average approximately 0.25 inches operation, when the magnetic source is at 45° or less, using the collected data. Once systematic and noise error are removed, the determined a z-axis position results in a 0.24% error (mean, 1.40% max) and a maximum difference of 0.15 inches.

Because the baseline model for determining the z-axis position was on a dense sensor network, the results lagged behind expectation. Simulated results using a dense sensor network show that a z-axis position can be determined with less than a 0.4 inches difference from theoretical, over the range of $0° \leq \theta \leq 90°$, with an average of 0.20 inches. Again, these values can change significantly with the density of the magnetic sensor network.

Additionally, this novel contribution leads to an overall system that can locate and track at computational speeds much faster than suggested iterative solvers. The computational times of the proposed location system are shown in Table 17. These results are based on the solution to the linear test case, with a sample size of 500. The iterative process used MATLAB's nonlinear, least squared solver with a tolerance of 1e-3 and the model in (4.2.7) with 5 sensors as an input and converged in 48.87 sec. This method converges in at most 6 iterations (given good initial conditions). These results show an increase in computational speed up to 1865% using the smallest number of clusters (5), and 274% increase using the number of clusters (15) as used in this experiment.

Table 17 - Computation speeds of geometrical solver vs. MATLAB iterative solver

No. of clusters	Proposed system (sec)	Speed increase (%)
5	2.62	1865
10	8.65	565
15	17.82	274

Chapter 6 – Conclusion and Recommendations

This document outlines a novel, three-dimensional magnetic tracking application. This chapter details conclusions drawn from the results of the previous chapter, as well as recommendations for continued work.

6.1 Conclusion

Presented here is a novel implementation of a "pure-DC" magnetic tracking method. The initial proposal was that a methodology could be developed that implements a single-axis magnetic sensor network to be used to determine three-dimensional position and orientation of a magnetic projectile. Results show that using the unique geometry of the B-field to calculate the position and orientation of a magnetic source is a viable option to track magnetic objects in three-dimensional space.

This contribution has shown that it is not necessary to gather multiple dimensions of magnetic sensor information to determine a magnet's position in free-space. It is possible to track and locate the three-dimensional position and orientation of a permanent magnetic source (with known magnetic flux geometry) with only a single-axis magnetic sensor network. While this systems work well with three-dimensional tracking problems, it is also capable of two-dimensional tracking with less computational effort. Using the approach outlined in this document, position and orientation can be described solely based on the location and B-field magnitude of each single-axis magnetic sensor.

6.2 Recommendations

Several recommendations could be suggested for future work. Having the ability to acquire sensor data with one system would greatly reduce the overhead of the processing unit (as

opposed to the two DAQ cards used in this project). For a commercial application, it would be recommended that a single DAQ with appropriate specifications be used.

Additionally, it is recommended that an analysis of an optimal geometric shape, size, and locations of the magnetic sensors and sensor clusters be performed to reduce the calculation error. Using this experimentation as a baseline, it will be possible to scale this work, up or down, to satisfy a host of magnetic location and tracking applications, specifically those mentioned in this dissertation.

While some parameters have not been completely investigated, a continued effort can be made to:

- Examine the feasibility of using different magnetic sources (other than neodymium permanent magnetic disk)
- Determine optimal sensor network layout (spacing and shape for specified source) for desired application.
- Create a sensor network that can take advantage of recording information for both magnetic source position and ambient magnetic noise simultaneously.
- Examine (micro and macro) scalability of a magnetic tracking system.

References

[1] Ascension Technology Corporation, “Magnetic fact sheet and video: DC vs. AC tracking”, white paper, http://www.ascension-tech.com/docs/ASCWhitePaperDCvAC.pdf, accessed 22 May 2012.

[2] Bachmann, E. R., "Inertial and Magnetic Tracking of Limb Segment Orientation for Inserting Humans into Synthetic Environments," Dissertation, Naval Postgraduate School, Monterey, CA, 2000.

[3] Ferre, M., et al, “Position tracking and imaging system for use in medical applications”, U.S. Patent No. 5967980, 1999.

[4] Wong, P. S., Sastre, A., “Simultaneous AC and DC magnetic field measurements in residential areas: Implications for resonance theories of biological effect,” *IEEE Transactions on Power Delivery*, vol. 10, no. 4, 1995.

[5] Lu, D. J., et al, “Wireless identification and tracking using magnetic fields”, U. S. Patent No. 6686881, 2004.

[6] Vinegar, H. J., et al, “Thermal processes for subsurface formations”, U. S. Patent No. 7121342, 2006.

[7] Iwamatsu, T., et al, “Tracking control device for magnetic recording/reproducing apparatus”, U. S. Patent No. 5262908, 1993.

[8] Sauer, F., “Method and apparatus for augmented reality visualization”, U. S. Patent No. 6919867, 2005.

[9] Polhemus, “AC & pulsed DC motion trackers”, web paper, http://www.polhemus.com/polhemus_editor/assets/AC-DCwebPaper1.pdf, accessed 2 February 2009.

[10] Rees, D., et. al, " CLICK-IT: interactive television highlighter for sports action replay", IEEE Fourteenth International Conference on Pattern Recognition, vol. 2, pp 1448-1487, August 1998.

[11] Pers, J. and Kovacic, S., " Computer vision system for tracking players in sports games", Proceedings of the First International Workshop on Image and Signal Processing and Analysis, pp 177-182, 2000.

[12] Pingali, G.S., et. al, "Real time tracking for enhanced tennis broadcasts", IEEE Computer Vision and Pattern Recognition, pp 260-265, June 1998.

[13] Owens, N., Harris, C., and Stennett, C., "Hawk-eye tennis system", International Conference on Visual Information Engineering, 2003, pp 182-185, July 2003.

[14] Cavallaro, R., "The FoxTrax hockey puck tracking system", IEEE Computer Graphics and Applications, vol. 17, no. 2, pp 6-12, 1997.

[15] Rohrer, M., Bauer, H., Mintorovitch, J., Requardt, M., and Weinmann, H. J., " Comparison of Magnetic Properties of MRI Contrast Media Solutions at Different Magnetic Field Strengths," *Investigative Radiology*, vol. 40, no.11, pp 715-724, Nov 2005.

[16] Schenck, J., "Health and Physiological Effects of Human Exposure to Whole-Body Four-Tesla Magnetic Fields during MRI," *Annals of the New York Academy of Sciences*, vol. 649, no. 1, Dec 2006.

[17] Stuchly, M. A. and Dawson, T. W., " Interaction of Low-Frequency Electric and Magnetic Fields with the Human Body" *Proceedings of the IEEE*, vol. 88, no. 5, May 2000.

[18] Okamoto, K., *Global environment remote sensing*, ISO Press, Amsterdam, The Netherlands, 2001.

[19] Want, R., "An introduction to RFID technology," *IEEE Pervasive Computing*, vol. 5, no. 1, pp 25-33, Jan 2006.

[20] Canada Centre for Remote Sensing, “Fundamentals of remote sensing”, http://www.ccrs.nrcan.gc.ca/resource/tutor/fundam/index_e.php, modified 25 September 2007, accessed 2 February 2009.

[21] Cheng, V., Sridhar, B., “Integration of active and passive sensors for obstacle avoidance,” *Journal of IEEE Control Systems*, vol. 10, no.4, pp 43-50, June 1990.

[22] Caruso, M., Bratland, T., Smith, C., and Schneider, R., “A new perspective on magnetic field sensing”, *Sensors Expo Proceedings*, pp 195-21 3, October 1998.

[23] Hansen, P. K., “Magnetic position and orientation measurement system”, U. S. Patent No. 4622644, 1984.

[24] Nelson, C. V., Jacobs, B. C., “Magnetic sensor system for fast-response, high accuracy, three-dimensional position measurement”, U. S. Patent No. 6789043 B1, 2004.

[25] You, Y., et al, “Precise position detection technique for permanent magnet linear synchronous motors”, *14th International Conference on Mechatronics and Machine Vision in Practice*, pp 73-77, December 2007.

[26] Schneider, M., Stevens, C., “Development and testing of a new magnetic-tracking device for image guidance”, *Proceedings of the SPIE*, vol. 6509, pp. 65090I, 2007.

[27] Zachmann, G., “Distortion correction of magnetic fields for position tracking”, *IEEE Proceedings of Computer Graphics International*, pp 213-220, 1997.

[28] Lenz, J., “A review of magnetic sensors”, 0018-9219/90, *Proceedings of the IEEE*, vol. 78, No. 6, June 1990.

[29] Webster, J. G., *The measurement, instrumentation, and sensor handbook*, ch. 48, “Magnetic Field Measurement,” by Steven A. Macintyre, CRC Press, Baco Raton, FL, 1999.

[30] Ramo, S., Whinnery, J., Van Duzer, T., *Fields and waves in communication electronics*, John Wiley & Sons, Inc., Hoboken, NJ, 1994.

[31] Inan, U., Inan, A., *Engineering electromagnetics*, Addison Wesley Longman, Inc., Menlo Park, CA, 1999.

[32] Lorrain, P., Corson, D., *Electromagnetic fields and waves*, 2nd ed., W. H. Freeman & Co. Ltd., San Francisco, CA, 1970.

[33] Shearer, S. E., “Three-dimensional inversion of magnetic data in the presence of remanent magnetization”, Master’s Thesis, Colorado School of Mines, Golden, CO, 2005.

[34] Biro, O., Preis, K., "On the Use of the Magnetic Vector Potential in the Finite Element Analysis of Three-Dimensional Eddy Currents," *IEEE Transactions on Magnetics*, vol. 25, no. 4, pp. 3145-3159 July 1984.

[35] Griffiths, D. J., *Introduction to Electrodynamics*, 3rd edition, Prentice-Hall, Inc., Upper Saddle River, NJ, 1999.

[36] Schlageter, V., Besse, P. A., Popovic, R. S., Kucera, P., "Tracking system with five degrees of freedom using a 2D-array of hall sensors and a permanent magnet", *Sensors and Actuators*, vol. 92, pp 37-42, 2001.

[37] Connors, M., “Measurement and analysis of the field of disk magnets,” *The Physics Teacher*, vol. 40, pp 308-311, 2002

[38] Jiles, D., *Introduction to magnetism and magnetic materials*, Chapman & Hall/CRC, Boca Raton, FL, 1998.

[39] Moskowitz, B., “Hitchhiker’s guide to magnetism”, Institute for Rock Magnetism, Department of Geology and Geophysics, University of Minnesota, http://www.irm.umn.edu/hg2m/hg2m_index.html, accessed 21 February 2009.

[40] Bowler, N., "Frequency dependence of Relative Permeability in Steel," *AIP Conference Proceedings*, vol. 820, pp 1269-1276, 2006.

[41] Heck, C., *Magnetic materials and their applications*, Crane, Russak and Company, Inc., New York, 1974

[42] Petrie, R., "Permanent magnets in review," *Proceedings of Electrical Electronics Insulation Conference and Electrical Manufacturing & Coil Winding Conference*, pp 207-210, October 1993.

[43] Madawala, U., Pillay, S., "A magnetic field based technique for 3D position tracking," *IECON 2005. 31st Annual Conference of IEEE Industrial Electronics Society*, pg. 6, November 2005.

[44] Raab, F., Blood, E., Steiner, T., Jones, H., "Magnetic position and orientation tracking system," *IEEE transactions on Aerospace and Electronic Systems*, vol. AES-15, no. 5, September 1979.

[45] Kelly, C., *Iterative methods for optimization*, SIAM, Philadelphia, PA, 1999.

[46] Schlageter, V., Drljaca, P., Popovic, R. S., Kucera, P., "A Magnetic Tracking System based on Highly Sensitive Integrated Hall Sensors", *JSME International Journal*, Series C, Mechanical systems, machine elements and manufacturing vol. 45, no. 4, pp. 967-973, 2002.

[47] Sherman, J. T., Lubkert, J. K., Popovic, R. S., DiSilvestro, M. R., "Characterization of a novel magnetic tracking system", *IEEE Transactions on Magnetics*, vol. 43, no. 6, June 2007.

[48] Bittel, H., "Noise of ferromagnetic materials", *IEEE Transactions on Magnetics*, vol. MAG-5, no. 3, September 1969.

[49] Stutzke, N. A., Russek, S. E., pappas, D. P., "Now-frequency noise measurements on commercial magnetoresistive magnetic field sensors", *Journal of Applied Physics*, vol. 97, 2005.

[50] E.L. Maxwell, E. L., Stone D. L., "Natural noise fields 1cps to 100kc", *IEEE Transactions on Antennas and Propagation*, vol. AP-11, no. 3, pp 339-43, May 1963.

[51] Meloy, J., "What and where is the natural noise floor?", http://www.vlf.it/naturalnoisefloor/naturalnoisefloor.htm, accessed 12 July 2010.

[52] National Geophysical Data Center, World Magnetic Model Coefficients 2010, NOAA, http://www.ngdc.noaa.gov accessed 14 April 2012.

[53] Stoner, J. S. and St-Onge G., "Chapter Three Magnetic Stratigraphy in Paleoceanography: Reversals, Excursions, Paleointensity, and Secular Variation," *Developments in Marine Geology*, vol. 1, pp 99-138, 2007.

[54] National Geomagnetism Program, United States Geological Survey, http://geomag.usgs.gov accessed 28 November 2012.

[55] Sabaka, T. J., Olsen, N., and Langel, A., "A comprehensive model of the quiet-time, near-Earth magnetic field: phase 3", *Geophysical Journal International*, vol. 151, pp 32-68, February 2002.

[56] Stepisnik, J., "NMR down to Earth", *NATURE, International weekly journal of science*, vol .439, pp 799-801, February 2006.

[57] Kalman, R. E., "A new approach to linear filtering and prediction problems," *Transactions of the ASME - Journal of Basic Engineering*, no. 82, series D, pp 35-45, 1960.

[58] Kalman, R. E., "Contributions to the Theory of Optimal Control", *Boletin de la Sociedad Matematica Mexicana*, vol. 5, pp. 102-119, 1960.

[59] Fox, D., Hightower, J., Liao, L., Schulz, D., Borriello, G., "Bayesian filtering for location estimation", *IEEE Pervasive Computing*, no. 1536-1268/03, pp 24 – 33, 2003.

[60] Simon, D., "Kalman Filtering", *Embedded systems programming*, pp 72 – 79, June 2001.

[61] Welch, G. and Bishop, G., "An Introduction to the Kalman Filter", Course 8, ACM SIGGRAPH, 2001.

[62] Maybeck, P. S., *Stochastic models, estimation, and control: volume 1*, Academic Press, New York, NY, 1979.

[63] Wang, C., Lin, G., Lin C., Chen, R., "An unsupervised kalman filter-based linear mixing approach to MRI classification," *IEEE Asia-Pacific Conference on Circuits and Systems*, pp 1105-1108, December 2004.

[64] Gannot, S., Burshtein, D., Weinstein, E., "Iterative and sequential kalman filter-based speech enhancement algorithms," *IEEE Transactions on Speech and Audio Processing*, vol. 6 no. 4, July 1998.

[65] Hoshiya, M., Saito, E., "Structural identification by extended kalman filter," *Journal of Engineering Mechanics,* vol. 110, no. 12, pp 1757-1770, December 1984.

[66] Crowley, J. L., "World model and position estimation for a mobile robot using Ultrasonic ranging," *IEEE Conference on Robotics and Automation*, vol. 3, pp 1574-1579, May 1989.

[67] Burgard, W., Derr, A., Fox, D., Cremers, A.B., "Integrating global position estimation and position tracking for mobile robots: the dynamic Markov localization approach," *Proceedings of International Conference on Intelligent Robots and Systems*, vol. 2, pp 730-735, October 1998

[68] Fox, D., Burgard, W., Dellaert, F., Thrun, S., "Monte carlo localization: efficient position estimation for mobile robots," *Proceedings of the Sixteenth National Conference on Artificial Intelligence*, July 1999.

[69] Roumeliotis, S., Bekey, G., "Bayesian estimation and kalman filtering: a unified framework for mobile robot localization," *IEEE International Conference on Robotics and Automation*, vol. 3, pp 2985 – 2992, April 2000.

[70] Burgard, W., Fox, D., Hennig, D., Schmidt, T., "Estimating the absolute position of a mobile robot using position probability grids," *Proceedings of the Thirteenth National Conference on Artificial Intelligence*, pp 896 – 901, August 1996.

[71] Chan, V. T., Hu, A G., Plant, J. B., "A kalman filter based tracking scheme with input estimation," *IEEE Transactions on Aerospace and Electronic Systems*, vol. AES-15 no. 2, pp 237-244, March 1979.

[72] Weiss, H., Moore, J. B., "Improved extended kalman filter design for passive tracking," *IEEE Transactions on Automatic Control*, vol. ac-25, no. 4, August 1980.

[73] Dhaouadi, R., Mohan, N., Norum, L., "Design and implementation of an extended kalman filter for the state estimation of permanent magnet synchronous motor," *IEEE Transactions on Power Electronics*, vol. 6, no, 3, July 1991.

[74] Ribeiro, M. I., "Kalman and extended kalman filters: concepts, derivation and properties," *Report for Institute for Systems and Robotics*, Instituto Superior Tecnico, Lisboa, Portugal, February 2004.

[75] Kim, S. J., Iltis, R. A., "Performance comparison of particle and extended kalman filter algorithms for GPS C/A code tracking and interference rejection," *Conference on Information Sciences and Systems*, Princeton University, March 2002.

[76] COMSOL Multiphysics, *Introduction to COMSOL Multiphysics*, ver. 4.0a, COMSOL AB, Sweden, June 2010.

[77] Dirba, I., and Kleperis, J., "Modelling of a switchable permanent magnet magnetic flux actuator," *Proceedings of the 2011 COMSOL Conference*, Stuttgart, Germany, October 2011.

[78] Wang, D. A., and Chang, K. H., "Electromagnetic energy harvesting from a flow induced vibration," *Microelectronics Journal*, vol 41, no. 6, pp 356-364, June 2010.

[79] ViziMag, “Visualize magnetic fields: electromagnetic finite element modeling, analysis, simulation software, http://www.vizimag.com, accessed 18 February 2010.

[80] COMSOL Multiphysics, *AC/DC Module*, ver. 4.0a, COMSOL AB, Sweden, June 2010.

[81] Dorf, R. C., *The Electrical Engineering Handbook*, CRC Press, Boca Raton, FL, 1993.

[82] Fink, D. G. and Beatty, H. W., *Standard Handbook for Electrical Engineers*, McGraw-Hill Book Co., New York, NY, 1978.

[83] K&J Magnetics, Inc., http://www.kjmagnetics.com/specs.asp, accessed 15 Mar 2012.

[84] "Neodymium." Chemicool Periodic Table, http://www.chemicool.com/elements/neodymium.html created 8 Jul 2011, accessed 15 Mar 2012.

[85] Lunk, B. and Beichner, R., "Exploring Magnetic Fields with a Compass," The Physics Teacher, vol. 49, pp 45-48, January 2011.

[86] Gerth, E. and Glagolevskij, Y. V., "Modelling of stellar magnetic fields by superposition of elementary dipoles," Proceedings of the IUA Symposium, vol. 210, June 2003.

[87] Honeywell, "1- and 2-Axis Magnetic Sensors HMC1001/1002/1021/1022", Datasheet, http://www51.honeywell.com/aero/common/documents/myaerospacecatalog-documents/Missiles-Munitions/HMC_1001-1002-1021-1022_Data_Sheet.pdf, accessed 5 January 2008.

[88] K&J Magnetics, Inc, "Neodymium Magnet Physical Properties", http://www.kjmagnetics.com/specs.asp accessed 13 November, 2011.

[89] Weisstein, E. W. "Line-line intersection." MathWorld--A Wolfram Web Resource", http://mathworld.wolfram.com/Line-LineIntersection.html, accessed 12 July 2010.

[90] Williams, T., "Rowing Performance Monitoring System Deployment," Masters thesis, University of Canterbury, Christchurch, New Zealand, 2001.

[91] NI USB-6226 multifunction DAQ, National Instruments, http://sine.ni.com/nips/cds/view/p/lang/en/nid/203823, accessed 22 November, 2009.

[92] National Instruments, "DAQCard E Series User Manual", http://www.ni.com/pdf/manuals/321138a.pdf , accessed 22 May 2012, modified March 1999.

[93] National Instruments, "NI 6013/6014 User Manual", http://www.ni.com/pdf/manuals/370636a.pdf , accessed 22 May 2012, modified October 2002.

Appendix A – Magnetic Sensor Component Information

AI_1 (NI DAQCard-AI-16XE-50)

Sensor	R200	R5K_1	R5K_2	R1M_2	HW Gain	Calibration Gain	AI
1	198.7	4958	4884	999100	202.51	1.0524	<0,8>
2	199.3	5005	4943	1001200	201.04	0.9651	<1,9>
3	199.0	4957	4921	1002400	203.22	0.9740	<2,10>
4	198.3	4999	4986	999600	200.96	0.9858	<5,13>
5	198.9	4955	4880	1003500	203.52	0.9631	<6,14>
6	199.3	4944	4924	1000300	203.33	0.9805	<7,15>

AI_2 (NI PCI-6013)

Sensor	R200	R5K_1	R5K_2	R1M_2	HW Gain	Calibration Gain	AI
7	199.7	4941	4858	1000000	203.39	1.0817	<0,8>
8	198.6	4949	4888	1002000	203.47	0.9522	<1,9>
9	199.1	4936	4893	999000	203.39	0.9597	<2,10>
10	198.5	5007	4959	1000000	200.72	0.9755	<5,13>
11	199.0	4936	4993	1005000	204.61	0.9285	<6,14>
12	198.8	4881	4916	1005000	206.90	0.9690	<7,15>

*Note: Some labels (R200, R5K_1, R5K_2, and R1M_2) correspond to parts of PCB design shown in Appendix B.

Appendix B – Magnetic Sensor PCB Schematic

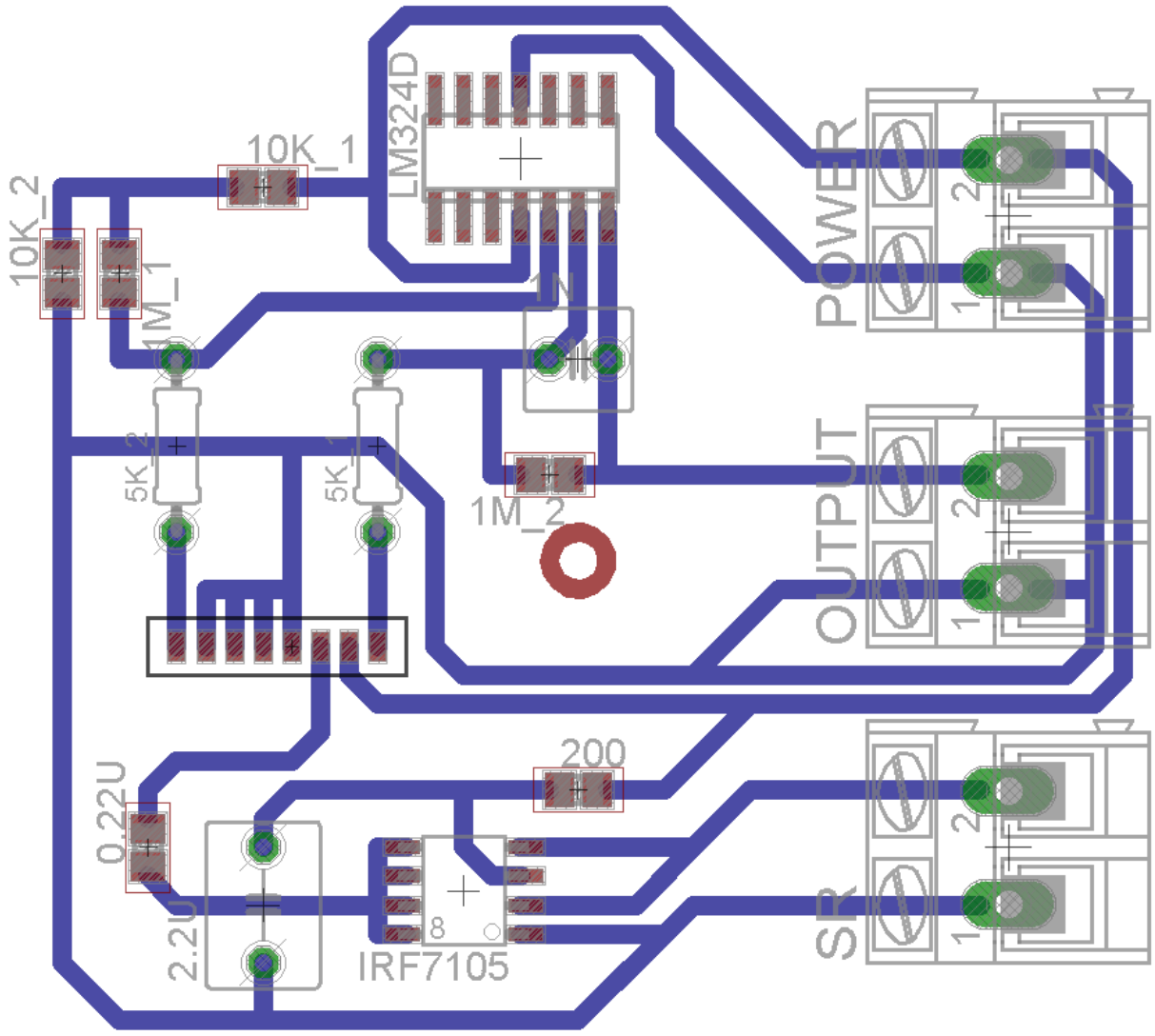

Appendix C – Absolute Positions of Magnetic Sensors

Sensor Number	**X-Positions (in)**	**Y-Position (in)**
#1	-10.4562	-5.3737
#2	-2.5528	-3.1075
#3	-5.4516	-10.4665
#4	1.5438	-5.3737
#5	9.4472	-3.1075
#6	6.5484	-10.4665
#7	-10.4562	6.6263
#8	-2.5528	8.8925
#9	-5.4516	1.5335
#10	1.5438	6.6263
#11	9.4472	8.8925
#12	6.5484	1.5335

**Note*: All positions are relative to the center of the sensor network

Appendix D – Absolute Positions of Center of Sensor Clusters

Cluster Number	X-Positions (in)	Y-Position (in)
#1	-6.1535	5.6841
#2	5.8465	5.6841
#3	-6.1535	-6.3159
#4	5.8465	-6.3159
#5	-8.7880	0.9287
#6	-6.1535	-2.3159
#7	-2.1535	1.6841
#8	-2.1535	5.6841
#9	1.8465	1.6841
#10	2.8127	8.1371
#11	8.4809	2.4395
#12	5.8465	-2.3159
#13	0.8802	-8.7689
#14	-2.1535	-6.3159
#15	1.8465	-2.3159

**Note*: All positions are relative to the center of the sensor network

Appendix E – Frequency Response of Unfiltered and Filtered Magnetic Sensors

NI DAQCard-AI-16XE-50, Sensors #1 - #3

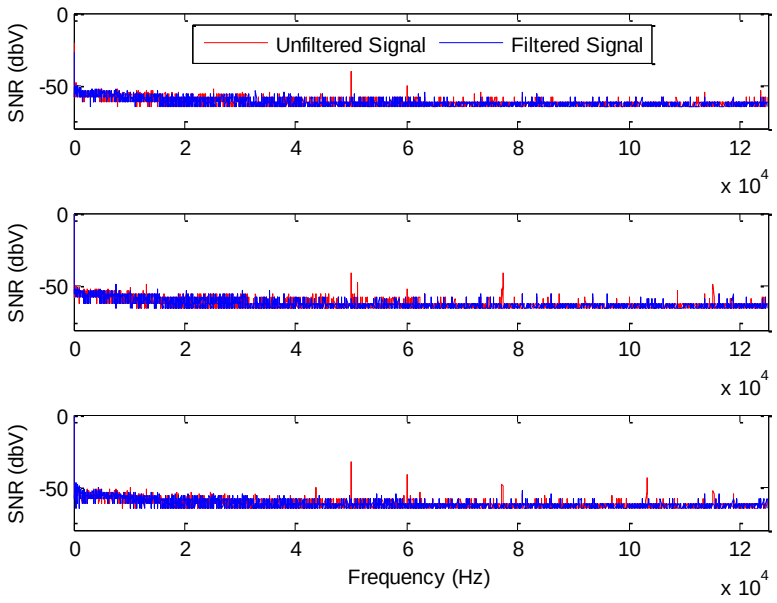

NI DAQCard-AI-16XE-50, Sensors #4 - #6

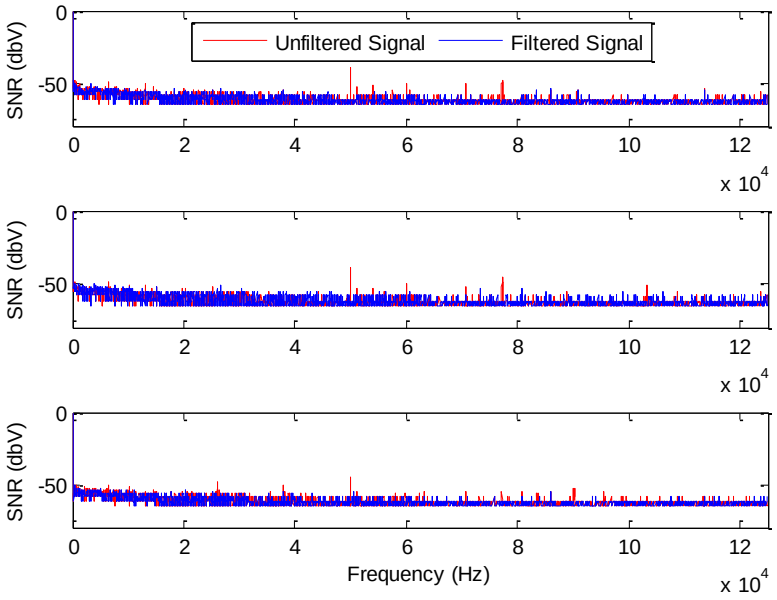

NI PCI-6013, Sensors #1 - #3

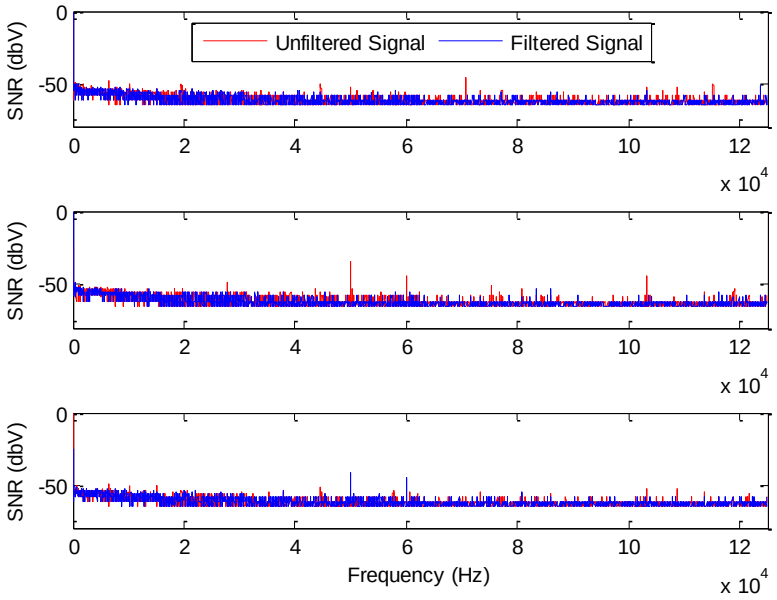

NI PCI-6013, Sensors #4 - #6

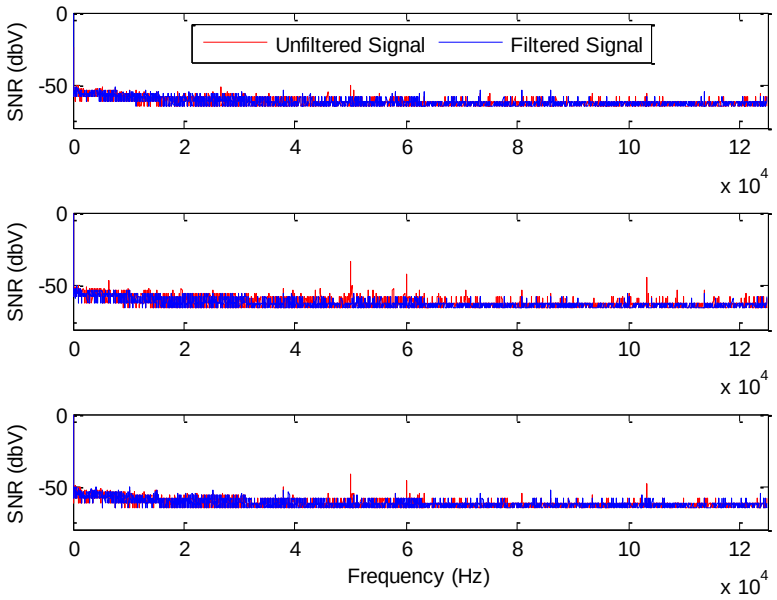

Appendix F – Frequency Response of Power Supply

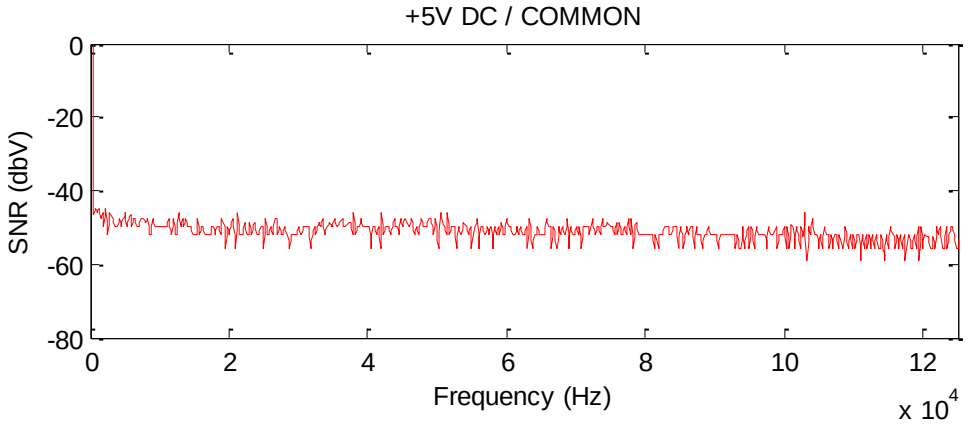

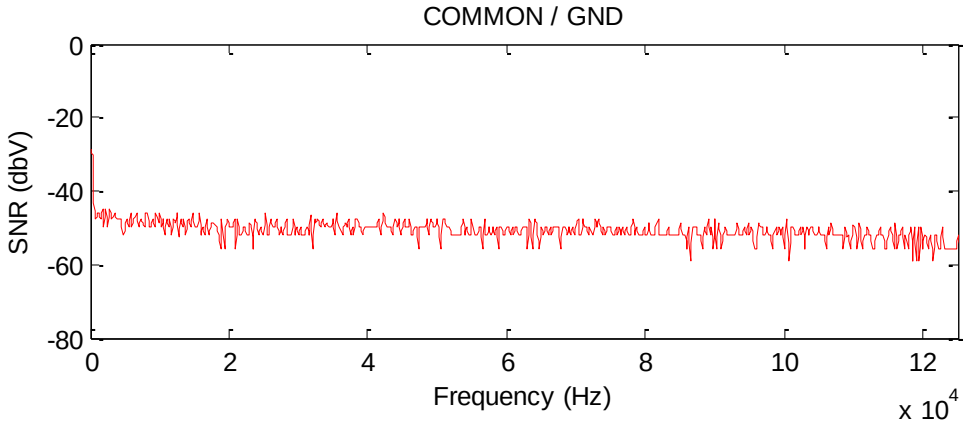

Appendix G – Experimental data for rotation apparatus

Magnetic Source at 15°

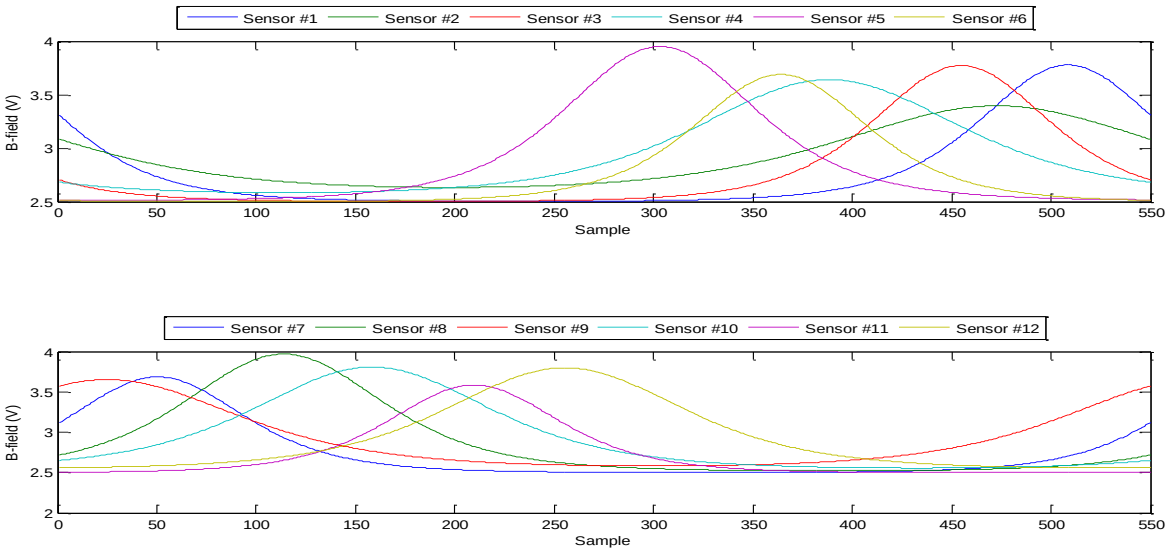

Figure 82 - Output of magnetic sensors for rotating test apparatus (θ = 15°)

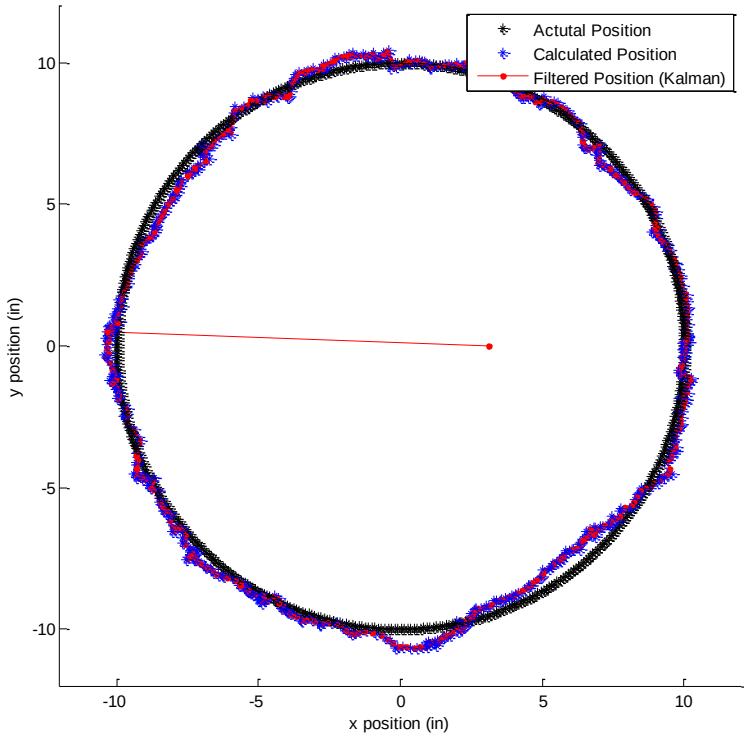

Figure 83 - Radial position for rotating test apparatus (θ = 15°, 15 clusters)

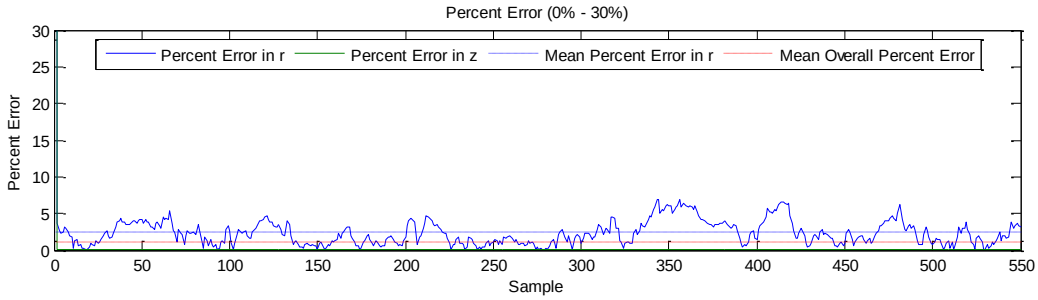

Figure 84 - Experimental percent error for rotating test apparatus (θ = 15°, 15 clusters)

Magnetic Source at 30°

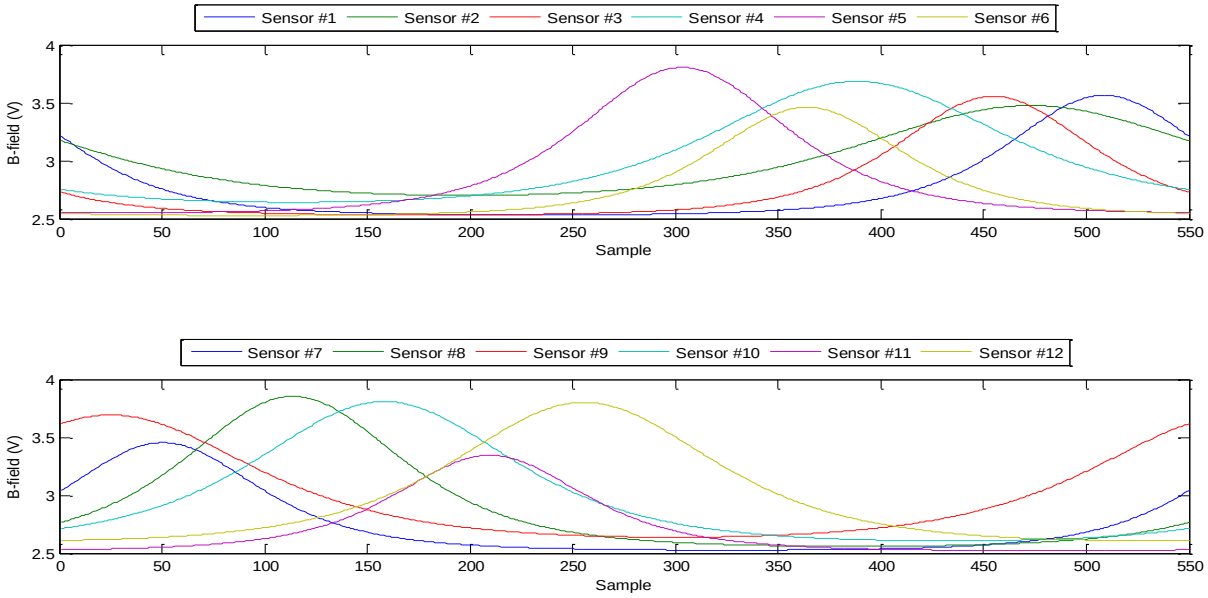

Figure 85 - Output of magnetic sensors for rotating test apparatus (θ = 30°)

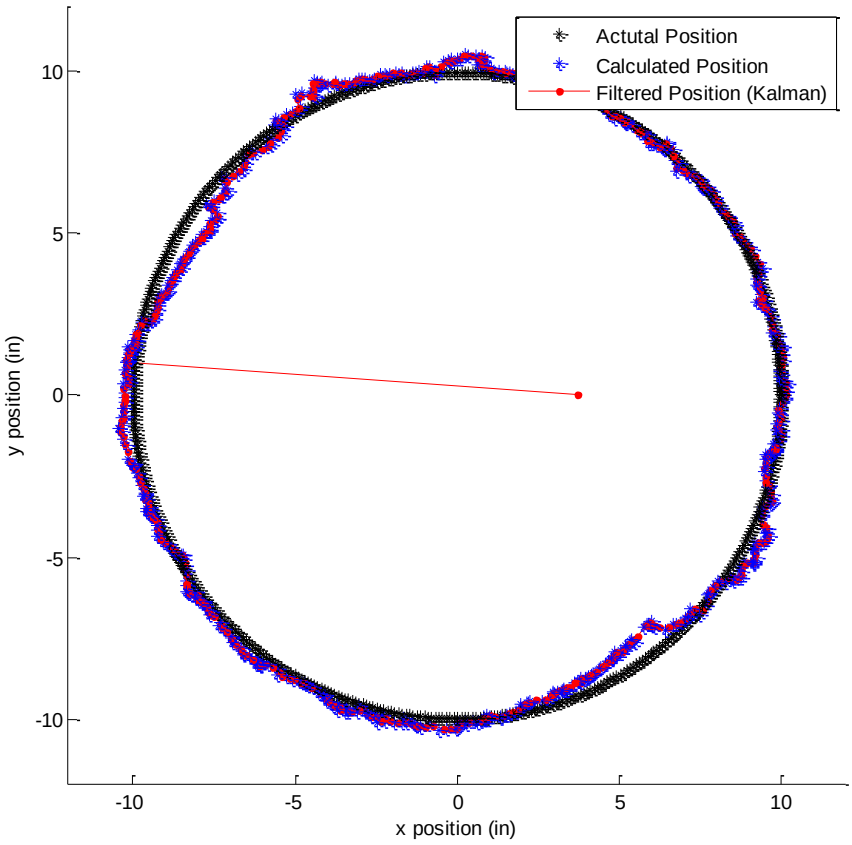

Figure 86 - Radial position for rotating test apparatus (θ = 30°, 15 clusters)

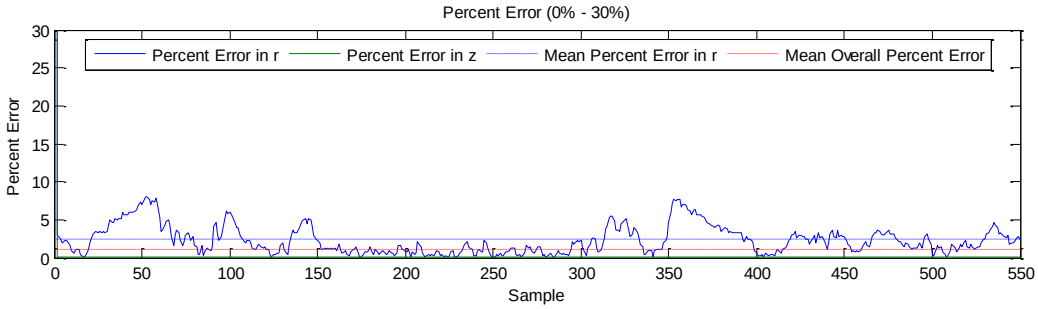

Figure 87 - Experimental percent error for rotating test apparatus (θ = 30°, 15 clusters)

Magnetic Source at 45°

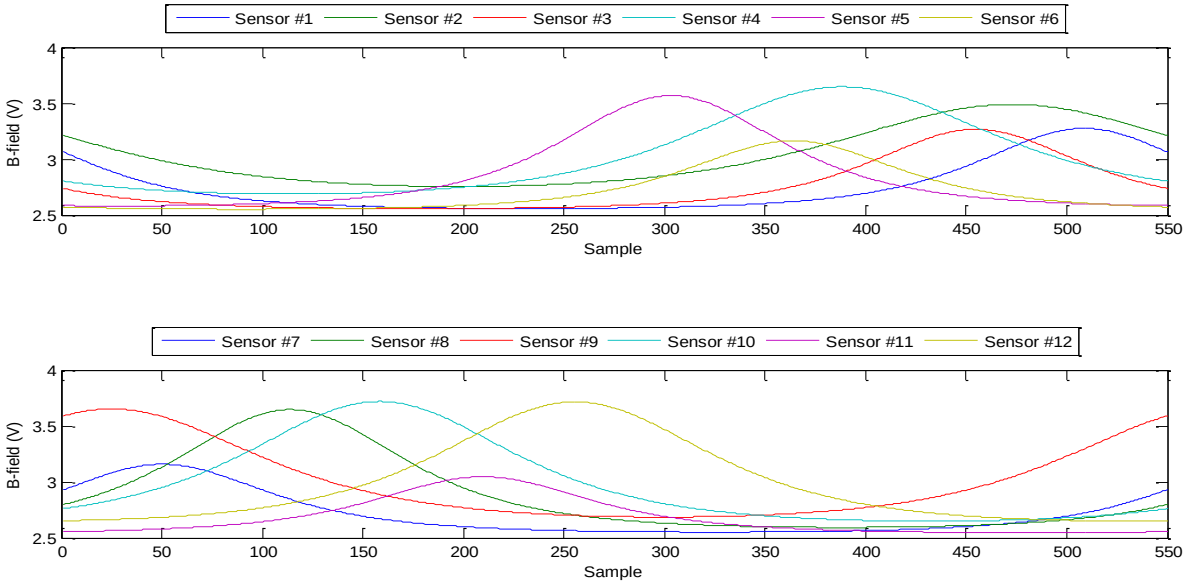

Figure 88 - Output of magnetic sensors for rotating test apparatus (θ = 45°)

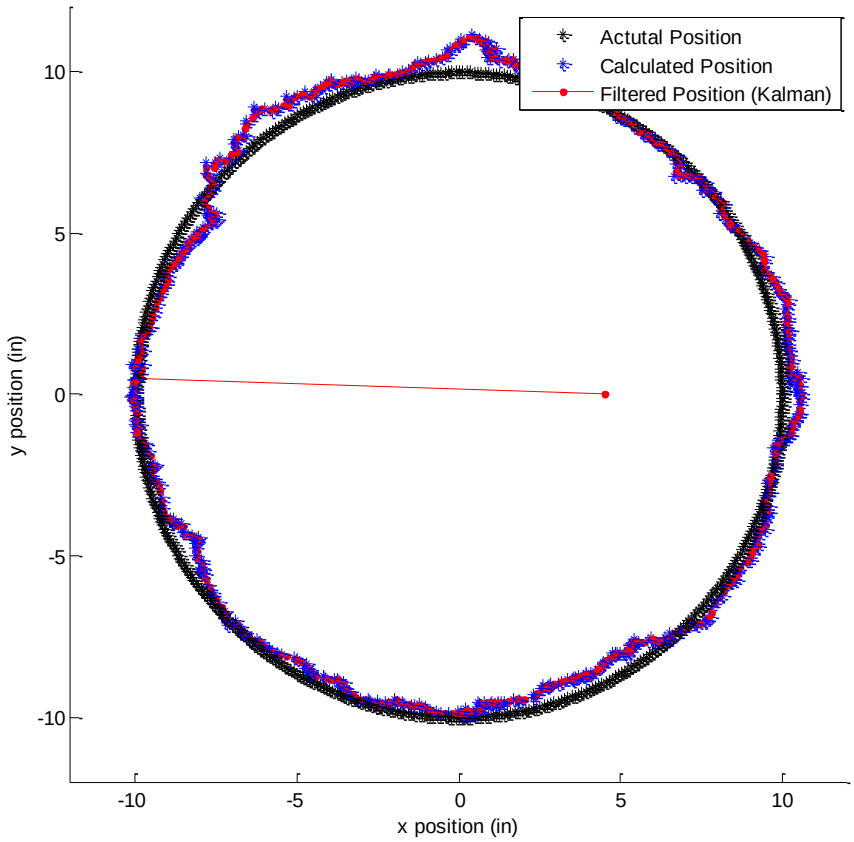

Figure 89 - Radial position for rotating test apparatus (θ = 45°, 15 clusters)

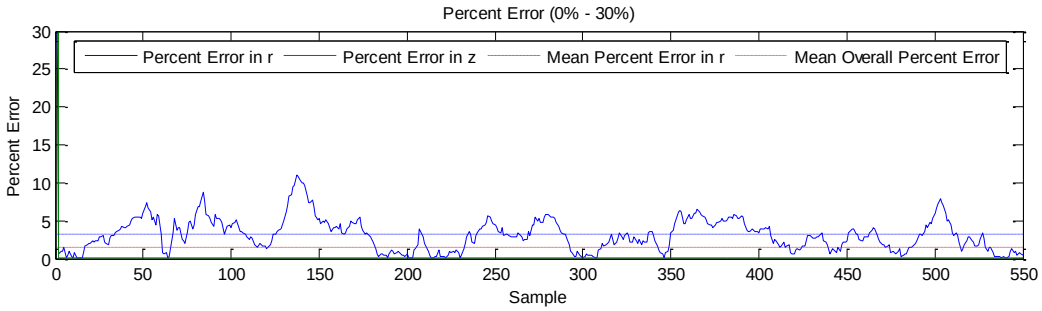

Figure 90 - Experimental percent error for rotating test apparatus (θ = 45°, 15 clusters)

Magnetic Source at 60°

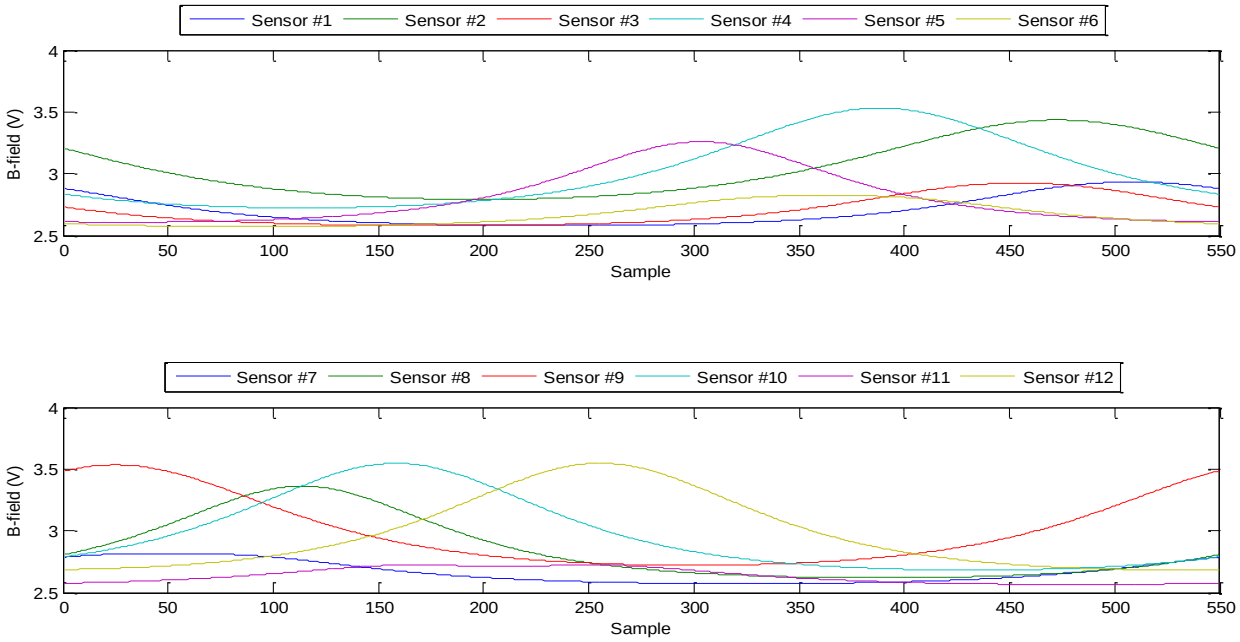

Figure 91 - Experimental output of magnetic sensors for rotating test apparatus (θ = 60°)

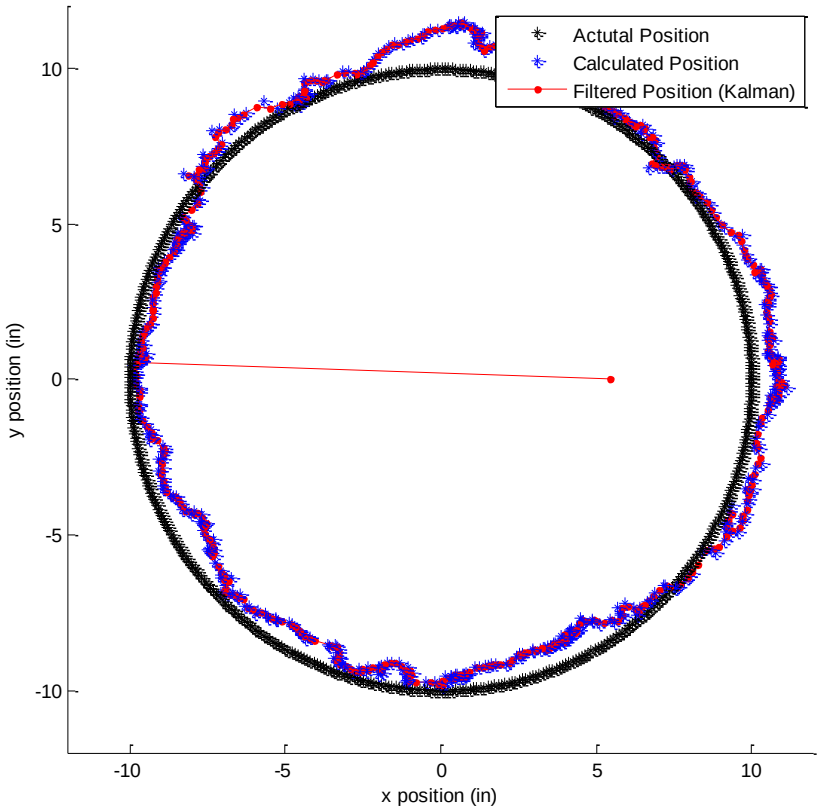

Figure 92 - Radial position for rotating test apparatus (θ = 60°, 15 clusters)

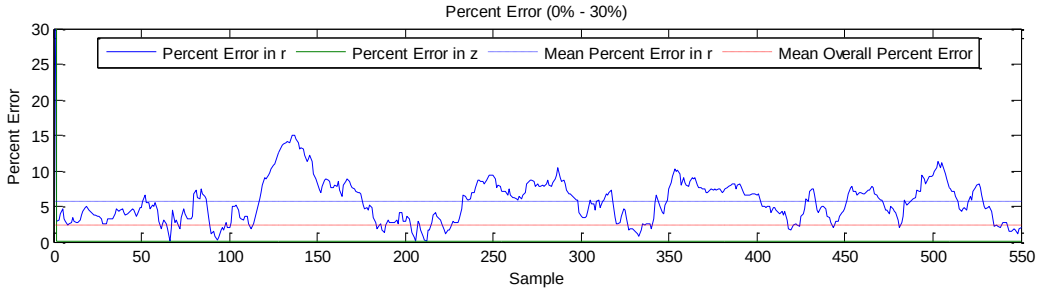

Figure 93 - Experimental percent error for rotating test apparatus (θ = 60°, 15 clusters)

Appendix H – Experimental data for linear apparatus

Magnetic Source at 15°

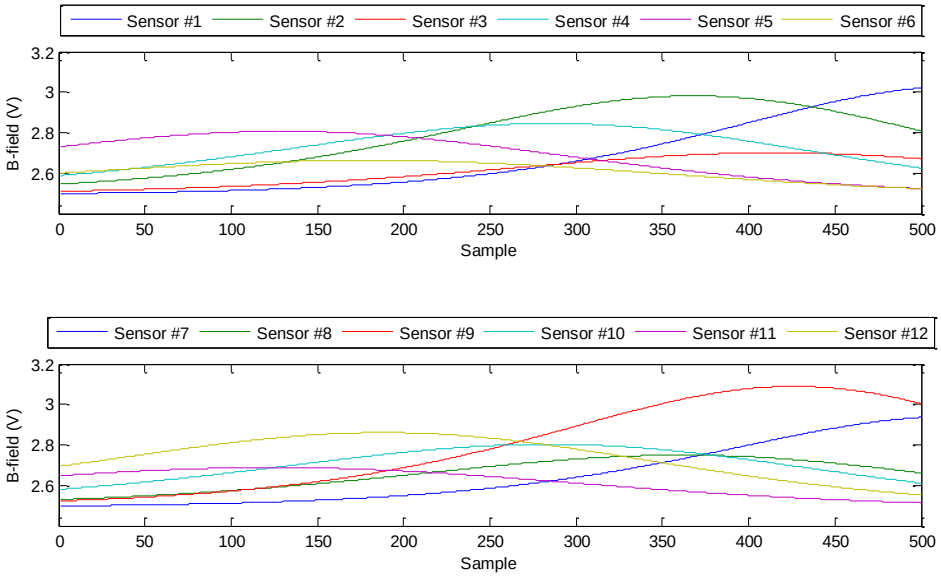

Figure 94 - Output of magnetic sensors for linear test apparatus (θ = 15°)

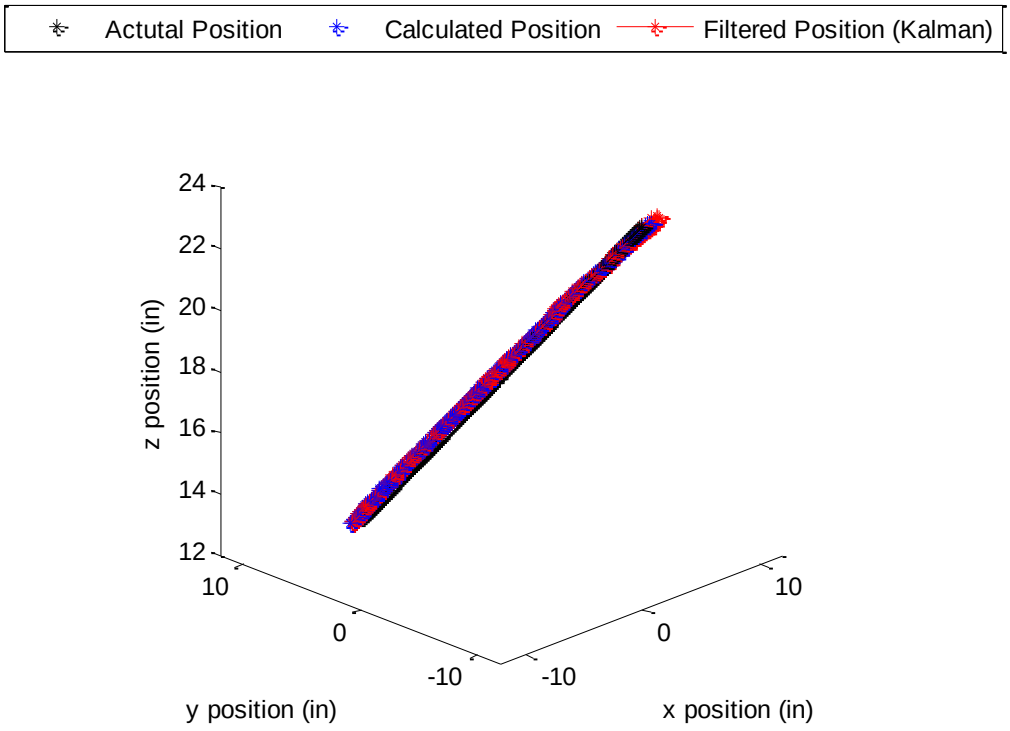

Figure 95 - Three-dimensional position for linear test apparatus (θ = 15°, 15 clusters)

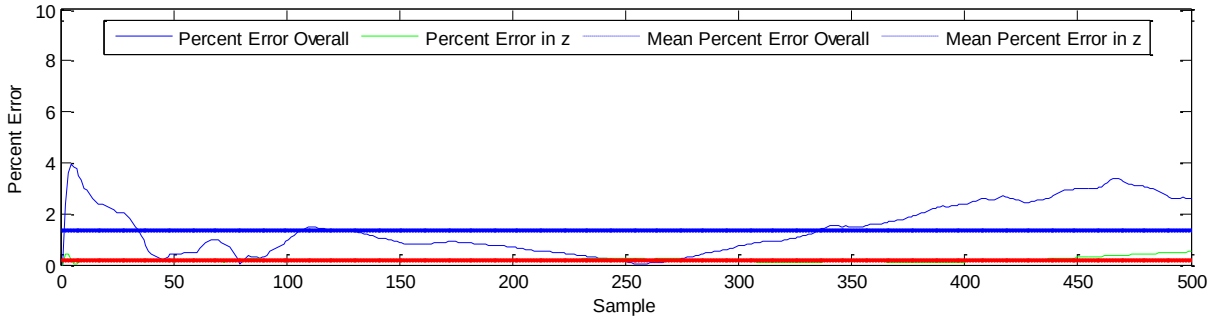

Figure 96 - Error for linear test apparatus (θ = 15°, 15 clusters)

Magnetic Source at 30°

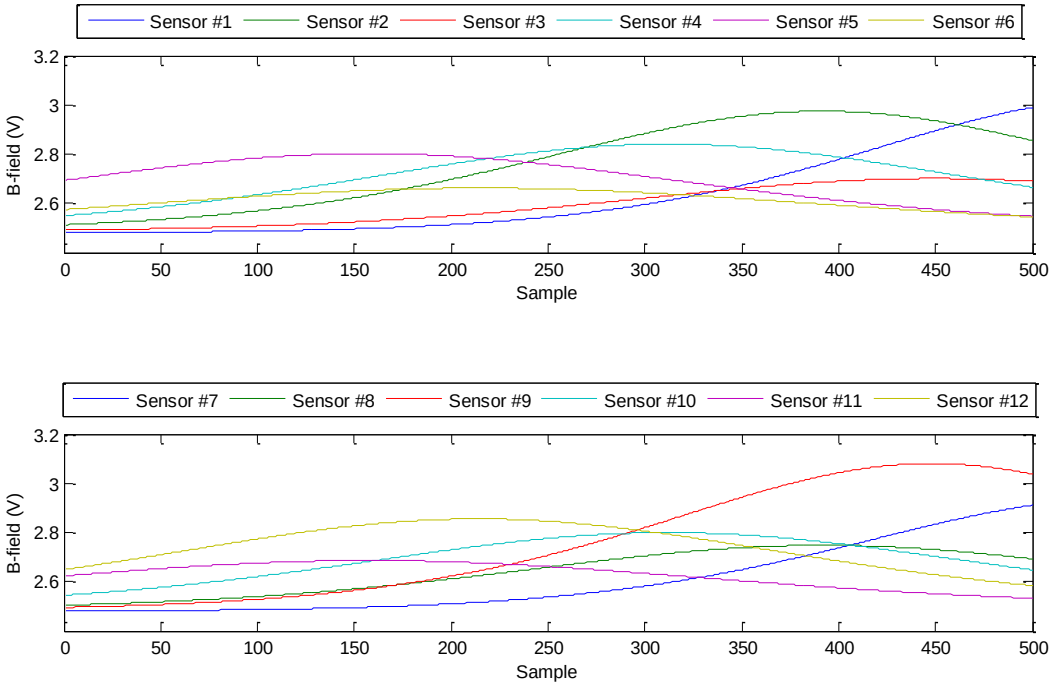

Figure 97 - Output of magnetic sensors for linear test apparatus (θ = 30°)

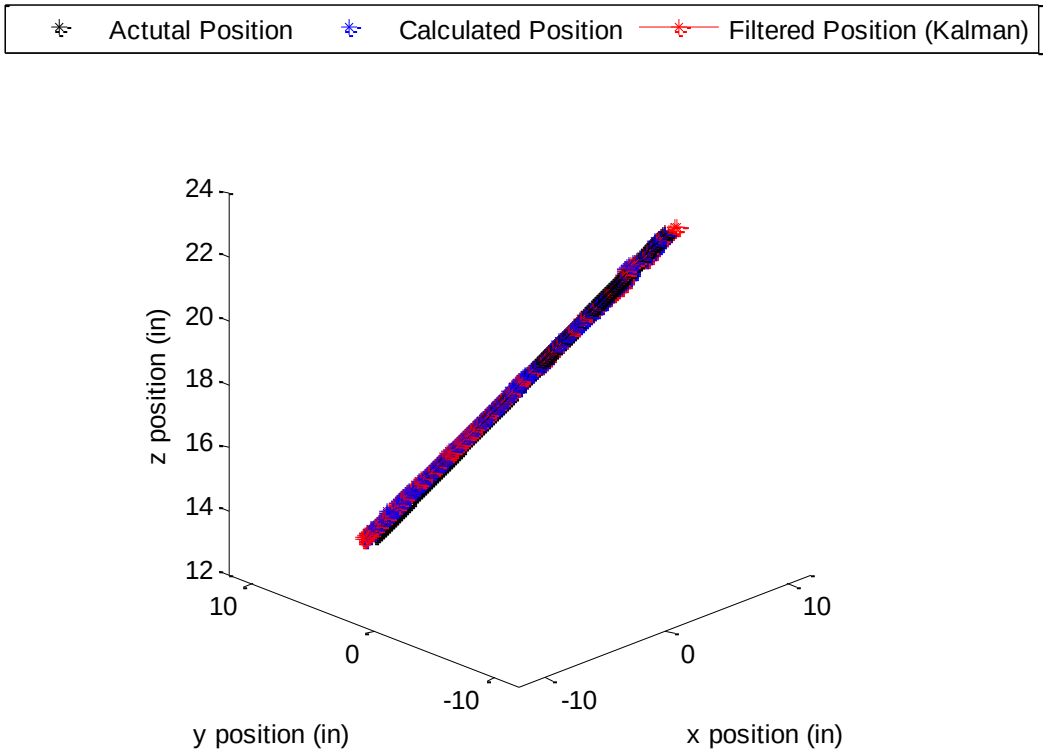

Figure 98 - Three-dimensional position for linear test apparatus (θ = 30°, 15 clusters)

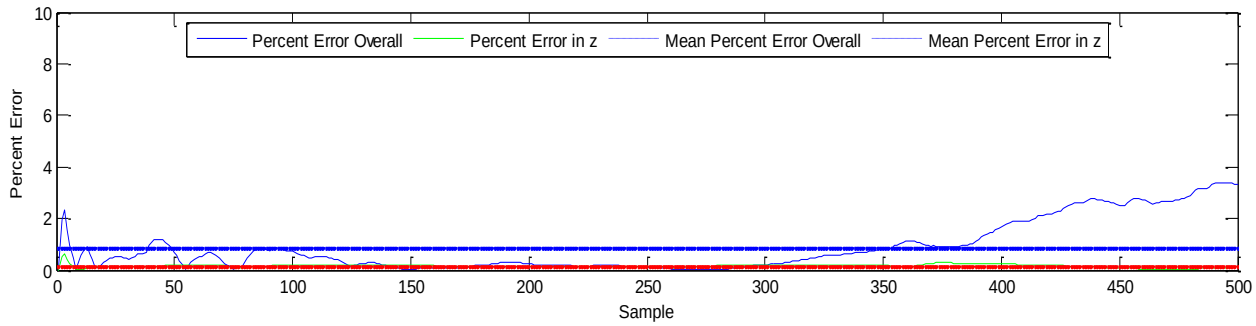

Figure 99 - Error for linear test apparatus (θ = 30°, 15 clusters)

Magnetic Source at 45°

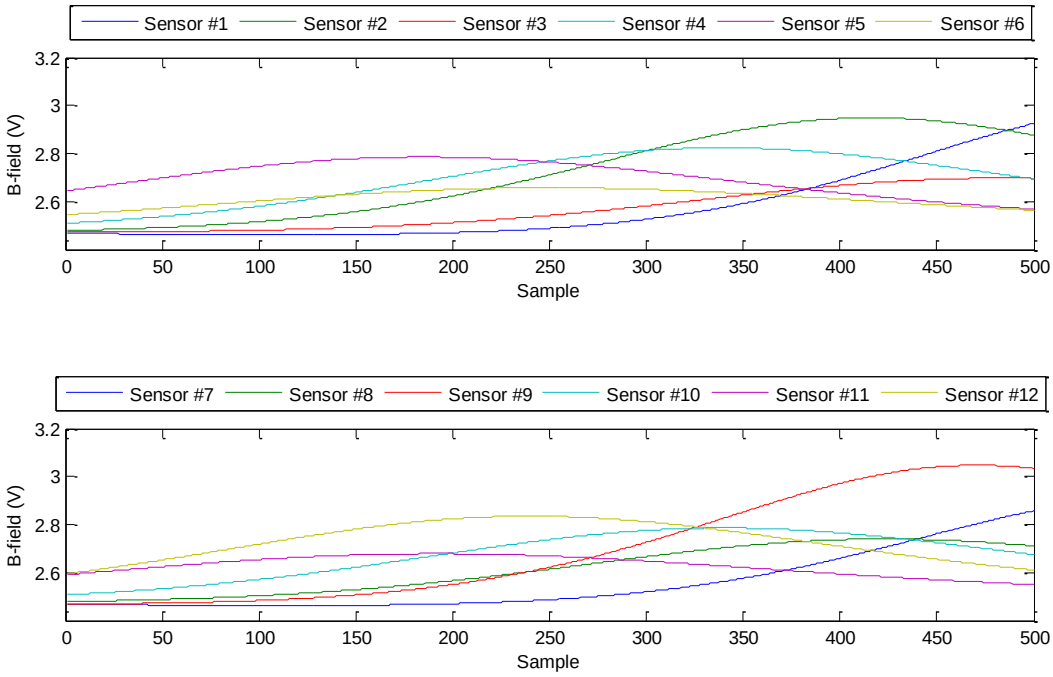

Figure 100 - Output of magnetic sensors for linear test apparatus (θ = 45°)

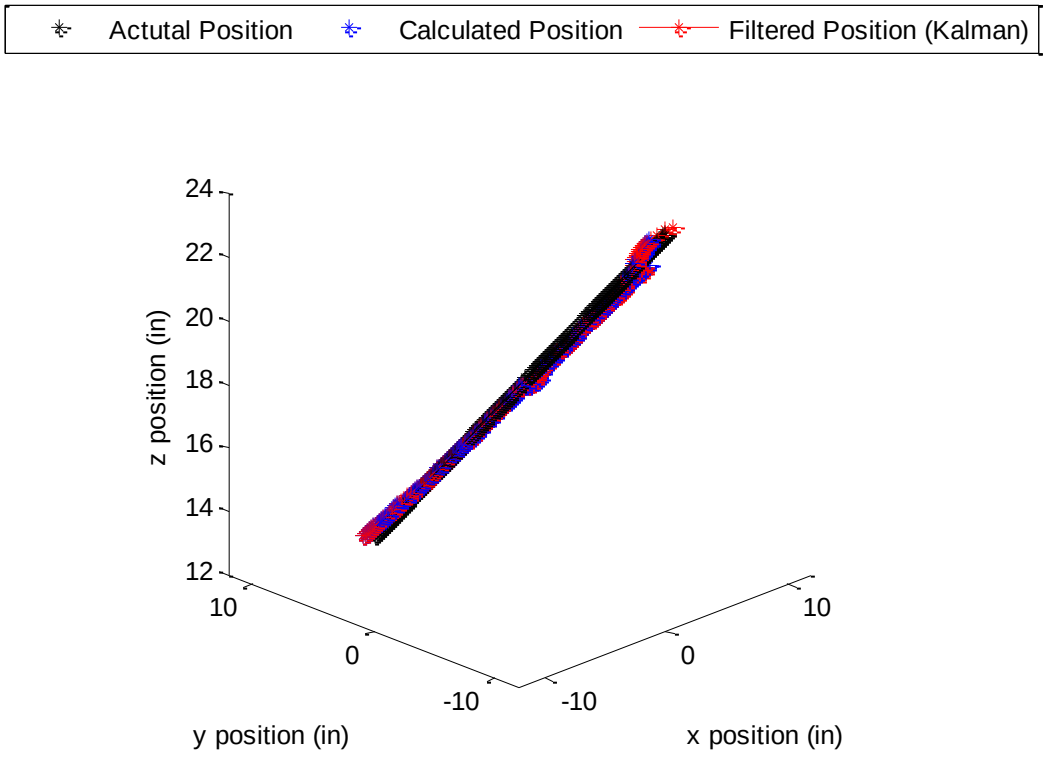

Figure 101 - Three-dimensional position for linear test apparatus (θ = 45°, 15 clusters)

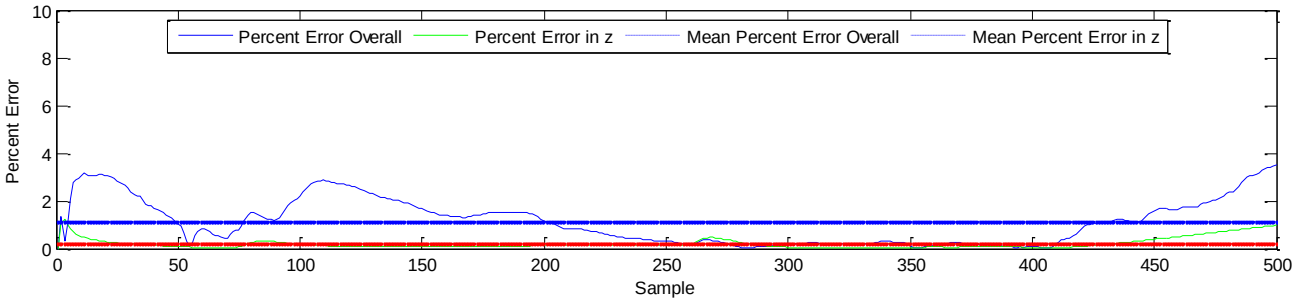

Figure 102 - Error for linear test apparatus (θ = 45°, 15 clusters)